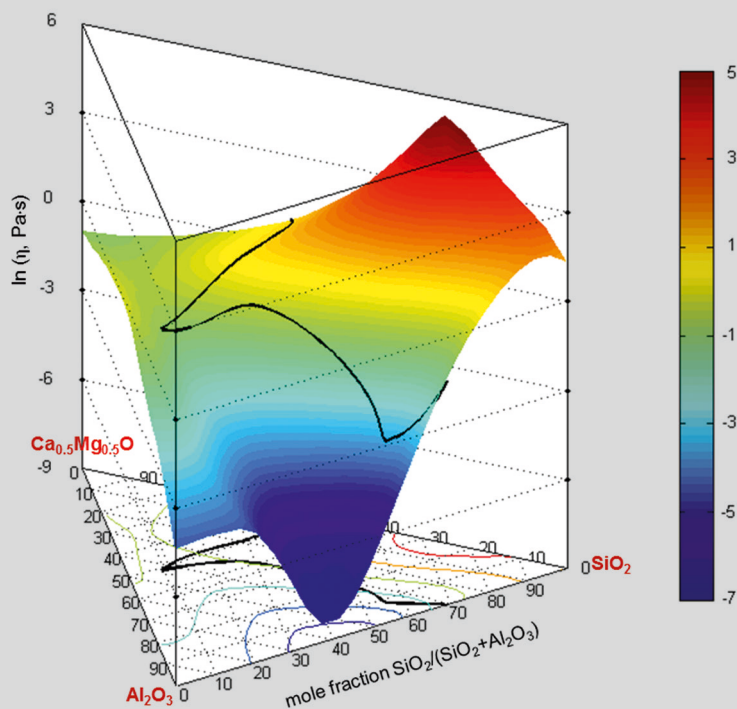


Modelling and Experimental Validation of the Viscosity of Liquid Phases in Oxide Systems Relevant to Fuel Slags

Guixuan Wu



Energie & Umwelt/
Energy & Environment
Band/ Volume 282
ISBN 978-3-95806-081-4

Forschungszentrum Jülich GmbH
Institute of Energy and Climate Research (IEK)
Microstructure and Properties of Materials (IEK-2)

Modelling and Experimental Validation of the Viscosity of Liquid Phases in Oxide Systems Relevant to Fuel Slags

Guixuan Wu

Schriften des Forschungszentrums Jülich
Reihe Energie & Umwelt / Energy & Environment

Band / Volume 282

ISSN 1866-1793

ISBN 978-3-95806-081-4

Bibliographic information published by the Deutsche Nationalbibliothek.
The Deutsche Nationalbibliothek lists this publication in the Deutsche
Nationalbibliografie; detailed bibliographic data are available in the
Internet at <http://dnb.d-nb.de>.

Publisher and Distributor:	Forschungszentrum Jülich GmbH Zentralbibliothek 52425 Jülich Tel: +49 2461 61-5368 Fax: +49 2461 61-6103 Email: zb-publikation@fz-juelich.de www.fz-juelich.de/zb
Cover Design:	Grafische Medien, Forschungszentrum Jülich GmbH
Printer:	Grafische Medien, Forschungszentrum Jülich GmbH
Copyright:	Forschungszentrum Jülich 2015

Schriften des Forschungszentrums Jülich
Reihe Energie & Umwelt / Energy & Environment, Band / Volume 282

D 82 (Diss. RWTH Aachen University, 2015)

ISSN 1866-1793

ISBN 978-3-95806-081-4

The complete volume is freely available on the Internet on the Jülicher Open Access Server (JuSER)
at www.fz-juelich.de/zb/openaccess.

Neither this book nor any part of it may be reproduced or transmitted in any form or by any
means, electronic or mechanical, including photocopying, microfilming, and recording, or by any
information storage and retrieval system, without permission in writing from the publisher.

Kurzfassung

Moderne IGCC-Kraftwerke bieten hinsichtlich der vielseitig verwendbaren Brennstoffe und Produkte die größten Vorteile. Der Prozess verbindet dabei ein konventionelles GuD-Kraftwerk mit einem Vergaserreaktor. Darüber hinaus kann dieser mit einer CO₂-Abscheidung und -Speicherung (CCS Carbon Capture Storage) gekoppelt werden. Diese Technologie ist ein vielversprechender Ansatz, die CO₂-Emission durch fossile Energieträger zu reduzieren. Der Kern des IGCC-Kraftwerkes ist dabei der Vergaser, dieser bestimmt auch maßgeblich die Effektivität des Gesamtprozesses. Die anorganischen Bestandteile bilden auf den Reaktorwänden des Vergasers eine viskose Schlacke. Die verbleibenden anorganischen Komponenten werden in Form von Flugasche im Synthesegas mitgerissen. Die Viskosität der Schlacke spielt eine zentrale Rolle bei der Bestimmung der optimalen Betriebsbedingungen, viele Vorgänge sind direkt oder indirekt abhängig von dem Fließverhalten der Schlacke, wie die Tropfenhaftung (oder Partikelhaftung), der Schlackefluss und -abfluss, sowie die Degradierung der Refraktärmaterialien. Damit beeinflusst das Fließverhalten maßgeblich die Effizienz, Stabilität und Sicherheit des Vergasungsprozesses. Die Viskosität der Schlacke wurde ebenfalls als kritische Größe bei der Simulation durch numerische Strömungsmechanik (CFD) erkannt. Die meisten vorherigen Modelle bieten nur die Möglichkeit, die Viskosität in einem sehr eingeschränkten Bereich von Temperatur und Zusammensetzung zu beschreiben, da insbesondere eine effektive Beschreibung des Einflusses der inneren Struktur auf die Viskosität fehlte.

Das Ziel dieser Arbeit war die Entwicklung eines neuen Modells zur Beschreibung der Viskosität vollständig geschmolzener Schlacken im newtonschen Bereich. In diesem neuen Modell wird die innere Struktur der Schlacke berücksichtigt, indem die Viskosität mit der Art und Verteilung einzelner Schlackenkomponenten, sowie der Wechselwirkung dieser Komponenten untereinander in Verbindung gebracht wird. Die Art der Komponente wird dabei durch die Gibbs-Energie bestimmt, die Verteilung dieser mit einer selbst-konsistenten thermodynamischen Datenbank berechnet. Für die Beschreibung der oxidischen Schlackesysteme wird ein modifiziertes Assoziatenmodell verwendet. Die Datenbank ermöglicht die Berechnung von Phasendiagrammen und

anderen thermodynamischen Eigenschaften in guter Übereinstimmung mit vorhandenen experimentellen Daten. Der Einfluss von Temperatur und Zusammensetzung auf die Struktur vollständig geschmolzener Schlacke wird mit monomeren Assoziaten in Verbindung mit der selbst- und der interpolymersation beschrieben.

Das neue Viskositätsmodell wurde für vollständig geschmolzene Schlacken in dem System $\text{SiO}_2\text{--Al}_2\text{O}_3\text{--CaO--MgO--Na}_2\text{O--K}_2\text{O--FeO--Fe}_2\text{O}_3$ und deren Subsysteme, basierend auf dem thermodynamisch modifizierten Assoziatenmodell, entwickelt. Das Modell erlaubt eine verlässliche Vorhersage der Viskosität über alle genannten Komponenten sowie einen großen Temperaturbereich mit nur einem Satz an Modellparametern. Diese besitzen zusätzlich eine eindeutige physikochemische Bedeutung. Mit dem neuen Modell kann der Lubricant-Effekt in SiO_2 -basierten binären Systemen beschrieben werden. Die Änderung der Viskosität durch den Austausch eines Netzwerkwandlers durch einen anderen bei konstantem SiO_2 -Gehalt wird ebenfalls gut beschrieben. Auch das durch Al_2O_3 bewirkte Viskositätsmaximum kann das Modell beschreiben, so kann sowohl die Konzentration als auch die Viskosität des Maximums in Abhängigkeit von Temperatur und Zusammensetzung (Ladungsausgleichseffekt) vorhergesagt werden. Desweiteren kann ebenfalls das Viskositätsmaximum beim Austausch von Al_2O_3 durch SiO_2 bei ansonsten konstanter Konzentration der Netzwerkwandler dargestellt werden. Der Fe_2O_3 induzierte Ladungsausgleichseffekt ist weniger stark ausgeprägt als bei Al_2O_3 . Das durch Fe_2O_3 bewirkte Viskositätsmaximum zeigt dabei eine starke Abhängigkeit vom Ladungsausgleich von Fe^{3+} . Wird Fe_2O_3 durch SiO_2 bei ansonsten gleicher Zusammensetzung ersetzt, ist es möglich, dass das Viskositätsmaximum nicht mehr vorhanden ist.

Zusätzlich wurde ein Rotationsviskosimeter zur Validierung des entwickelten Viskositätsmodells genutzt. Die Viskosität mehrerer realer Kohleaschen wurde hierfür gemessen. Des weiteren werden Beispiele für die praktische Anwendung des Modells gegeben.

Abstract

Flexibility in feedstocks and products is one of the most important advantages of an IGCC power plant based on entrained-flow gasifiers. Moreover, it can be combined with the carbon capture and storage (CCS), which is a promising solution to control the CO₂ emissions produced from the use of fossil fuels such as coal. The core of an IGCC power plant is the slagging gasifier, whose performance is significant for an IGCC power plant. In slagging gasifiers, the majority of the inorganic components are converted to a liquid slag flowing down the wall of the gasifier, whereas the remaining inorganic components entrained in the syngas form fly ash. Slag viscosity plays a very important role in determining the optimum operating conditions for slagging gasification, in which many processes are related to the viscosity, such as the particle sticking (or droplet sticking), slag flow, slag tapping, and refractory degradation that may lead to concerns about efficiency, process reliability, and safety. Slag viscosity is also identified as a critical property for simulations based on computational fluid dynamics (CFD). However, most of the early viscosity models are only capable of describing the viscosity over a limited range of temperatures and compositions, due to the lack of an effective description about the structural dependence of viscosity.

This study aims at developing a new viscosity model for fully liquid slag systems in the Newtonian range. In the new viscosity model, the structure of slag is effectively taken into account, in which the viscosity is linked to the type and distribution of species, as well as the connectivity of species. The type of species is determined from the Gibbs energy, and thereby the distribution of species is calculated by using a completely self-consistent thermodynamic dataset, where the modified associate species model was applied for the slag. This dataset provides the phase diagram and other thermodynamic properties to be calculated in good agreement with the experimental data. In consequence, both the temperature- and composition-induced structural changes of molten fuel slags can be described with a set of monomeric associate species in combination with the critical clusters induced by the self- and inter-polymerizations.

The new viscosity model has been developed for fully liquid slag system $\text{SiO}_2\text{--Al}_2\text{O}_3\text{--CaO--MgO--Na}_2\text{O--K}_2\text{O--FeO--Fe}_2\text{O}_3$ and its subsystems in the Newtonian range, based on the thermodynamic modified associate species model. The model gives a reliable prediction over the whole range of compositions and a broad range of temperatures using only one set of model parameters, which all have a clear physico-chemical meaning. With the new model, one of the challenges of the viscosity behavior in SiO_2 -based binary systems, the so called lubricant effect, can be excellently described. The viscosity behavior when substituting one network modifier for another at constant SiO_2 contents is well described. The Al_2O_3 -induced viscosity maximum is also well described, in which the position and magnitude of the viscosity maximum as a function of composition and temperature (charge compensation effect) are properly predicted. Another viscosity maximum when replacing Al_2O_3 with SiO_2 for constant contents of the network modifiers is presented. The Fe_2O_3 -induced charge compensation effect is less pronounced than that induced by Al_2O_3 . It was found that the Fe_2O_3 -induced viscosity maximum does not always occur depending on the charge compensators for Fe^{3+} . The viscosity maximum when replacing Fe_2O_3 with SiO_2 for constant contents of the other network modifiers might not occur.

In addition, a rotational viscometer is employed to validate the current viscosity model. Viscosities of several real coal ashes were measured by this rotational method. Moreover, examples of the application of the current model in determining coal ash fluxing and blending are presented.

Contents

Index of Figures.....	V
Index of Tables	XV
1 Introduction	1
2 Literature review	5
2.1 Fundamentals of rheological properties.....	5
2.1.1 Definition of viscosity	5
2.1.2 Rheological behavior	7
2.1.2.1 Newtonian fluid	7
2.1.2.2 Non-Newtonian fluid	8
2.2 Structure of slag	10
2.3 Previous viscosity models	15
2.3.1 Single phase slag systems.....	15
2.3.1.1 Temperature-related models	16
2.3.1.2 Composition- and temperature-related models	22
2.3.1.2.1 Non-structure based models	23
2.3.1.2.2 Structure based models	31
2.3.2 Multiphase slag systems	42
2.4 Methods of viscosity measurements.....	44
2.4.1 Rotating cylinder method	44
2.4.2 Falling body method.....	46
2.4.3 Capillary method	46
2.4.4 Parallel plates method	47
2.4.5 Rod elongation method	48
3 Experiments	51
4 Modelling	57
4.1 Model description	57
4.1.1 Structural dependence of viscosity	58
4.1.2 Common structural base between the viscosity and Gibbs energy	60

4.1.3	Description of the Gibbs energy using the modified associate species model	63
4.1.4	Linking the viscosity of slag to its structure	65
4.1.5	Viscosity of the pure oxides and binary systems.....	70
4.1.6	Viscosity of the multicomponent systems without Al_2O_3	71
4.1.7	Viscosity of the Al_2O_3 -containing multicomponent systems	72
4.1.8	Viscosity of the $\text{FeO}/\text{Fe}_2\text{O}_3$ -containing systems.....	76
4.2	Optimization procedure	79
5	Results and discussion	87
5.1	Pure oxides	91
5.1.1	SiO_2	91
5.1.2	Al_2O_3	92
5.1.3	CaO , MgO , Na_2O , and K_2O	93
5.2	Binary systems	94
5.2.1	SiO_2 – Al_2O_3 and Al_2O_3 – CaO	94
5.2.2	Al_2O_3 – MgO , Al_2O_3 – Na_2O , and Al_2O_3 – K_2O	97
5.2.3	SiO_2 – CaO and SiO_2 – MgO	98
5.2.4	SiO_2 – Na_2O and SiO_2 – K_2O	100
5.3	Multicomponent systems without Al_2O_3	102
5.3.1	SiO_2 – CaO – MgO	103
5.3.2	SiO_2 – CaO – Na_2O	105
5.3.3	SiO_2 – Na_2O – K_2O	106
5.3.4	SiO_2 – CaO – MgO – Na_2O – K_2O	108
5.4	Multicomponent systems with Al_2O_3	110
5.4.1	SiO_2 – Al_2O_3 – CaO and SiO_2 – Al_2O_3 – MgO	110
5.4.2	SiO_2 – Al_2O_3 – Na_2O and SiO_2 – Al_2O_3 – K_2O	115
5.4.3	SiO_2 – Al_2O_3 – CaO – MgO	122
5.4.4	SiO_2 – Al_2O_3 – CaO – Na_2O	123
5.4.5	SiO_2 – Al_2O_3 – Na_2O – K_2O	125
5.4.6	SiO_2 – Al_2O_3 – CaO – MgO – Na_2O – K_2O	127
5.5	The $\text{FeO}/\text{Fe}_2\text{O}_3$ -containing systems	130

5.5.1 The overall performance of the FeO/Fe ₂ O ₃ -containing systems	130
5.5.2 Discussion of the local viscosity maximum in the system SiO ₂ – FeO/Fe ₂ O ₃	133
5.5.3 Fe ₂ O ₃ -induced charge compensation effect.....	137
5.6 Viscosity of real coal ashes	141
5.7 Application of the current model in selection of coal ashes fluxing and blending.....	144
6 Conclusion and outlook	149
References	153
Appendix.....	167
Acknowledgements.....	169

Index of Figures

Fig. 1.1.	Schematic diagram of an IGCC power plant with carbon capture [2]	1
Fig. 1.2.	Presentation of GE Energy Gasifier [2]	2
Fig. 2.1.	Visualized concept of viscosity [17]	5
Fig. 2.2.	Qualitative flow curves for Newtonian fluid	7
Fig. 2.3.	Qualitative flow curves for varying non-Newtonian fluids [22]	8
Fig. 2.4.	Qualitative flow curves for thixotropic and rheopectic fluids [22]	9
Fig. 2.5.	Schematic of silica structure [24]	10
Fig. 2.6.	Modification of silica network structure by sodium [26]	11
Fig. 2.7.	Presentation of modified random network structure [27]	11
Fig. 2.8.	Proposed atomic arrangement of discrete silicon-oxide units in liquid silicates [28]	12
Fig. 2.9.	Loosening of the silica network structure by addition of alkali oxides and alkaline earth oxides	13
Fig. 2.10.	Presentation of atomic arrangement of the system $\text{Al}_2\text{O}_3\text{--CaO}$ at 0.375 mole fraction Al_2O_3 and 0.625 mole fraction CaO [29]	14
Fig. 2.11.	The behavior of Al_2O_3 as a network former in the systems $\text{SiO}_2\text{--Al}_2\text{O}_3\text{--MO/R}_2\text{O}$	14
Fig. 2.12.	Viscous forces are proposed to arise from momentum transfer between moving fluid layers when particles jump from one layer to another [47]	21
Fig. 2.13.	Schematic diagram of Q^n -groups [75]	37

Fig. 2.14. Presentation of internal structure and viscous flow in silicates, where: O^0 , O^- , and O^{2-} are the bridging, non-bridging, and free oxygen, respectively [76]	39
Fig. 2.15. Schematic diagram of the rotating cylinder method [87].....	45
Fig. 2.16. Schematic diagram of the capillary method [87].....	47
Fig. 2.17. Schematic diagram of the parallel plates method [90] and deformation of the sample [89].....	48
Fig. 3.1. Structure and schematic of the experimental setup for viscosity measurements.....	51
Fig. 3.2. Spindle and crucible	53
Fig. 3.3. Torque losses over rotational speed and time.....	54
Fig. 3.4. Temperature profile along a longitudinal axis	55
Fig. 3.5. Calibration and validation of viscometer	56
Fig. 4.1. Viscosity of the system SiO_2 – CaO at temperatures of $1600^\circ C$ and $1700^\circ C$ [91]	59
Fig. 4.2. Viscosity of polyvinylpyrrolidone solution of various concentrations at different temperatures [92]	60
Fig. 4.3. Second derivative of $\ln(\eta)$ with respect to mole fraction of SiO_2 at temperatures of $1950^\circ C$, $2000^\circ C$, and $2050^\circ C$ in the system SiO_2 – Al_2O_3	61
Fig. 4.4. Second derivative of $\ln(\eta)$ with respect to mole fraction of SiO_2 at temperatures of $1600^\circ C$, $1700^\circ C$, and $1800^\circ C$ in the system SiO_2 – CaO	62
Fig. 4.5. Second derivative of $\ln(\eta)$ with respect to mole fraction of SiO_2 at temperatures of $1300^\circ C$, $1400^\circ C$, and $1500^\circ C$ in the system SiO_2 – Na_2O ...	62

Fig. 4.6.	Accordance of the phase diagram of the system $\text{SiO}_2\text{--Al}_2\text{O}_3\text{--CaO}$ between experimental points (a) and model predictions (b)	64
Fig. 4.7.	Phase diagram of the system $\text{SiO}_2\text{--Al}_2\text{O}_3$ [98]	65
Fig. 4.8.	Structural representation of the associate species CaSiO_3 [106]	67
Fig. 4.9.	Normalized distribution of associate species for the system $\text{SiO}_2\text{--Na}_2\text{O}$	68
Fig. 4.10.	Normalized distribution of associate species in the fully liquid system $\text{SiO}_2\text{--CaO}$ at 2800°C	68
Fig. 4.11.	Normalized distribution of associate species in the fully liquid system $\text{SiO}_2\text{--CaO--Na}_2\text{O}$ at 2000°C and 0.50 mole fraction SiO_2	69
Fig. 4.12.	Viscosity comparison of the systems $\text{Al}_2\text{O}_3\text{--CaO}$ and $\text{SiO}_2\text{--CaO}$ at 1700°C for the same concentration of the tetrahedral structural units.....	74
Fig. 4.13.	The associate species distribution in the system $\text{Fe}_2\text{O}_3\text{--CaO}$	77
Fig. 4.14.	Presentation of the model development process.....	79
Fig. 4.15.	Comparison of the experimental data before and after selection in the system $\text{SiO}_2\text{--CaO}$ at 0.50 mole fraction SiO_2	81
Fig. 4.16.	Comparison of the experimental data before and after selection in the system $\text{SiO}_2\text{--CaO--MgO}$ at 0.40 mole fraction SiO_2 and 0.37 mole fraction CaO	81
Fig. 4.17.	The optimization process without and with the consideration of variable partial pressure of oxygen	85
Fig. 5.1.	Comparison between experimental data and calculated data for SiO_2	91
Fig. 5.2.	Comparison between experimental data and calculated data for Al_2O_3	92
Fig. 5.3.	Viscosities of the pure oxides SiO_2 , Al_2O_3 , CaO , MgO , Na_2O , and K_2O	93

Fig. 5.4.	Comparison between experimental data and calculated data in the system $\text{SiO}_2\text{--Al}_2\text{O}_3$	95
Fig. 5.5.	The effect of self-polymerization of SiO_2 on viscosity	95
Fig. 5.6.	Comparison between experimental data and calculated data in the system $\text{Al}_2\text{O}_3\text{--CaO}$	96
Fig. 5.7.	Charge compensation effect in the systems $\text{Al}_2\text{O}_3\text{--MgO}$, $\text{Al}_2\text{O}_3\text{--Na}_2\text{O}$, and $\text{Al}_2\text{O}_3\text{--K}_2\text{O}$	97
Fig. 5.8.	Normalized distribution of associate species in the systems $\text{Al}_2\text{O}_3\text{--K}_2\text{O}$ and $\text{Al}_2\text{O}_3\text{--Na}_2\text{O}$	98
Fig. 5.9.	Comparison between experimental data and calculated data in the system $\text{SiO}_2\text{--CaO}$	99
Fig. 5.10.	Comparison between experimental data and calculated data in the system $\text{SiO}_2\text{--MgO}$	100
Fig. 5.11.	Comparison between experimental data and calculated data in the system $\text{SiO}_2\text{--Na}_2\text{O}$	101
Fig. 5.12.	Comparison between experimental data and calculated data in the system $\text{SiO}_2\text{--K}_2\text{O}$	101
Fig. 5.13.	Formation of ring structure for the monomeric associate species	102
Fig. 5.14.	Comparison between experimental data and calculated data in the system $\text{SiO}_2\text{--CaO--MgO}$ at 1400°C , 1500°C , 1600°C , 1700°C , and 1800°C for the SiO_2 content of 0.50 mole fraction	103
Fig. 5.15.	Comparison between experimental data and calculated data in the system $\text{SiO}_2\text{--CaO--MgO}$ at 1600°C for the SiO_2 contents of 0.30, 0.40, 0.50, 0.60, and 0.70 mole fraction	104

Fig. 5.16. Comparison between experimental data and calculated data in the system $\text{SiO}_2\text{--CaO--Na}_2\text{O}$ at 1100°C, 1200°C, 1300°C, and 1400°C for the SiO_2 content of 0.75 mole fraction	105
Fig. 5.17. Comparison between experimental data and calculated data in the system $\text{SiO}_2\text{--CaO--Na}_2\text{O}$ at 1300°C for the SiO_2 contents of 0.30, 0.40, 0.50, 0.60, and 0.70 mole fraction	106
Fig. 5.18. Comparison between experimental data and calculated data in the system $\text{SiO}_2\text{--Na}_2\text{O--K}_2\text{O}$ at 1100°C, 1200°C, 1300°C, and 1400°C for the SiO_2 content of 0.75 mole fraction	107
Fig. 5.19. Comparison between experimental data and calculated data in the system $\text{SiO}_2\text{--Na}_2\text{O--K}_2\text{O}$ at 1300°C for the SiO_2 contents of 0.300, 0.400, 0.500, 0.600, 0.667, 0.743, 0.800, and 0.900 mole fraction	108
Fig. 5.20. Comparison between experimental data and calculated data in the system $\text{SiO}_2\text{--CaO--MgO--Na}_2\text{O--K}_2\text{O}$ for 0.730 mass fraction SiO_2 , 0.055 mass fraction CaO , 0.035 mass fraction MgO as well as 0.20, 2.00, and 3.50 mass ratio $\text{Na}_2\text{O/K}_2\text{O}$	109
Fig. 5.21. Comparison between experimental data and calculated data in the system $\text{SiO}_2\text{--Al}_2\text{O}_3\text{--CaO}$ at 1400°C, 1600°C, 1800°C, and 2000°C for the SiO_2 content of 0.50 mole fraction	111
Fig. 5.22. Comparison between experimental data and calculated data in the system $\text{SiO}_2\text{--Al}_2\text{O}_3\text{--CaO}$ at 1600°C for the SiO_2 contents of 0.40, 0.50, 0.67, and 0.75 mole fraction	112
Fig. 5.23. Comparison between experimental data and calculated data in the system $\text{SiO}_2\text{--Al}_2\text{O}_3\text{--CaO}$ at 1 mole ratio $\text{Al}_2\text{O}_3/\text{CaO}$ for the SiO_2 contents of 0.25, 0.50, and 0.75 mole fraction	113

Fig. 5.24. Comparison between experimental data and calculated data in the system $\text{SiO}_2\text{--Al}_2\text{O}_3\text{--MgO}$ at 1 mole ratio $\text{Al}_2\text{O}_3/\text{MgO}$ for the SiO_2 contents of 0.25, 0.50, and 0.75 mole fraction.....	113
Fig. 5.25. Comparison between experimental data and calculated data in the system $\text{SiO}_2\text{--Al}_2\text{O}_3\text{--MgO}$ at 1500°C, 1600°C, 1700°C, and 1800°C for the SiO_2 content of 0.50 mole fraction.....	114
Fig. 5.26. Comparison between experimental data and calculated data in the system $\text{SiO}_2\text{--Al}_2\text{O}_3\text{--MgO}$ at 1600°C for the SiO_2 contents of 0.45, 0.50, 0.60, 0.67, and 0.75 mole fraction.....	115
Fig. 5.27. Comparison between experimental data and calculated data in the system $\text{SiO}_2\text{--Al}_2\text{O}_3\text{--Na}_2\text{O}$ at 1600°C for the SiO_2 contents of 0.40, 0.50, 0.60, 0.67, 0.75, and 0.82 mole fraction.....	116
Fig. 5.28. Schematic presentation of a tricluster species $\text{AlSi}_2\text{O}_{5.5}$	117
Fig. 5.29. Comparison between experimental data and calculated data in the system $\text{SiO}_2\text{--Al}_2\text{O}_3\text{--Na}_2\text{O}$ at 1000°C, 1200°C, 1400°C, and 1600°C for the SiO_2 content of 0.67 mole fraction.....	118
Fig. 5.30. Comparison between experimental data and calculated data in the system $\text{SiO}_2\text{--Al}_2\text{O}_3\text{--Na}_2\text{O}$ at 1 mole ratio $\text{Al}_2\text{O}_3/\text{Na}_2\text{O}$ for the SiO_2 contents of 0.50, 0.60, 0.67, 0.75, and 0.83 mole fraction.....	119
Fig. 5.31. Comparison between experimental data and calculated data in the system $\text{SiO}_2\text{--Al}_2\text{O}_3\text{--K}_2\text{O}$ at 1 (or 0.06) mole ratio $\text{Al}_2\text{O}_3/\text{K}_2\text{O}$ for the SiO_2 contents of 0.55 and 0.75 mole fraction.....	119
Fig. 5.32. Comparison between experimental data and calculated data in the system $\text{SiO}_2\text{--Al}_2\text{O}_3\text{--K}_2\text{O}$ at 1400°C (or 1300°C) for the SiO_2 contents of 0.55, 0.60, 0.65, and 0.70 mole fraction.....	120

Fig. 5.33. Comparison between experimental data and calculated data in the system $\text{SiO}_2\text{--Al}_2\text{O}_3\text{--K}_2\text{O}$ at 1200°C, 1250°C, 1300°C, 1350°C, and 1400°C for the SiO_2 content of 0.60 mole fraction	121
Fig. 5.34. Comparison between experimental data and calculated data in the system $\text{SiO}_2\text{--Al}_2\text{O}_3\text{--CaO--MgO}$ at 1400°C, 1500°C, and 1600°C as well as 0.50 mole fraction SiO_2 and 0.25 mole fraction CaO	122
Fig. 5.35. Comparison between experimental data and calculated data in the system $\text{SiO}_2\text{--Al}_2\text{O}_3\text{--CaO--MgO}$ at 1500°C as well as 0.05 mass fraction MgO and 0.30, 0.35, 0.40, 0.45, 0.50, 0.55, and 0.60 mass fraction SiO_2	123
Fig. 5.36. Comparison between experimental data and calculated data in the system $\text{SiO}_2\text{--Al}_2\text{O}_3\text{--CaO--Na}_2\text{O}$ for the SiO_2 contents of 0.501, 0.548, 0.644, and 0.729 mole fraction	124
Fig. 5.37. Comparison between experimental data and calculated data in the system $\text{SiO}_2\text{--Al}_2\text{O}_3\text{--CaO--Na}_2\text{O}$ at 1300°C, 1350°C, and 1400°C as well as 0.2115 mass fraction CaO and 0.0385 mass fraction Na_2O	125
Fig. 5.38. Comparison between experimental data and calculated data in the system $\text{SiO}_2\text{--Al}_2\text{O}_3\text{--Na}_2\text{O--K}_2\text{O}$ at 1 mole ratio $\text{Al}_2\text{O}_3/(\text{Na}_2\text{O}+\text{K}_2\text{O})$ for the SiO_2 contents of 0.688 and 0.847 mole fraction	126
Fig. 5.39. Comparison between experimental data and calculated data in the system $\text{SiO}_2\text{--Al}_2\text{O}_3\text{--Na}_2\text{O--K}_2\text{O}$ at 1000°C, 1200°C, and 1400°C as well as 0.125 mole fraction Na_2O and 0.125 mole fraction K_2O	127
Fig. 5.40. Comparison between experimental data and calculated data in the system $\text{SiO}_2\text{--Al}_2\text{O}_3\text{--CaO--MgO--Na}_2\text{O--K}_2\text{O}$ for the SiO_2 contents of 0.605, 0.732, and 0.746 mole fraction	128
Fig. 5.41. Comparison between experimental data and calculated data in the system $\text{SiO}_2\text{--Al}_2\text{O}_3\text{--CaO--MgO--Na}_2\text{O--K}_2\text{O}$ at 1300°C	129

Fig. 5.42. Comparison between experimental data and calculated data in the system $\text{SiO}_2\text{--Al}_2\text{O}_3\text{--CaO--FeO}$ at 1450°C	131
Fig. 5.43. Comparison between experimental data and calculated data in the system $\text{SiO}_2\text{--Al}_2\text{O}_3\text{--CaO--FeO}$ at 1500°C	131
Fig. 5.44. Comparison between experimental data and calculated data in the systems $\text{SiO}_2\text{--CaO--FeO}$, $\text{SiO}_2\text{--MgO--FeO}$, $\text{SiO}_2\text{--Al}_2\text{O}_3\text{--FeO}$, and $\text{SiO}_2\text{--CaO--MgO--FeO}$	132
Fig. 5.45. Comparison between experimental data and calculated data in the system $\text{SiO}_2\text{--MgO--K}_2\text{O--FeO}$	133
Fig. 5.46. Viscosity maximum in the systems $\text{Fe}_2\text{O}_3\text{--CaO}$ and $\text{Fe}_2\text{O}_3\text{--Na}_2\text{O}$	134
Fig. 5.47. The associate species distribution in the system $\text{SiO}_2\text{--Fe}_2\text{O}_3$	135
Fig. 5.48. The local viscosity maximum in the system $\text{SiO}_2\text{--Fe}_2\text{O}_3$	136
Fig. 5.49. The charge compensation effect in the systems $\text{Fe}_2\text{O}_3\text{--CaO}$ and $\text{Fe}_2\text{O}_3\text{--Na}_2\text{O}$	137
Fig. 5.50. The charge compensation effect in the system $\text{SiO}_2\text{--Al}_2\text{O}_3\text{--FeO}$	138
Fig. 5.51. The charge compensation effect in the systems $\text{SiO}_2\text{--Fe}_2\text{O}_3\text{--Na}_2\text{O/K}_2\text{O}$.	139
Fig. 5.52. The viscosity behavior with the substitution of SiO_2 for Fe_2O_3 in the system $\text{SiO}_2\text{--Fe}_2\text{O}_3\text{--Na}_2\text{O--K}_2\text{O}$	139
Fig. 5.53. The viscosity of the $\text{Al}_2\text{O}_3/\text{Fe}_2\text{O}_3$ -containing slags.....	141
Fig. 5.54. Comparison between experimental data and calculated data for the coal ashes K2-5, S1-1, S1-2, and S1-4	142
Fig. 5.55. Iso-viscosity lines and viscosity surface in the systems $\text{SiO}_2\text{--Al}_2\text{O}_3$, $\text{Al}_2\text{O}_3\text{--CaO}$, and $\text{SiO}_2\text{--Al}_2\text{O}_3\text{--CaO}$	144

Fig. 5.56. Iso-viscosity lines and viscosity surface in the system $\text{SiO}_2\text{--Al}_2\text{O}_3\text{--CaO--MgO--Na}_2\text{O--K}_2\text{O}$ at 1600°C as well as 0.1 mole fraction Na_2O , 0.1 mole fraction K_2O , and 0.2 mole fraction MgO	145
Fig. 5.57. Principle of coal ashes bending.....	146

Index of Tables

Table 2.1. Approximate viscosities for some common substances at room temperature [19]	6
Table 2.2. Previous viscosity models presented in this section	15
Table 2.3. The composition range used for the development of the Lakatos model	25
Table 2.4. The composition range suitable for the Riboud model	28
Table 4.1. Structural change with respect to CaO content in SiO ₂ –CaO melts	58
Table 4.2. Definition of associate species and structural units for pure oxides and binary systems	66
Table 4.3. The Al ³⁺ -containing associate species and structural units	73
Table 4.4. The Fe-containing associate species and structural units	78
Table 4.5. Summary of experimental data used for pure oxides and binary systems in the system SiO ₂ –Al ₂ O ₃ –CaO–MgO–Na ₂ O–K ₂ O	80
Table 5.1. Optimized model parameters as well as predicted theoretical viscosity and activation energy of viscous flow for pure oxides and binary systems..	87
Table 5.2. Optimized model parameters as well as predicted theoretical viscosity and activation energy of viscous flow for ternary or higher order systems ..	89
Table 5.3. Composition of four synthetic slags (mole fraction)	140
Table 5.4. Main components of four coal ashes (mole fraction)	142

1 Introduction

Coal is the world's most abundant and widely distributed fossil fuel, which maintains around 41% of the power generation in the world. Despite a strong development of renewables such as solar, wind, and geothermal energies, coal will continue to play an essential role in power generation for the foreseeable future. The utilization of coal, however, causes a remarkable increase in carbon dioxide emissions, which has a significant contribution to the global warming. Reducing carbon dioxide emissions requires technologies that allow a cleaner and more efficient utilization of coal. Coal-fired power plants using integrated gasification combined cycle (IGCC) technology in combination with carbon capture are identified as a promising solution to achieve these goals [1], as shown in **Fig. 1.1**.

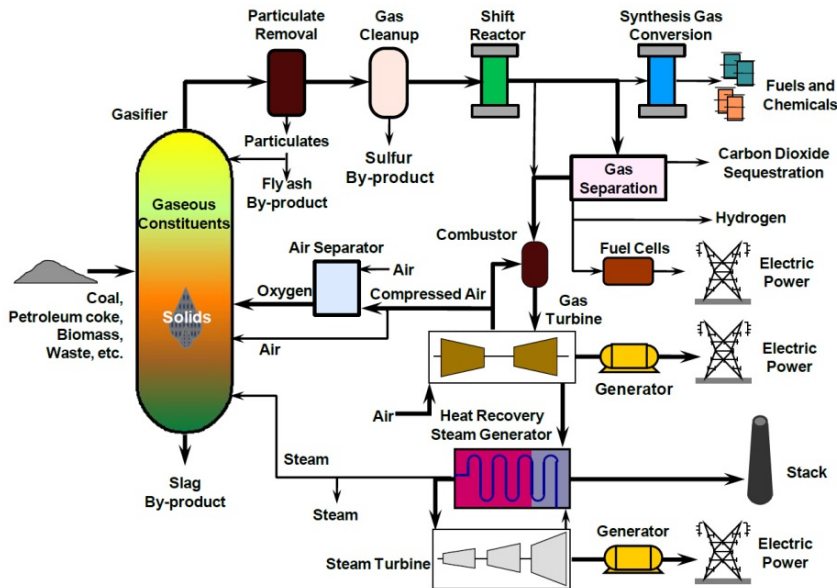


Fig. 1.1. Schematic diagram of an IGCC power plant with carbon capture [2]

The core of an IGCC power plant is the gasifier, whose performance is significant for the IGCC power plant. Many types of gasifiers have been developed so far, for instance, moving-bed, fluid-bed, and entrained-flow gasifiers. However, the majority of the

successful coal gasification processes developed after 1950 are performed by entrained-flow slagging gasifiers, which are operated at temperatures above 1400°C and pressures ranging from 2 MPa to 7 MPa [3]. As an example, the GE Energy gasifier (see **Fig. 1.2**) is currently employed by 64 plants, and moreover 6 more plants are in planning [2].

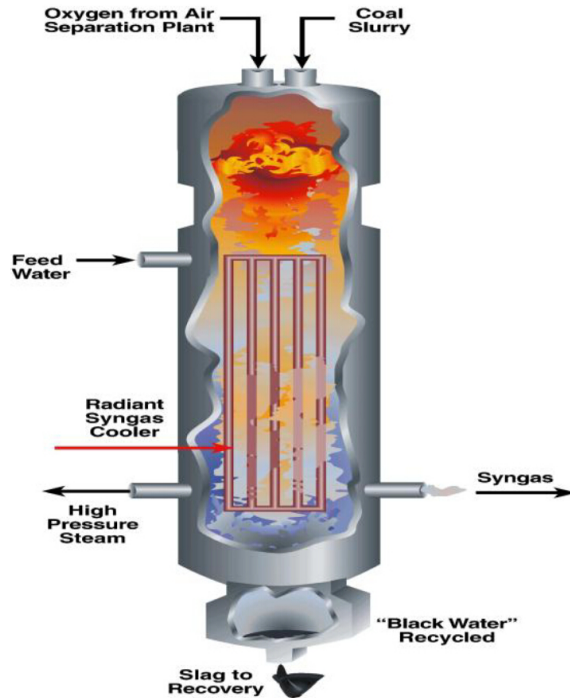


Fig. 1.2. Presentation of GE Energy Gasifier [2]

In slagging gasifiers, the organic components in coal particles are converted to syngas, which is used for electricity generation. The majority of the inorganic components are converted to a liquid slag flowing down the wall of the gasifier, whereas the remaining inorganic components entrained in the syngas form fly ash. Slag viscosity plays a very important role in determining the optimum operating conditions for slagging gasification, in which many processes such as the particle sticking (or droplet sticking), slag flow, slag tapping, and refractory degradation are related to the viscosity [4]. Slag viscosity is

strongly dependent on composition and temperature. When the operating temperature is optimized for the syngas production, blended coals or fluxing agents are often used to make the slag viscosity low enough for efficient slag flow and tapping [5, 6]. For smooth slag flow and tapping, the maximum slag viscosity is 25 Pa·s [7]. On the other hand, an increased viscosity is required to decrease the corrosion rate to protect the refractory material of the gasifier [8]. Moreover, the viscosity is an important factor in designing the slagging gasifiers [9].

Although extensive measurements of slag viscosities have been made so far, it is impossible to give all data for the range of compositions and temperatures encountered in practice. In addition, measuring viscosity is not only time consuming but also expensive. To solve this problem, modelling of viscosities is a proper and promising approach. A number of viscosity models such as the Arrhenius model [10], the Weymann-Frenkel model [11], the Lakatos model [12], the Urbain model [13], the Riboud model [14], and the Reddy model [15] have been developed for several past decades. Most of the early models, however, involve a longstanding problem that they are only capable of describing the viscosity over a limited range of compositions and temperatures, due to the lack of an effective description about the structural dependence of viscosity. Thus, a reliable, accurate, and general model is required to describe the viscosity over the whole range of compositions and a broad range of temperatures for proper selection of operating temperature, blended coals, and fluxing agents. Moreover, a proper viscosity model should be implemented for simulations based on computational fluid dynamics (CFD) [16].

This study aims at developing a new structure based viscosity model in the Newtonian range, which can describe viscosities of liquid melts for the system $\text{SiO}_2\text{--Al}_2\text{O}_3\text{--CaO--MgO--Na}_2\text{O--K}_2\text{O--FeO--Fe}_2\text{O}_3$ and its subsystems relevant to fuel slags. The model should be applicable in the whole range of compositions and a broad range of temperatures encountered in slagging gasification, which requires an effective description about the structure of the slag. In the current model the viscosity is linked to the type and distribution of species, as well as the connectivity of species. The type of species is determined from the Gibbs energy, and thereby the distribution of species is

calculated by using a completely self-consistent thermodynamic dataset, where the modified associate species model was applied for the slag. It is assumed that both the temperature- and composition-induced structural changes of molten fuel slags can be described with a set of monomeric associate species in combination with the critical clusters induced by the self- and inter-polymerizations. More than 7700 experimental data points are used to assess the model parameters.

In addition, a rotational viscometer is employed to measure the viscosity, which is used for validation of the current model. Viscosities of several real coal ashes were measured by this rotational method. Moreover, examples of the application of the current model in determining coal ash fluxing and blending are presented.

2 Literature review

2.1 Fundamentals of rheological properties

2.1.1 Definition of viscosity

Viscosity can be considered as an internal fluid friction, which can transform kinetic energy of macroscopic motion into heat energy like the friction between moving solids. There is no such friction in a liquid as static friction between two solids. However, there is, instead, dynamic friction due to the random motion of species (i.e. atoms, molecules, or ions) in a liquid. The causes of viscosity, essentially, are the transfer of momentum between species and the inter-species forces between species of the liquid.

In terms of the quantitative description of viscosity, Newton conducted a simple experiment in which the fluid is sandwiched between two suspending parallel horizontal plates in a liquid. The viscosity is described as the shear stress that suppresses the movement of these two suspending parallel horizontal plates, which is illustrated in **Fig. 2.1**.

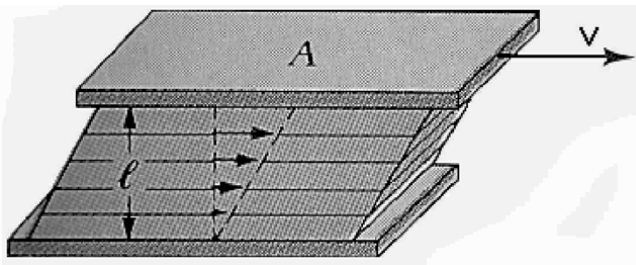


Fig. 2.1. Visualized concept of viscosity [17]

The lower plate is fixed while the upper plate is pulled slowly at a constant speed. After a steady state is reached, the fluid can be imaged to be composed of many layers like a pile of printer paper, where each sheet moves a little faster than the sheet below it. In other words, the fluid between the plates flows in lamina and its speed distribution is linear, which is proportional to the distance from the lower plate.

As **Fig. 2.1** presents, the viscosity can be calculated with [18]

$$\tau = \frac{F}{A} = \eta \cdot \frac{v}{\ell} \quad (2.1)$$

where: τ is the shear stress; F is the force required to move the upper plate; A is the area of the plate; η is the viscosity; v is the speed of plate; ℓ is the distance between the plates. This equation was verified by Poiseuille in 1849, based on the experiment of liquid flow in tubes.

The SI unit of the viscosity is $\text{Pa}\cdot\text{s}$, which is used in this thesis. It is necessary to point out another unit, poise (P), named after Poiseuille, which is usually applied in industry. The relation between P and $\text{Pa}\cdot\text{s}$ is shown in Eq. (2.2).

$$1 \text{ Pa}\cdot\text{s} = 10 \text{ P} \quad (2.2)$$

To get a rough picture of the degree of viscosities, viscosities of some common substances are shown in **Table 2.1**. Moreover, the viscosity studied in this thesis is always dynamic viscosity, although there is another term, kinetic viscosity, which is used to describe the ability of the fluid to transport momentum, and it is defined as the ratio of dynamic viscosity to density.

Table 2.1. Approximate viscosities for some common substances at room temperature [19]

Material	$\log \eta \text{ (Pa}\cdot\text{s)}$
Ideal fluid	$-\infty$
Water	-3
Machine oil	-1
Heavy oil	0
Glycerol	1
Solid glass	>18

2.1.2 Rheological behavior

Viscosity is strongly related to the rheological behavior of a liquid. There is no general model to calculate the viscosity for all types of rheological behaviors [20], which is extremely complicated. The evaluation of flow type is required to develop a new viscosity model. According to the relationship between shear rate and viscosity, the fluid is classified as two categories: Newtonian fluid and non-Newtonian fluid.

2.1.2.1 Newtonian fluid

The Newtonian fluid behavior is characterized by a linear relationship between the applied shear stress and shear rate [21]. That is, the viscosity remains constant as the change in shear rate occurs for the Newtonian fluid, which is illustrated in **Fig. 2.2**.

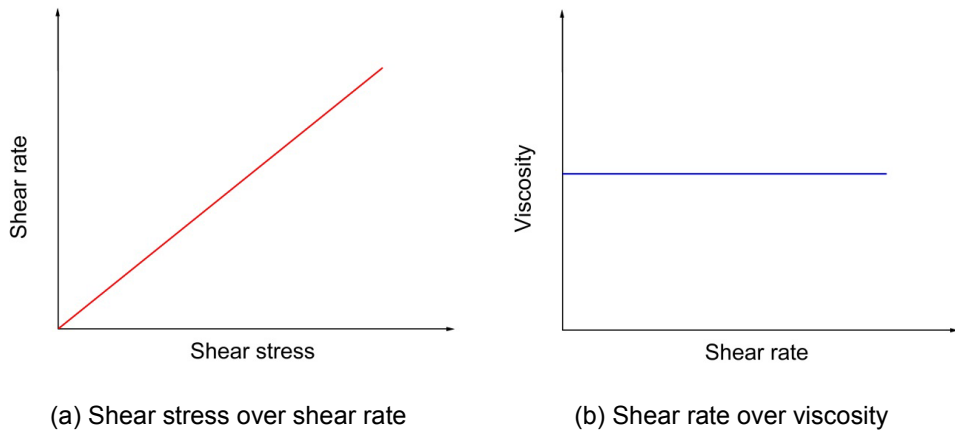


Fig. 2.2. Qualitative flow curves for Newtonian fluid

In 2010, Chhabra gave a more complete definition where a Newtonian fluid should satisfy the complete Navier-Stokes equations rather than simply present a constant viscosity at varying shear rates [22]. The present viscosity modelling is subjected to the Newtonian fluid.

2.1.2.2 Non-Newtonian fluid

For non-Newtonian fluid behavior, the viscosity is dependent on the shear rate. The relationship between the shear stress and shear rate is no longer linear for non-Newtonian fluid [21]. There are several types of non-Newtonian fluid, which can be further classified as a time-dependent fluid and a time-independent fluid.

For the time-independent fluid, as the name implies, the fluid behavior is independent on time. The common types of this fluid are shown in **Fig. 2.3**.

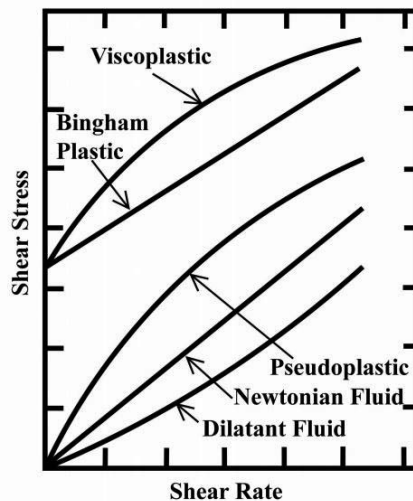


Fig. 2.3. Qualitative flow curves for varying non-Newtonian fluids [22]

A pseudoplastic fluid, which is perhaps the most common non-Newtonian fluid, is characterized by the phenomena that viscosity decreases with increasing shear rate. It is encountered in many types of fluids, such as emulsions and dispersions. Conversely, a dilatant fluid displays increasing viscosity with increasing shear rate, as presented in **Fig. 2.3**. It can be observed in concentrated suspensions like a mixture of water and silver sand.

A bingham plastic fluid, as shown in **Fig. 2.3**, behaves like a solid at low shear stress but behaves like Newtonian fluid at high shear stress, where the critical shear stress is

called yield stress and the slope of line is called plastic viscosity. In contrast, a viscoplastic fluid, which is also characterized by the existence of a yield stress, reveals a decrease in plastic viscosity as the shear rate increases.

Some non-Newtonian fluids show a change in viscosity with time at constant shear rate. According to the behavior of shear stress-shear rate over duration of shearing, time-dependent fluids are described as two types, i.e. a thixotropic fluid and a rheopectic fluid, as presented in **Fig. 2.4**.

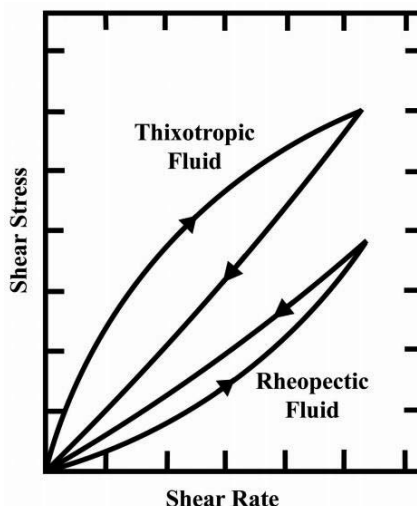


Fig. 2.4. Qualitative flow curves for thixotropic and rheopectic fluids [22]

Thixotropic fluids, such as paints and clays, present a decrease in viscosity with time at constant shear rate but show a recovery of the viscosity once the shear load is removed [23], as shown in **Fig. 2.4**. Rheopectic fluids, which are rarely encountered compared to thixotropic fluids, display the opposite phenomenon that viscosity increases over the duration of shearing. In addition, it is not uncommon that both thixotropic and rheopectic behaviors can be observed in the same liquid under appropriate conditions [22].

2.2 Structure of slag

When it comes to the viscosity of slag, the structure of slag is inevitable to be considered due to the essential dependence of the viscosity on structure. Slag can be treated as the mixture of oxides, such as SiO_2 , Al_2O_3 , CaO , MgO , Na_2O , K_2O , FeO , and Fe_2O_3 , with ignoring the slight amount of sulphides as well as phosphides. The structure of each pure oxide is related to the radius ratio of cation and anion. According to the specific effects of oxides on the slag structure, they are categorized as three groups, i.e. network formers (e.g. SiO_2), network modifiers (e.g. CaO , MgO , Na_2O , K_2O , and FeO) and amphoteric (e.g. Al_2O_3 and Fe_2O_3).

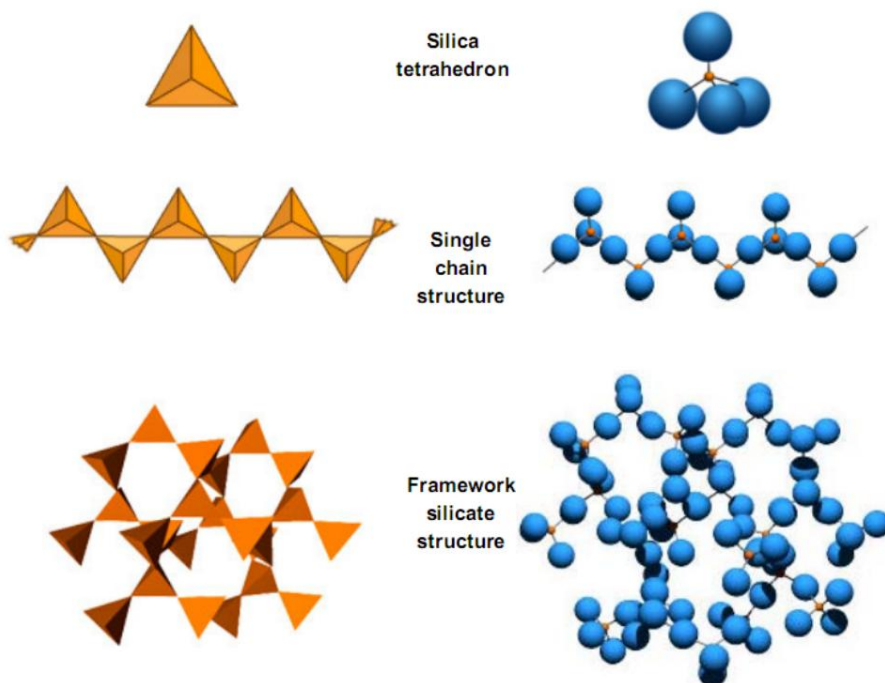


Fig. 2.5. Schematic of silica structure [24]

In the 1930s, the silicate structure was extensively investigated by Zachariasen [25] and Warren and Bischoff [26], who found three rules for describing the atomic arrangement in

vitreous silicates through X-ray diffraction experiments. Firstly, the silicon ion is tetrahedrally surrounded by four oxygen ions. Secondly, there is no more than one oxygen ion between two adjacent silicon ions. Finally, every oxygen ion is linked to the silicon ion or some other cations. Thus, the silica tetrahedron, single chain structure, and framework silica structure are pictured as shown in **Fig. 2.5**. These covalent structures give several macroscopic features. They are very hard in the solid state, and the viscosity of molten pure silica is very high compared to other melts due to the fact that the bonds are still strong in the liquid state [17].

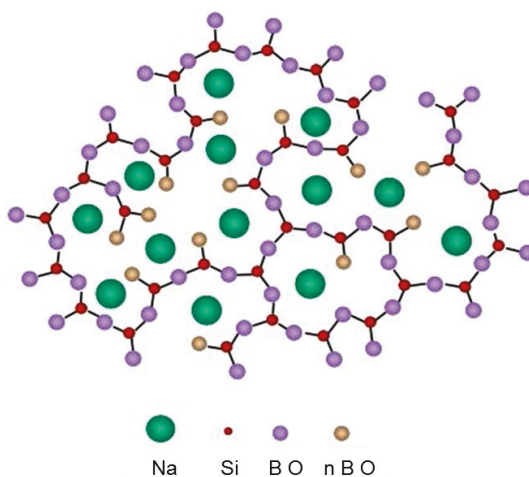


Fig. 2.6. Modification of silica network structure by sodium [26]

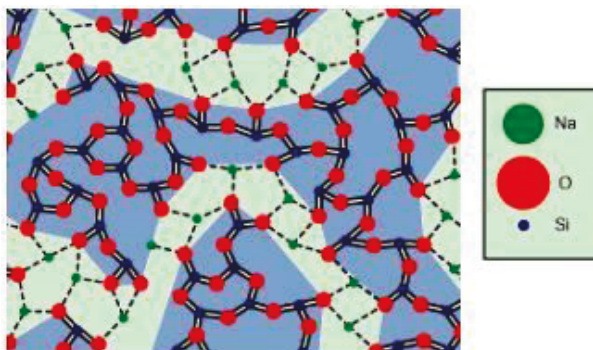


Fig. 2.7. Presentation of modified random network structure [27]

However, the covalent bond of oxygen and silicon can be broken by addition of network modifiers. In 1938, the modification of silica network structure was postulated by Warren and Bischoff based on the study of sodium silicate glass, which is presented in **Fig. 2.6**. It is seen that the oxygen ions are not always bonded to two silicon ions, and sodium ions are presented in various holes in the irregular network structure. In 1985, Greaves further investigated the effect of the network modifiers on the structure of glass. Then, he proposed modified random network structure, as shown in **Fig. 2.7**.

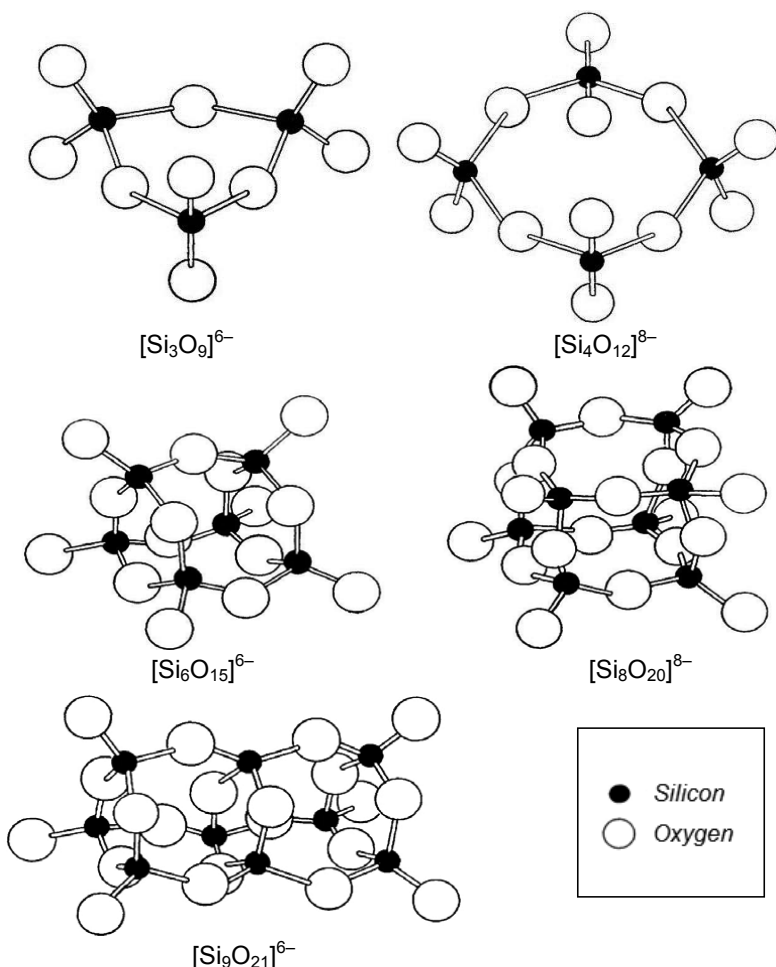


Fig. 2.8. Proposed atomic arrangement of discrete silicon-oxide units in liquid silicates [28]

In 1955, Bockris et al. put forward the discrete silicon-oxide units in liquid silicates after collapse of silica network structure, as shown in **Fig. 2.8**. These proposed discrete units are capable of describing changes in molar volume as well as the activation energy for viscous flow over composition [28].

Based on empirical observations, Zachariasen also found that network formers usually involve four features [25]. No oxygen ions may be bonded to more than two cations; the cation coordination number is small (3 or 4); oxygen polyhedral share corners rather than edges or faces; at least three corners must be shared for 3-dimensional network structure. The alkali oxides and alkaline earth oxides are considered as network modifiers based on the features of network formers. Each alkali ion results in one break of covalent bonds while each alkaline earth ion leads to two breaks of covalent bonds, as **Fig. 2.9** illustrates.

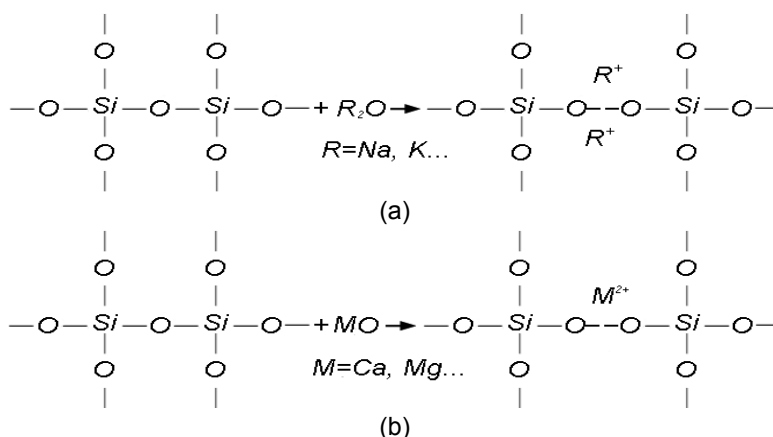


Fig. 2.9. Loosening of the silica network structure by addition of alkali oxides and alkaline earth oxides

According to the principles shown in **Fig. 2.9**, addition of the network modifiers, such as alkali oxides and alkaline earth oxides, to pure silica will cause a sharp decrease in viscosity.

In terms of amphoteric oxides like Al_2O_3 , as the name itself implies, they behave as either network formers or network modifiers depending on the composition of the silicate melts. For example, the viscosity decreases with increasing content of Al_2O_3 in the binary

system $\text{SiO}_2\text{--Al}_2\text{O}_3$ in which Al_2O_3 acts as a network modifier. For the binary system $\text{Al}_2\text{O}_3\text{--CaO}$, however, it can behave as a network former as shown in **Fig. 2.10**, where Al^{3+} is charge-compensated by Ca^{2+} and results in a viscosity maximum which here is also called charge compensation effect.

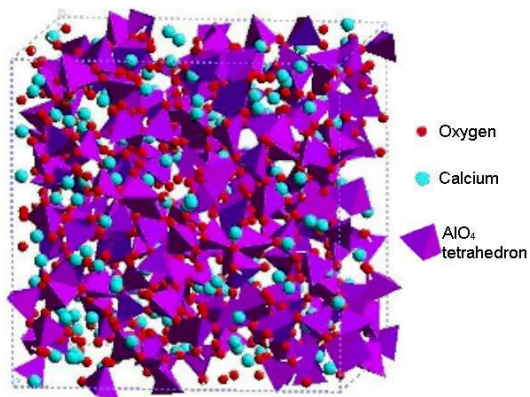


Fig. 2.10. Presentation of atomic arrangement of the system $\text{Al}_2\text{O}_3\text{--CaO}$ at 0.375 mole fraction Al_2O_3 and 0.625 mole fraction CaO [29]

In ternary systems such as $\text{SiO}_2\text{--Al}_2\text{O}_3\text{--MO/R}_2\text{O}$, the Al_2O_3 -induced viscosity behavior is complicated depending on relative concentrations of each component [30]. As **Fig. 2.11** presents, different charge compensators lead to different structural changes.

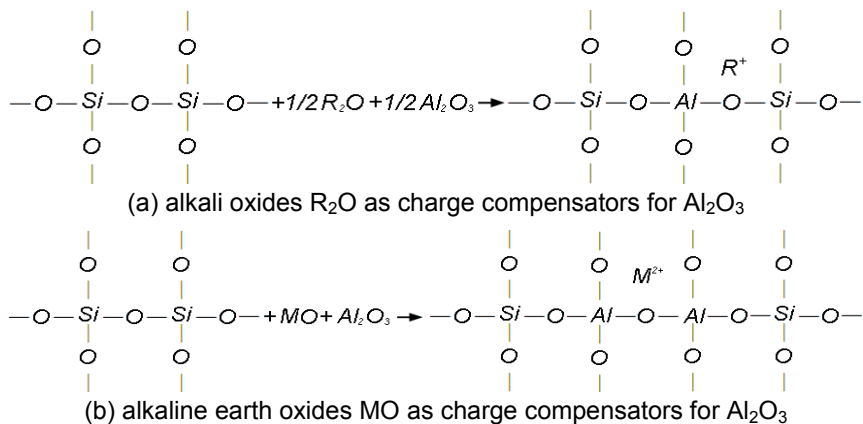


Fig. 2.11. The behavior of Al_2O_3 as a network former in the systems $\text{SiO}_2\text{--Al}_2\text{O}_3\text{--MO/R}_2\text{O}$

2.3 Previous viscosity models

Many efforts have been made to develop various models for the prediction of viscosity in past decades. Most of them are only applicable in a special range of compositions or temperatures. Some common previous models are listed in **Table 2.2**, and described in detail as follows.

Table 2.2. Previous viscosity models presented in this section

Single phase slag systems			
Temperature-related models	Temperature & Composition-related models		Multiphase slag systems
	Non-structure based models	Structure based models	
Arrhenius model	Shaw model	Zhang-Jahanshahi model	Einstein model
Vogel-Fulcher-Tammann model	Lakatos model	Reddy model	Roscoe model
Adam-Gibbs model	Urbain model	Iida model	
Eyring model	Riboud model	KTH model	
Weymann-Frenkel model	Kalmanovitch-Frank model	Avramov model	
Bockris-Reddy model	Hurst model	Quasi-chemical viscosity model	
AM model	Kondratiev-Jak model	FactSage model	

2.3.1 Single phase slag systems

This section focuses on describing the viscosity models for fully liquid systems where rheological behavior is constrained within the Newtonian fluid. In an earlier stage, the temperature dependence of viscosity was widely investigated and many temperature-related models were developed. Considering the temperature dependence only, was not sufficient and therefore the effect of the composition on viscosity was coupled to the

viscosity models. Due to the fact that the structure plays an essential role in viscosity, structure based models were adopted to describe the viscosity, later on.

2.3.1.1 Temperature-related models

Extensive efforts on temperature dependence of viscosity have been made since the end of 19th century [20]. What is well known at present are the Arrhenius model, the Vogel-Fulcher-Tammann model, the Adam-Gibbs model, the Eyring model, the Weymann-Frenkel model, the Bockris-Reddy model, and the AM model.

Arrhenius model

This model is a widely known approach, which is often employed to describe the temperature dependence of viscosity for silicate melts. At the end of the 19th century, an internal friction of dilute aqueous solutions was investigated by Arrhenius [10]. He found that the internal friction (viscosity) exhibits a temperature-dependent behavior and obeys Eq. (2.3).

$$\ln \eta = A + \frac{B}{T} \quad (2.3)$$

where: η is the viscosity; A and B are composition-dependent constants; T is the absolute temperature in K.

As the definition of viscosity says, viscous flow can be described as relative movements of the structural units of the liquid in the view of molecular scale. Based on the Eyring absolute rate theory [31], the precondition for the displacement of structural units is to overcome the potential energy barriers, which are dependent on composition. Then, a more complicated form of the Arrhenius model was derived as follows [32].

$$\ln \eta = A_a + \frac{E_a}{R \cdot T} \quad (2.4)$$

where: A_a and E_a are composition-dependent constants; R is the gas constant.

There are many arguments in terms of the constants A and B. The relationship between $\ln \eta$ and $1/T$ is usually nonlinear. In 1986, Richet observed that the constant B is dependent on temperature [33]. Afterwards, Wang and Porter characterized the constant B as a temperature and composition-related parameter for polymer systems in 1995 [34].

Vogel-Fulcher-Tammann model

This model was independently put forward by Vogel [35], Fulcher [36], and Tammann and Hesse [37]. Compared to the Arrhenius model, it introduces another constant parameter C besides the constants A and B, which is expressed as

$$\ln \eta = A + \frac{B}{T - C} \quad (2.5)$$

where: A, B, and C are composition-dependent constants.

It is suitable to demonstrate the dependence of viscosity on temperature for silicate melts. In 1985, Urbain found that the Vogel-Fulcher-Tammann model shows a good agreement between experimental data and calculated results for fully liquid silicates, supercooled liquids, and glasses [38]. This model is also employed by Gan and Lai to describe the temperature dependence of viscosity for molten blast furnace slag and gives a good performance [39]. However, Mauro et al. stated that the Vogel-Fulcher-Tammann model exhibits systematic error when extrapolating to low temperatures [40].

Adam-Gibbs model

In 1965, another model, i.e. the Adam-Gibbs model, whose appearance is similar to the Arrhenius model, was developed by generalizing and extending the previous work of Gibbs and Dimarzio who applied the configurational entropy theory to explain the relaxational properties of glass-forming liquids [32, 41]. Adam and Gibbs stated that viscous flow of a liquid system occurs by the cooperative rearrangements of the varying species (atoms, ions, and molecules) in the liquid. The average probability for the structural rearrangements was derived by Adam and Gibbs and is given by

$$P(T) = A_p \cdot \exp\left(\frac{-B_p}{T \cdot S_c(T)}\right) \quad (2.6)$$

where: $P(T)$ is the average probability for the structural rearrangement; A_p and B_p are composition-dependent constants; T is the absolute temperature in K; $S_c(T)$ is the configurational entropy.

On the other hand, the average probability is inversely proportional to the structural relaxation time, which can be thought to be controlled by the probability of configurational variations in microscopic volumes. In the 1980s, Richet and his coworkers investigated the viscosity of silicate melts, and proposed that the structural relaxation time could be employed to indicate the shear strain relaxation time [33, 42]. Thus, a general Adam-Gibbs viscosity model was achieved and is given by

$$\log \eta = A + \frac{B}{T \cdot S_c(T)} \quad (2.7)$$

where: A and B are composition dependent constants. The configurational entropy $S_c(T)$ represents a measure of the dynamical states allowed to rearrange to new configurations [42], which can be calculated with

$$S_c(T) = S_c(T_{\text{ref}}) + \int_{T_{\text{ref}}}^T \frac{\Delta C_p}{T} dt \quad (2.8)$$

where: T_{ref} is a reference temperature and ΔC_p is the configurational heat capacity, which is given by [33]

$$\Delta C_p = C_{p,\text{liq}} - C_{p,\text{glass}} \quad (2.9)$$

where: $C_{p,\text{liq}}$ and $C_{p,\text{glass}}$ are the heat capacity in liquid and glassy phase states, respectively.

This viscosity model could give a basis for a semi-theoretical model which is used to calculate the viscosity of molten silicates [32]. The temperature dependence of viscosity is well described in the range from 1 Pa•s to 10^{12} .

Eyring model

On the basis of the absolute reaction rate theory [31], this model was derived by Eyring in 1941. He linked the absolute reaction rate theory with the viscosity in the molecular scale. A chemical reaction does not occur until the participating atoms or molecules come together to form the activated complex. That means that energy barriers must be overcome before the chemical reaction occurs. To describe the distribution of energy, the Maxwell-Boltzmann equation was employed.

Besides the activation energy, the chemical reaction always involves a change in the equilibrium distance between atoms or molecules. In the view of molecular scale, viscous flow can also be described as relative movements of two layers of molecules in the liquids. According to the same principles, the Eyring model revealing temperature dependence of viscosity is given by [43]

$$\eta = \frac{hN}{V_m} \cdot \exp\left(\frac{\Delta G^*}{RT}\right) = \frac{hN\rho}{M} \cdot \exp\left(\frac{\Delta G^*}{RT}\right) \quad (2.10)$$

where: h is the Planck's constant; N is the Avogadro's number; V_m is the molar volume; ΔG^* is the Gibbs energy of activation of viscous flow; R is the gas constant; T is the absolute temperature; ρ is the density and M is the molecular weight. The Eyring model can be transformed into an Arrhenius-like model, but they are theoretically different.

Weymann-Frenkel model

This model was developed in 1962, based on the hole theory [44, 45], and the liquid was assumed to be a quasi-crystalline structure. As the hole theory says, the properties of a liquid are determined by the motion of the holes just as the motion of molecules determines the properties of a gas. For the liquid matter in this model, the molecule can move from one equilibrium position to the next equilibrium position which is empty when it has adequate energy to overcome the potential barriers. On the basis of this liquid structure, the mechanical and statistical concepts were employed by Weymann to deduce the mechanism of viscosity, which is given by [11]

$$\eta = \left(\frac{RT}{E_W}\right)^{\frac{1}{2}} \cdot \frac{(2mkT)^{\frac{1}{2}}}{v^{\frac{2}{3}} \cdot P_V} \cdot \exp\left(\frac{E_W}{kT}\right) \quad (2.11)$$

where: R is the gas constant; T is the absolute temperature; E_W is the energy well; m and v are the mass and volume of the structural unit; k is the Boltzmann constant; P_V is the 'hole' probability connected with the structural model of the liquid. It should be pointed out that Eq. (2.11) is invalid without the following assumptions [11]. The direction of the shear stress is constrained to be in the gliding plane. Only the linear model, in which essentially one row of molecules moves through the potential field of a second row of molecules, is investigated. The transition probability is dependent on the number and the arrangement of the holes which are described by the S-distribution in a liquid in shear motion and the R-distribution in a liquid at rest.

The Weymann-Frenkel model can be simplified in the form of the following equation.

$$\log \eta = \log A + \log T + \frac{B}{T} \quad (2.12)$$

Compared to the Arrhenius model, an extra absolute temperature term is introduced. It is suitable to present the temperature dependence of silicate melt viscosities. Furthermore, in the case of high-temperature viscosity measurements for standard reference materials, Mills found that the Weymann-Frenkel model gives the best fit for the temperature dependence of most glasses and slags [46].

Bockris-Reddy model

This viscosity model based on the hole theory was deduced by Bockris and Reddy [47]. In this model, a fluid in motion is assumed to be moving layers of fluid in the direction parallel to liquid layers. According to the hole theory, the viscous forces are thought to occur due to the momentum transfer between moving fluid layers when holes jump from one layer to another, as shown in **Fig. 2.12**.

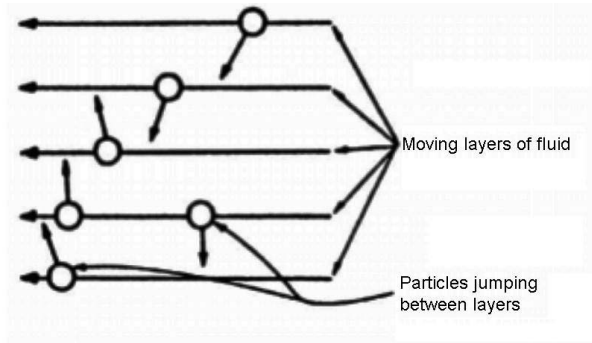


Fig. 2.12. Viscous forces are proposed to arise from momentum transfer between moving fluid layers when particles jump from one layer to another [47]

The viscous drag also arises during the similar momentum transfer. Thus, the Bockris-Reddy model is given by

$$\eta = \frac{2}{3} n_h \langle r_h \rangle \cdot (2\pi m k T)^{\frac{1}{2}} \cdot \exp\left(\frac{E}{RT}\right) \quad (2.13)$$

where: n_h is the number of holes per unit volume; $\langle r_h \rangle$ is the average radius of the holes; m is the mass of the ionic unit; k is the Boltzmann constant; T is the absolute temperature; E is the energy of ionic unit for viscous flow; R is the gas constant. This model has been applied to multicomponent slags.

AM model

In 1983, Milchev and Avramov [48] found that the dispersion around the mean energy barrier for diffusion in amorphous media can lead to a considerable change in the coefficient of atomic diffusion, which was inspired by the previous investigation of activated complex theory in bulk viscosity of liquids [49]. Followed by the study of influence of disorder on viscosity in condensed systems [50] as well as undercooled melts [51], the AM model was developed by relating the viscosity to the thermally activated jumping process. The viscosity was assumed to be inversely proportional to the average jump frequency of the building units of the system, where the specific jump does not occur until the corresponding activation energy is overcome.

The probability of appearance of energy barrier is introduced to calculate the average jump frequency, which is expressed as follows.

$$\langle \nu \rangle = \sum_{i=0}^{\infty} \nu_i \cdot p_i(E_i) \quad (2.14)$$

where: $\langle \nu \rangle$ is the average jump frequency; ν_i is the molecule jump frequency; $p_i(E_i)$ is the probability distribution function (Poisson probability distribution used here). The solution for Eq. (2.14) was obtained by employing the dispersity of the activation energy and the activation energy value at the maximum of probability. Then, Avramov and Milchev linked the dispersity to the entropy. Thus, the viscosity model was derived.

$$\eta = \eta_{\infty} \exp \left(\frac{\theta}{T} \right)^{\alpha} \quad (2.15)$$

where: η_{∞} is the constant; T is the absolute temperature; θ is a parameter in Kelvin; α is dimensionless parameter.

Summary

As mentioned above, the mechanism of viscosity in the molecular scale has been discussed and thereby the models concerning the temperature dependence of viscosity has been derived. These models are mainly applied in simple liquids. They could not give a good performance for more complicated liquids such as aluminosilicate melts. Nevertheless, the extensive studies on relationship between viscosity and temperature provide a reasonable framework for the further development of viscosity models of multicomponent systems.

2.3.1.2 Composition- and temperature-related models

Only considering the temperature dependence of viscosity is apparently not adequate due to the fact that viscosity is also a composition dependent variable. Over the past decades, a number of composition- and temperature-related models, such as the Shaw model, the Lakatos model, the Urbain model, the Iida model, the KTH model, and the

Avramov model have been developed so far. According to the treatment of composition of slag, these models are classified into two types, i.e. non-structure based models and structure based models. To avoid redundancy, the temperature dependence of viscosity will just be briefly referred to in the description of the following models.

2.3.1.2.1 Non-structure based models

The models of this kind only consider the influence of the bulk composition rather than the influence of the composition-related structure on the viscosity, and therefore they are treated as non-structure based models, such as the Shaw model, the Lakatos model, the Urbain model, the Riboud model, the Kalmanovitch-Frank model, the Hurst model, and the Kondratiev-Jak model. The introduction of the bulk composition probably increases the level of performance of viscosity models. A brief review is performed as follows.

Shaw model

Based on the Arrhenius-type temperature dependence of viscosity, an empirical model to calculate the viscosity was put forward by Shaw in 1972 [52]. He reviewed the Arrhenius mixture rule used by Bottinga and Weill [53], with which the viscosity of a Newtonian fluid can be described as the sum of each contribution η_i , based on the assumption that the silicate melts consist of varying liquid oxides.

$$\ln \eta(T) = \sum_i X_i \cdot \ln \eta_i = \sum_i X_i \cdot \left(A_i + \frac{B_i}{T} \right) \quad (2.16)$$

where: X_i is the mole fraction of oxide component i ; A_i and B_i are experimental constants of oxide component i .

However, this equation is largely insufficient to describe the viscosity over the entire range of compositions. Then, Shaw turned to investigate additivity relations for the constants A and B in the Arrhenius equation. He attempted to fit the viscosity data for rock compositions by methods of multiple regression analysis. It was found that it is much easier to estimate viscosities of multicomponent anhydrous silicate liquids without

the use of extensive tables in the model of Bottinga and Weill [53]. To develop the Shaw model, an assumption was introduced that the viscosity curve of multicomponent silicate liquids intersects the reference curve of a pure silica melt in an invariant point. Based on this assumption, the viscosity is given by

$$\log \eta = \alpha \cdot \frac{10^4}{T} - c_T \cdot \alpha + c_\eta \quad (2.17)$$

where: α is the characteristic slope; T is the absolute temperature; c_T and c_η are the coordinates of the invariable point. The characteristic slope is expressed as Eq. (2.18).

$$\alpha = \frac{X_{\text{SiO}_2} \cdot \sum(X_i \cdot \alpha_i^0)}{1 - X_{\text{SiO}_2}} \quad (2.18)$$

where: X_{SiO_2} is the mole fraction of SiO_2 ; X_i is the mole fraction of other components; α_i^0 is a constant.

In terms of performance of this model, Shaw stated that large negative deviation may occur when reproducing experimental data at viscosities above approximately $10^7 \text{ Pa}\cdot\text{s}$. Another shortcoming is that the predictions inevitably fail for melts which are exposed to any thermal or compositional gradients.

Lakatos model

By using the Vogel-Fulcher-Tammann type temperature dependence of viscosity, the Lakatos model [12] was developed by incorporating the influence of composition on viscosity into the three constants A , B , and C of the Vogel-Fulcher-Tammann model. To develop this model, the viscosity-temperature relations were built up for 30 different compositions in the system $\text{SiO}_2\text{--Al}_2\text{O}_3\text{--Na}_2\text{O--K}_2\text{O--CaO--MgO}$. The composition range is shown in **Table 2.3**. The Lakatos model was optimized by minimization of temperature deviations, and is given by

$$\log \eta = A + \frac{B}{T - C} \quad (2.19)$$

where: A, B, and C are composition-dependent constants, which are calculated from the following relations.

$$A = 1.5183 X_{\text{Al}_2\text{O}_3} - 1.6030 X_{\text{CaO}} - 5.4936 X_{\text{MgO}} + 1.4788 X_{\text{Na}_2\text{O}} - 0.8350 X_{\text{K}_2\text{O}} - 2.4550$$

$$B = 2253.4 X_{\text{Al}_2\text{O}_3} - 3919.3 X_{\text{CaO}} + 6285.3 X_{\text{MgO}} - 6039.7 X_{\text{Na}_2\text{O}} - 1439.6 X_{\text{K}_2\text{O}} + 5736.4$$

$$C = 294.4 X_{\text{Al}_2\text{O}_3} + 544.3 X_{\text{CaO}} - 384.0 X_{\text{MgO}} - 25.07 X_{\text{Na}_2\text{O}} - 321.0 X_{\text{K}_2\text{O}} + 471.3$$

It was found that the viscosity can be calculated by this model with good accuracy (standard deviation $\sim 3.0^\circ\text{C}$) if compositions are calculated on a molecular basis. The influences of constituents on viscosity are linearly dependent on the molecular contents and additives. The interaction between the constituents could be ignored. Although this model involves large deviations at high temperature, it is often used due to its simplicity.

Table 2.3. The composition range used for the development of the Lakatos model

Components	Mole fraction range
SiO ₂	0.61–0.77
Al ₂ O ₃	0.00–0.05
CaO	0.09–0.14
MgO	0.00–0.10
Na ₂ O	0.10–0.15
K ₂ O	0.00–0.06

Urbain model

By employing the Weymann-Frenkel model to describe the temperature dependence of viscosity, a model for calculating the viscosity of silicate and aluminosilicate melts was put forward by Urbain et al. in 1981 [54], in the form of a simplified Weymann-Frenkel model.

$$\eta = A \cdot T \cdot \exp\left(\frac{1000 \cdot B}{T}\right) \quad (2.20)$$

where: T is the absolute temperature; A and B are composition-dependent constants. Compared to the original Weymann-Frenkel model, constants A and B are obtained as follows.

$$A = \left(\frac{R}{E_W} \right)^{\frac{1}{2}} \cdot \frac{(2mk)^{\frac{1}{2}}}{\left(\frac{1}{V} \right)^{\frac{2}{3}} \cdot P_V} \quad (2.21)$$

$$B = \frac{E_W}{1000 \cdot k} \quad (2.22)$$

After further derivation, the relationship between A and B is given by

$$\ln A = -(m \cdot B + n) \quad (2.23)$$

where: m and n are model parameters, optimized based on the study of about 60 different compositions in the ternary systems $\text{SiO}_2\text{--Al}_2\text{O}_3\text{--MO}$ and $\text{SiO}_2\text{--Al}_2\text{O}_3\text{--R}_2\text{O}$, where MO and R_2O represent the bi- and mono-valent oxides, respectively. Urbain found that the m and n values are close to each other for similar liquids, although each liquid has a specific m and n value [20]. For ionic liquids, such as oxides, silicates, and aluminosilicates, the average values for parameters m and n are 0.293 and 11.571, respectively, whereas m and n are 0.207 and 10.288, respectively, for network liquids such as B_2O_3 , GeO_2 , and SiO_2 .

The composition-dependent constant B is determined by introduction of parameter α . To calculate α , the constituents are classified into the following three categories, according to their oxygen content.

- Glass formers: SiO_2 , P_2O_5 , etc.
- Network modifiers: CaO , MgO , FeO , Na_2O , K_2O , etc.
- Amphoteric: Al_2O_3 , Fe_2O_3 , etc.

$$\alpha = \frac{\text{Mole fraction of Network modifiers}}{\text{Mole fraction of Network modifiers} + \text{Mole fraction of Amphoteric}} \quad (2.24)$$

Then, the parameter B is linked with the composition, which can be expressed as a polynomial equation.

$$B = B_0 + B_1 \cdot X_{\text{SiO}_2} + B_2 \cdot X_{\text{SiO}_2}^2 + B_3 \cdot X_{\text{SiO}_2}^3 \quad (2.25)$$

$$B_i = a_i + b_i \cdot \alpha - c_i \cdot \alpha^2 \quad (2.26)$$

$i=0, 1, 2$, and 3 .

where: a_i , b_i , and c_i are fitting parameters; X_{SiO_2} is the mole fraction of silica. For the $\text{SiO}_2\text{--Al}_2\text{O}_3\text{--CaO}$ system, four polynomial equations are used to calculate the parameter B.

$$B_0 = 13.8 + 39.9355 \cdot \alpha - 44.049 \cdot \alpha^2$$

$$B_1 = 30.481 - 117.1505 \cdot \alpha + 129.9978 \cdot \alpha^2 \quad (2.27)$$

$$B_2 = -40.9429 + 234.0486 \cdot \alpha - 300.04 \cdot \alpha^2$$

$$B_3 = 60.7619 - 153.9276 \cdot \alpha + 211.1616 \cdot \alpha^2$$

Then, the parameter A can be easily obtained from B. By applying the Urbain model to multicomponent mixtures, Mills and Broadbent [55] reported that the composition dependence of viscosity can be properly described. However, Kondratiev and Jak [56] found that it is not capable of describing viscosity over the entire compositional range of the studied slag systems in 2001.

Riboud model

Riboud et al. modified the composition-dependent constants A and B in the Urbain model, to describe the viscosities of the system $\text{CaO--Al}_2\text{O}_3\text{--SiO}_2\text{--CaF}_2$ [14]. This modified Urbain model is called the Riboud model, in which the slag components are classified into five different categories as follows.

- 'SiO₂' group: SiO₂, P₂O₅, etc.
- 'CaO' group: CaO, MgO, FeO, etc.

- 'Al₂O₃' group: Al₂O₃, etc.
- 'CaF₂' group: CaF₂
- 'Na₂O' group: Na₂O, K₂O, etc.

Then, the compositional relationship of the Urbain model was modified into the following expression.

$$\ln A = -35.76 X_{\text{Al}_2\text{O}_3} + 1.73 X_{\text{CaO}} + 7.02 X_{\text{Na}_2\text{O}} + 5.82 X_{\text{CaF}_2} - 19.81 \quad (2.28)$$

$$B = 68.833 X_{\text{Al}_2\text{O}_3} - 23.896 X_{\text{CaO}} - 39.159 X_{\text{Na}_2\text{O}} - 46.356 X_{\text{CaF}_2} + 31.140 \quad (2.29)$$

where: A and B are the composition-dependent constants; X_i is the mole fraction of each group.

This model was originally developed for continuous casting mould fluxes, while it was later found that it could be applied to other metallurgical slags, especially for the compositional range listed in **Table 2.4**.

Table 2.4. The composition range suitable for the Riboud model

Components	Mass fraction range
SiO ₂	0.27–0.56
Al ₂ O ₃	0.00–0.12
CaO	0.08–0.46
Na ₂ O	0.00–0.22
CaF ₂	0.00–0.18

Kalmanovitch-Frank model

In 1988, Kalmanovitch and Frank [57] employed the Urbain model to calculate the viscosities of particular coal ash slags, then modified the relationship between constants A and B according to the following equation.

$$\ln A = -(0.2812 \cdot B + 14.1305) \quad (2.30)$$

Srinivasachar et al. reported that the Kalmanovitch-Frank model cannot give a good performance in describing the viscosity (above 10^3 Pa·s) at low temperatures [58]. A poor performance in describing the viscosity of FeO-containing systems is revealed by Jak et al. [59]. Nevertheless, Vargas et al. reported that the model can describe the viscosities of some special coal ash slags, such as British coal ash slags, Illinois No. 6 coal ashes, and Pittsburgh No. 8 coal ashes [57].

Hurst model

The Urbain model was modified by Hurst et al. to describe the viscosity of the coal ash slag system $\text{SiO}_2\text{--Al}_2\text{O}_3\text{--CaO--FeO}$, based on a least squares fit of the experimental data to the transformed Weymann-Frenkel model [60].

$$\eta = A \cdot T \cdot \exp\left(\frac{B}{R \cdot T}\right) \quad (2.31)$$

$$\ln \eta = \ln A + \ln T + \frac{B}{R \cdot T} \quad (2.32)$$

$$\begin{aligned} \ln \eta = & a_0 + a_1y + a_2y^2 + a_3x + a_4xy + a_5xy^2 + a_6x^2 \\ & + a_7x^2y + a_8x^2y^2 + a_9x^3 + a_{10}x^3y + a_{11}x^3y^2 \end{aligned} \quad (2.33)$$

where: T is the absolute temperature; R is the gas constant; A and B are composition-dependent constants; x and y are the normalized mole fractions $m_s/(m_s + m_a + m_c + m_f)$ and $(m_c + m_f)/(m_a + m_c + m_f)$, respectively. Here, the subscripts s , a , c , and f correspond to SiO_2 , Al_2O_3 , CaO , and FeO , respectively.

It was found that a better performance is given over a smaller range of compositions, compared to the Urbain model that is applied to the whole range of compositions. In 1999 the model was applied to the coal ash slags containing 5 wt.% and 10 wt.% FeO [61], and was further extended to the slags containing 15 wt.% FeO in 2000 [62]. However, different sets of model parameters are required for different ranges of FeO contents. As described by Ilyushechkin and Hla, a new set of model parameters is required when the Hurst model is applied to describe the viscosity of coal ash slags

containing 16.5–21 wt.% FeO [63]. Moreover, the viscosity model used by Ilyushechkin and Hla is applicable only for temperatures from 1450°C to 1550°C.

Kondratiev-Jak model

Based on the Urbain model, a model for predicting viscosities of the fully liquid system $\text{Al}_2\text{O}_3\text{--CaO--'FeO'--SiO}_2$ was developed by Kondratiev and Jak in 2001 [56], with two modifications as follows. The first is to introduce the composition-dependent parameter m instead of a constant optimized value.

$$m = \sum m_i \cdot X_i \quad (2.34)$$

where: m_i and X_i are the model parameter for a pure oxide and the mole fraction of the corresponding oxide, respectively.

Another modification is to introduce the continuous composition-dependent parameter B for two different network modifiers, i.e. FeO and CaO, in place of an average B simply calculated from each modifier.

$$B = \sum_{i=0}^3 b_i^0 \cdot X_s^i + \sum_{i=0}^3 \sum_{j=1}^2 (b_i^{C,j} \cdot \frac{X_c}{X_c + X_F} + b_i^{F,j} \cdot \frac{X_F}{X_c + X_F}) \cdot \alpha^j \cdot X_s^i \quad (2.35)$$

$$\alpha = \frac{X_c + X_F}{X_c + X_F + X_A} \quad (2.36)$$

where: X_A , X_c , X_F , and X_s are the mole fractions of Al_2O_3 , CaO , FeO , and SiO_2 , respectively; b_i^0 is the parameter for the system $\text{SiO}_2\text{--Al}_2\text{O}_3$; $b_i^{C,j}$ and $b_i^{F,j}$ are the sets of parameters for CaO and 'FeO', respectively.

It was found that a good agreement between calculated viscosities and experimental results is achieved for the quaternary system $\text{Al}_2\text{O}_3\text{--CaO--'FeO'--SiO}_2$. However, it still cannot describe the Al_2O_3 -induced varying viscosity maxima due to the lack of an effective description about the structural dependence of the viscosity. When the Kondratiev-Jak model is employed to calculate the viscosity of the liquid phase for the

viscosity model that predicts viscosities of partly crystallized slags [64], it might cause a great deviation.

Summary

The models mentioned in this section belong to semi-empirical models, which lack sufficient consideration of liquid structure. Most of them are only capable in their own compositional range and normally need more than one set of model parameters.

2.3.1.2.2 Structure based models

This kind of models have related the structures of slags rather than simple bulk compositions to the viscosity, which are, therefore, defined as structure based models, such as the Zhang-Jahanshahi model, the Reddy model, the Iida model, the KTH model, the Avramov model, the Quasi-chemical viscosity model, and the FactSage model. The consideration of internal structure makes the viscosity models show a better performance over a wide range of compositions and temperatures. The models of this style will be reviewed in this section, briefly.

Zhang-Jahanshahi model

Based on the Weymann-Frenkel type temperature dependence of viscosity, the Zhang-Jahanshahi model [65, 66] was developed by linking three types of oxygen, i.e. bridging, non-bridging, and free oxygen, to the composition dependence of viscosity, which is shown as a simplified Weymann-Frenkel model.

$$\eta = A^w \cdot T \cdot \exp\left(\frac{E_{\eta}^w}{R \cdot T}\right) \quad (2.37)$$

where: A^w is the pre-exponential parameter; E_{η}^w is the activation energy.

It is well known that the viscosity and activation energy increase with increasing silica content in silicate melts, which is thought to be the outcome of the network structure development. Such structural change can be indicated by the degree of polymerization. Zhang and Jahanshahi introduced three types of oxygen as mentioned above to reveal

the degree of polymerization. The concentration of oxygen can be obtained by experiments, such as molar refractivity, infrared, and Raman spectroscopy, or calculated by molecular dynamic simulations of silicate melts. Due to the fact that both experimental data and simulation results were limited at that time, the cell model, which was put forward by Kapoor and Froberg for binary and ternary silicate melts, was employed to calculate the concentrations of three types of oxygen. By using them, the activation energy of the simplified Weymann model is given by

$$E_{\eta}^w = a + b \cdot (N_{O^0})^3 + c \cdot (N_{O^0})^2 + d \cdot (N_{O^{2-}}) \quad (2.38)$$

where: a , b , c , and d are fitting parameters; N_{O^0} and $N_{O^{2-}}$ are mole fractions of bridging and free oxygen, respectively. The pre-exponential parameter can be obtained by Eq. (2.39).

$$\ln A^w = a' + b' \cdot E_{\eta}^w \quad (2.39)$$

where: a' and b' are unique coefficients for a particular system. Although fitting parameters were optimized by the experimental data of binary silicates, it was demonstrated that this model can provide a good description of the viscosity in higher order slag systems with respect to both the change in silica content and the effect of different cations on viscosity. However, the values of the viscosity extrapolated from SiO_2 -based binary systems to pure SiO_2 differ.

Reddy model

The Reddy model [67] was developed to estimate the viscosity of the ternary system $\text{Na}_2\text{O}-\text{SiO}_2-\text{B}_2\text{O}_3$, by employing the Bockris-Reddy type temperature behavior, which is given by

$$\eta = 1.68 \times 10^{-9} (X_{\text{B}_2\text{O}_3} + 0.77 X_{\text{SiO}_2}) \cdot (X_{\text{B}_2\text{O}_3} + 1.04 X_{\text{SiO}_2})^{\frac{1}{2}} \cdot (3 X_{\text{B}_2\text{O}_3} + 2 X_{\text{SiO}_2})^{-\frac{3}{2}} \cdot (N_{O^0}) \cdot T^{\frac{1}{2}} \cdot \exp\left(\frac{E}{RT}\right) \quad (2.40)$$

where: $X_{B_2O_3}$ and X_{SiO_2} are equivalent mole fractions; N_{O^0} is the mole fraction of bridging oxygen; T is the absolute temperature; E is the energy allowing to break the bond of the ionic unit; R is the gas constant. In this model, SiO_2 and B_2O_3 are characterized as network formers while Na_2O is considered as a network modifier. Thus, the mole fraction of bridging oxygen in the melt based on the atomic pair model is obtained by the following equation.

$$N_{O^0} = \frac{3X_{B_2O_3} + 2X_{SiO_2} - \frac{1}{2}N_{O^-}}{2X_{B_2O_3} + X_{SiO_2} + 1} \quad (2.41)$$

where: N_{O^-} is the mole fraction of non-bridging oxygen. And another term E can be given by:

$$E = A + B \cdot T$$

$$A = k + m \cdot X_{B_2O_3} + n \cdot X_{B_2O_3}^2 + p \cdot X_{B_2O_3}^3 \quad (2.42)$$

$$B = \alpha + \beta \cdot X_{B_2O_3} + \gamma \cdot X_{B_2O_3}^2 + \delta \cdot X_{B_2O_3}^3$$

where: all parameters mentioned in Eq. (2.42) can be expressed by polynomial equation.

$$k = -4.10909 \times 10^5 - 3.16176 \times 10^5 R + 1.216120 \times 10^6 R^2 - 5.13104 \times 10^5 R^3$$

$$m = -1.343160 \times 10^6 + 1.7586 \times 10^7 R - 2.2046 \times 10^7 R^2 + 1.768940 \times 10^6 R^3$$

$$n = 1.59975 \times 10^7 - 8.4629 \times 10^7 R + 9.18343 \times 10^7 R^2 - 2.76946 \times 10^6 R^3$$

$$p = -2.15337 \times 10^7 + 9.79282 \times 10^7 R - 1.01984 \times 10^7 R^2 + 2.99583 \times 10^6 R^3$$

$$\alpha = 1557.73 - 2146.51 R + 684.746 R^2 + 66.530 R^3 \quad (2.43)$$

$$\beta = -8493.96 + 8023.87 R + 1457.36 R^2 - 297.47 R^3$$

$$\gamma = 13734.2 + 2565.39 R - 22661.9 R^2 + 9981.06 R^3$$

$$\delta = -7326.2 - 14018.2 R + 28442.3 R^2 + 10587.9 R^3$$

where: R is the ratio of $X_{\text{SiO}_2}/X_{\text{Na}_2\text{O}}$.

It was found that the correlation of parameters η_h and $\langle r_h \rangle$ in the Bockris-Reddy model to composition is dependent on the definition of the structure units. Moreover, the performance of this model is satisfactory only for a limited range of compositions. In 2004, Zhang and Reddy [68] used the Reddy model to predict the viscosity of the same system $\text{Na}_2\text{O}-\text{SiO}_2-\text{B}_2\text{O}_3$ containing a higher content of SiO_2 (ratio $R=5$), where the polynomial equation for the term E is completely changed.

lida model

The basicity index was introduced in the lida model [69], by which the network structure is linked to viscosity. The lida model is expressed in a similar form of the Arrhenius model.

$$\eta = A \cdot \eta_0 \cdot \exp\left(\frac{E}{B_i^*}\right) \quad (2.44)$$

where: A and E are fitting parameters; η_0 is the hypothetical viscosity of non-network forming melts; B_i^* is the modified basicity index. All the parameters are further expressed by

$$A = 1.745 - 1.962 \times 10^{-3}T + 7.000 \times 10^{-7}T^2$$

$$E = 11.11 - 3.65 \times 10^{-3}T$$

$$\eta_0 = \sum \eta_{oi} \cdot X_i \quad (2.45)$$

$$\eta_{oi} = 1.8 \times 10^{-7} \frac{[M_i(T_m)_i]^{1/2} \exp(H_i/RT)}{(V_m)_i^{2/3} \exp[H_i/R(T_m)_i]}$$

$$H_i = 5.1(T_m)_i^{1/2}$$

$$B_i^* = \frac{\sum(\alpha_i W_i)_B + \alpha_{\text{Fe}_2\text{O}_3}^* W_{\text{Fe}_2\text{O}_3}}{\sum(\alpha_i W_i)_A + \alpha_{\text{Al}_2\text{O}_3}^* W_{\text{Al}_2\text{O}_3} + \alpha_{\text{TiO}_2}^* W_{\text{TiO}_2}}$$

where: η_{0i} is the hypothetical viscosity of the pure component; X_i is the mole fraction of each component; M_i is the formula weight of each component; $(T_m)_i$ is the melting point of each component; H_i is the coefficient of each component; $(V_m)_i$ is the molar volume at the corresponding melting point of each component; α_i and W_i are the specific coefficient and the mass percentage of each component, respectively; the subscripts A and B represent acidic oxide and basic oxide or fluoride, respectively; α_i^* is the modified specific coefficient indicating the interaction of the amphoteric oxide with other components.

The temperature-dependent parameters A and E were obtained by fitting the experimental data. The α_i^* could be obtained by correlating linearly to the basicity index B_i and the mass percentage of the amphoteric oxides W_i due to the fact that the amphoteric effect varies with the change in overall basicity of the slag. The other parameters mentioned above can be found or simply calculated from handbooks of physical properties. This model needs many fitting parameters to describe the amphoteric effect of Al_2O_3 , and these fitting parameters might be applicable in a limited range of compositions and temperatures, which was revealed by Forsbacka and Holappa when applying the Iida model to describe the viscosity of SiO_2 – CaO – CrO_x slags [70].

KTH model

Based on the Eyring model, the KTH model [71, 72] to estimate viscosities for ionic melts was developed by linking the Gibbs energy of activation of viscous flow to the composition dependence of the viscosity, as shown in the simplified Eyring model.

$$\eta = A \cdot \exp\left(\frac{\Delta G^*}{R \cdot T}\right) \quad (2.46)$$

where: A is the pre-exponential term; ΔG^* is the Gibbs energy of activation of viscous flow; R is the gas constant; T is the absolute temperature. The pre-exponential term A can be calculated with

$$A = \frac{hN\rho}{M} \quad (2.47)$$

where: h is Planck's constant; N is Avagadro's number; ρ is the density of the melt; M is the molecular weight.

For unary systems, the pre-exponent term A can be directly calculated from the molecular weight and the density of the pure liquid. The Gibbs energy of activation of viscous flow is obtained by

$$\Delta G^* = a + b \cdot T + c \cdot T \cdot \ln T + \dots \quad (2.48)$$

where: a , b , and c are the parameters optimized from experimental data. In addition, it is enough to consider the first two or three terms of Eq. (2.48) for good prediction of viscosity of pure oxide.

In the case of multicomponent systems, the molecular weight and density are calculated with the following equations.

$$M = \sum X_{ij} \cdot M_{ij}$$

$$\rho = \sum X_{ij} \cdot \rho_{ij} \quad (2.49)$$

where: X_{ij} is the mole fraction of the component $Ci_{vi}Aj_{vj}$; M_{ij} and ρ_{ij} represent the molecular weight and density of the component $Ci_{vi}Aj_{vj}$, respectively. Here, for the component $Ci_{vi}Aj_{vj}$, Ci and Aj represent the cation and anion, respectively, whereas the subscripts vi and vj are the stoichiometric coefficients. The Gibbs energy of activation in this case can be expressed by

$$\Delta G^* = \sum \sum X_{ij} \cdot \Delta G_{ij}^* + G^{ideal} + \Delta E_{G^*} \quad (2.50)$$

where: ΔG_{ij}^* is the Gibbs energy of activation of pure component $Ci_{vi}Aj_{vj}$ in liquid state, thus the term $\sum \sum X_{ij} \cdot \Delta G_{ij}^*$ stands for the linear summation of the Gibbs energy of

activation from the pure components without consideration of interaction between different components; the term G^{ideal} represents the change in Gibbs energy resulting from the ideal mixing of components; $\Delta^E G^*$ represents the change in Gibbs energy resulting from the mutual interactions between different species.

This model can give a good estimation of viscosities for various metallic as well as slag systems, from unary to quaternary systems. However, the structural dependence of viscosity cannot be completely described by linking the viscosity to the Gibbs energy. Seetharaman et al. stated that the KTH model cannot cover the entire slag area like other models such as the Iida model and the Reddy model [73].

Avramov model

Based on the non-Arrhenius type temperature dependence of viscosity (the AM model), Avramov introduced the Q^n -groups to reveal the dependence of effective activation energy on composition, and then to display the composition dependence of viscosity [74].

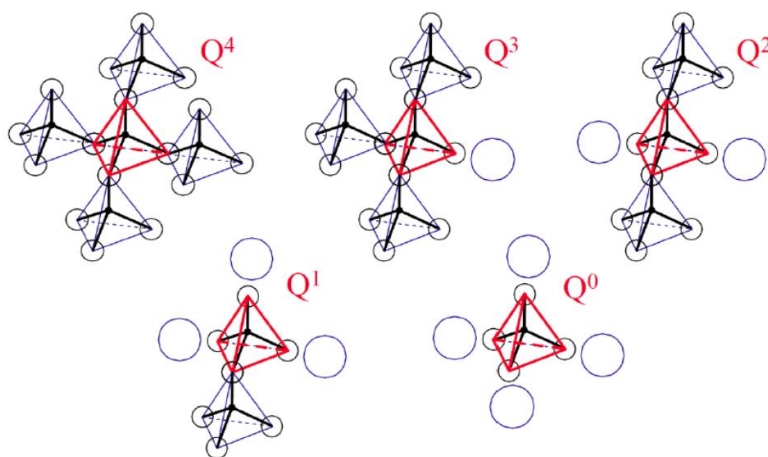


Fig. 2.13. Schematic diagram of Q^n -groups [75]

These Q^n -groups were developed from the modified random network structure, where the silica tetrahedra are connected by sharing oxygen ions. According to the

coordination number of Si in silicates, the components in silicate melts are classified as five different Q^n -groups: Q^0 , Q^1 , Q^2 , Q^3 , and Q^4 , which is illustrated in **Fig. 2.13**.

The activation energy for molecular motion E_n is strongly dependent on n . The distribution of Q^n -groups is assumed to be random at high temperature. Thus, the average jump frequency is modified by

$$\langle \nu \rangle = \nu_{\infty} \sum_{n=0}^4 Q^n \cdot \exp\left(-\frac{E_n}{R \cdot T}\right) \quad (2.51)$$

where: ν_{∞} is the variation frequency, ca. 10^{12} s^{-1} ; R is the gas constant; T is the absolute temperature; Q^n is the concentration of Si with n 'strong' oxygen bonds; E_n is the activation energy for molecular motion with n 'strong' oxygen bonds. By using the Maxwell relationship, the viscosity is obtained by

$$\eta = \frac{\eta_{\infty}}{\sum_{n=0}^4 Q^n \cdot \exp\left(-\frac{E_n}{R \cdot T}\right)} \quad (2.52)$$

where: η_{∞} is the pre-exponential constant. This model can describe the so called 'lubricant effect' that the viscosity sharply falls due to the presence of a low concentration of modifying oxides. However, the amphoteric or charge compensation effect induced by Al_2O_3 cannot be described.

Quasi-chemical viscosity model

The fundamental theory of this model is Frenkel's kinetic theory of liquids. According to this theory, the shear force in viscous flow, which is caused by the movement of structural units, can be determined by both the ability of structural units to jump over the potential barrier and the concentration of 'holes' in the liquid. Based on the assumption of liquid state and liquid viscosity put forward by Frenkel, the Quasi-chemical viscosity model is given by [76]

$$\eta = \frac{2RT}{\Delta E_{\text{vap}}} \cdot \frac{(2\pi m_{\text{SU}} kT)^{\frac{1}{2}}}{v_{\text{SU}}^{\frac{2}{3}}} \cdot \exp\left(\frac{E_a}{RT}\right) \quad (2.53)$$

where: ΔE_{vap} is the energy of vaporization; E_a is the activation energy; m_{SU} and v_{SU} are the weight and volume of a structure unit of viscous flow, respectively. These four parameters are influenced by the definition of the structural unit. Therefore, it is important to properly define the structural unit of the viscous flow in the Quasi-chemical viscosity model. The concept of the structure of silicate slag put forward by Fincham and Richardson was introduced in this model. There are three types of oxygen, i.e. bridging, non-bridging, and free oxygen, in silicate slags. Following this concept, the structural units of viscous flow can be defined as their combination where oxygen anions partly associate with metal cations: $\text{Si}_{0.5}\text{O}$, $\text{Me}_{2/n}^{n+}\text{O}$, and $\text{Me}_{1/n}^{n+}\text{Si}_{0.5}\text{O}$, as illustrated in Fig. 2.14.

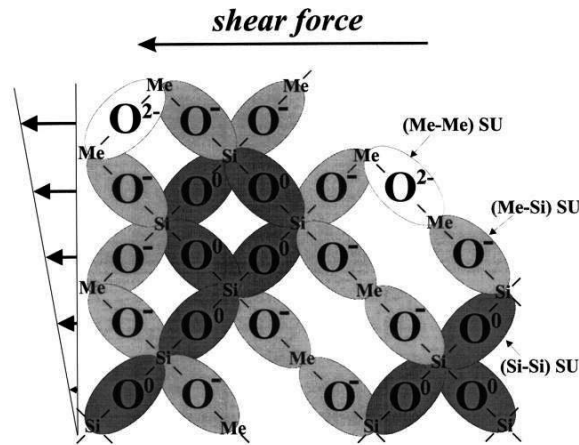


Fig. 2.14. Presentation of internal structure and viscous flow in silicates, where: O^0 , O^- , and O^{2-} are the bridging, non-bridging, and free oxygen, respectively [76]

Thus, for a binary system $\text{SiO}_2\text{--MeO}$ as an example, there are three different structural units Si--O--Si ($\text{Si}_{0.5}\text{O}$), Si--O--Me ($\text{Me}_{1/n}^{n+}\text{Si}_{0.5}\text{O}$), and Me--O--Me ($\text{Me}_{2/n}^{n+}\text{O}$), which can be abbreviated as the so called second nearest neighbor bonds Si-Si, Si-Me, and Me-Me, respectively. The four parameters of the Quasi-chemical viscosity model, thereby, can be given by

$$m_{\text{SU}} = m_{\text{Si-Si}}X_{\text{Si-Si}} + m_{\text{Me-Si}}X_{\text{Me-Si}} + m_{\text{Me-Me}}X_{\text{Me-Me}}$$

$$v_{\text{SU}} = v_{\text{Si-Si}} X_{\text{Si-Si}} + v_{\text{Me-Si}} X_{\text{Me-Si}} + v_{\text{Me-Me}} X_{\text{Me-Me}} \quad (2.54)$$

$$E_a = E_{a,\text{Si-Si}} X_{\text{Si-Si}} + E_{a,\text{Me-Si}} X_{\text{Me-Si}} + E_{a,\text{Me-Me}} X_{\text{Me-Me}} + \left(E_a^{\text{ch/c}} \right)$$

$$\Delta E_{\text{vap}} = \exp(E_{v,\text{Si-Si}} X_{\text{Si-Si}} + E_{v,\text{Me-Si}} X_{\text{Me-Si}} + E_{v,\text{Me-Me}} X_{\text{Me-Me}})$$

where: $X_{\text{Si-Si}}$, $X_{\text{Si-Me}}$, and $X_{\text{Me-Me}}$ are the mole fractions of the structural units; $m_{\text{Si-Si}}$, $m_{\text{Me-Si}}$, and $m_{\text{Me-Me}}$ are the weights of the structural units; $v_{\text{Si-Si}}$, $v_{\text{Si-Me}}$, and $v_{\text{Me-Me}}$ are the volumes of the structural units; $E_{a,\text{Si-Si}}$, $E_{a,\text{Me-Si}}$, and $E_{a,\text{Me-Me}}$ are the partial molar activation energies, and $\left(E_a^{\text{ch/c}} \right)$ represents the charge compensation effect; $E_{v,\text{Si-Si}}$, $E_{v,\text{Me-Si}}$, and $E_{v,\text{Me-Me}}$ are the dimensionless partial vaporization energy coefficients.

This model, in general, shows a good agreement between experimental data and calculated results for the fully liquid system $\text{Al}_2\text{O}_3\text{--CaO--FeO--MgO--SiO}_2$. But, it involves a large deviation at high silica content. Moreover, the amphoteric or charge compensation effect cannot be described with the second nearest neighbor bond concentrations, and some additional specific terms are needed to describe the Al_2O_3 -induced viscosity maximum, requiring many complicated model parameters.

FactSage model

By relying on the thermodynamic model and database put forward by Kondratiev and Jak, a viscosity model [77, 78] (a built-in module in FactSage software package and here is called the FactSage model) was developed by linking the concentration of Q^n species to the viscosity. In this model, the structure of silicate melts is characterized by the concept of Q^n species, where the concentration of Q^n species can be calculated by the concentration of bridging oxygen as mentioned in the Quasi-chemical viscosity model. As an example, the probability of the appearance of Q^4 species in silicate melts is given by

$$Y(Q^4) = p^4 \quad (2.55)$$

where: p is the probability to form bridging oxygen. In terms of polymerization of the silicate melts, it can be described by the degree of connectivity of the Q^n species. With increasing silica content, the silica tetrahedra polymerize to form dimers and trimers, even longer chains or rings. The probability of such a change in structure can be given by

$$Y(Q^{4,n})=p^n \quad (2.56)$$

where: the term $Y(Q^{4,n})$ represents the degree of connectivity of silica tetrahedra. Based on the Arrhenius type temperature dependence, a model is developed by the modification of the constants A and B in the Arrhenius model, taking binary systems $SiO_2 - MeO_x$ ($MeO_x = NaO_{0.5}, CaO, MgO, \dots$) as an example.

$$A = A_{MeO_x} X(MeO_x) + A_{SiO_2}^* X(SiO_2) + A_{SiO_2}^E X(SiO_2) p^{40} + A_{Me-Si} X(MeO_x) X(SiO_2) + A_{Me-Si}^R X(SiO_2) (p^4 - p^{40}) \quad (2.57)$$

$$E = E_{MeO_x} X(MeO_x) + E_{SiO_2}^* X(SiO_2) + E_{SiO_2}^E X(SiO_2) p^{40} + E_{Me-Si} X(MeO_x) X(SiO_2) + E_{Me-Si}^R X(SiO_2) (p^4 - p^{40}) \quad (2.58)$$

where: $X(SiO_2) p^{40}$ stands for the concentration of clusters of interconnected Si-Si pairs; $A_{SiO_2}^E$ and $E_{SiO_2}^E$ are parameters to describe the dramatic increase in viscosity when approaching pure SiO_2 ; the term $X(SiO_2) (p^4 - p^{40})$ represents the concentration of smaller clusters of interconnected Si-Si pairs; the cross-term $X(MeO_x) X(SiO_2)$, A_{Me-Si} , E_{Me-Si} , A_{Me-Si}^R , and E_{Me-Si}^R are parameters for describing the non-linear effect of composition on viscosity. The viscosity, therefore, is estimated with Eq. (2.4).

The model is capable of describing viscosities of the system $NaO_{0.5}-MgO-CaO-AlO_{1.5}-SiO_2$ and its subsystems. Besides the Q^n species, additional associates $NaAlO_2$, $CaAl_2O_4$, and $MgAl_2O_4$ are introduced to describe the Al_2O_3 -induced viscosity maximum. However, the Al_2O_3 -induced viscosity maximum for binary systems such as the system Al_2O_3-CaO is not presented. Moreover, a pronounced decrease in viscosity around 0.50 mole fraction SiO_2 is not well described for the binary systems SiO_2-Na_2O and SiO_2-

K₂O. In order to improve the performance in describing the viscosity of the binary systems containing alkali oxides, Kim et al. modified the model of Grundy et al. [77], in which an additional excess viscosity contribution resulted from the formation of large rings of Q²- and Q³-species is required for each alkali oxide-SiO₂ system [79].

Summary

The models of this style are mostly complicated and involve numerous model parameters, most of which are only mathematical fitting parameters and lack of clear physico-chemical meaning. The models are still not capable of describing the viscosity over the whole range of compositions and a wide range of temperatures. Moreover, some of the models are not self-consistent, such as the Zhang-Jahanshahi model.

2.3.2 Multiphase slag systems

It is common that slagging gasification is carried out in multiphase slag systems where coal particles are suspended in the molten slag or crystallizing particles present due to low temperature. The presence of solid phases causes a large deviation for the models developed for fully liquid phase. The deviation increases with increasing volume fraction of solid phases. Furthermore, viscous flow behavior will transform from Newtonian type to non-Newtonian type if the solid fraction is greater than 10%–40% depending on the shape and size of solid particles [80].

Constant and continuous efforts have been made to describe the viscous flow behavior of multiphase slag systems. A few examples like the Einstein model and the Roscoe model are presented here to give an acceptable mechanism of viscosities in solid-liquid systems.

Einstein model

Based on the Stokes equation, a linear model was derived by Einstein [81, 82] at the beginning of the twentieth century, where the viscosity of a solid-liquid mixture is linked to the volume fraction of solid particles.

$$\eta_e = \eta \cdot (1 + 2.5\theta) \quad (2.59)$$

where: η_e is the effective viscosity; η is the pure solvent viscosity; θ is the volume fraction of solid particles in the slag.

In terms of the performance of the Einstein model, it can describe the viscosity only in a mixture with very low fraction of solid particles (< 5 vol%). In 1911, it was found by Einstein that the factor 2.5 in the model is only valid for rigid spheres. In 1950 Ward and Whitmore [83] stated that the factor may vary between 1.9 and 4.0 according to the particle size distribution.

Roscoe model

On the basis of the Einstein model, the Roscoe model [84] was developed with a nonlinear relationship between the viscosity and volume fraction of solid particles, instead of the linear relationship in the Einstein model. In order to find out the dependence of viscosity on the size distribution of the solid particles, Roscoe derived the following expression through the study of viscosities of a suspension containing spheres with very diverse sizes.

$$\eta_e = \eta \cdot (1 - \theta)^{-2.5} \quad (2.60)$$

This equation can deal with solid particles with diverse size and is theoretically valid for all fractions of solid particles in the liquid.

In order to estimate the viscosity at high volume fractions of uniform solid particles in the slag, another experiment was conducted by Roscoe, where a suspension with high concentration of uniform spheres was employed. The corresponding relation was obtained according to the argument of Vand [85], which is given by

$$\eta_e = \eta \cdot (1 - 1.35\theta)^{-2.5} \quad (2.61)$$

This model is not strictly constraint to the aggregates with spherical shape in the liquid. These two similar models are later generalized as the Einstein-Roscoe model, which is given by

$$\eta_e = \eta \cdot (1 - R \cdot \theta)^{-n} \quad (2.62)$$

where: R and n are empirical parameters optimized by experimental data. This model was later examined by other authors. In the study of viscosities of partly crystallized slags in the $\text{Al}_2\text{O}_3\text{--CaO--FeO--SiO}_2$ system, Kondratiev and Jak stated that it is allowed to give a good fit for the multiphase slag system with a volume fraction of solid particles up to 30% by assuming the empirical factors $R = 2.04$ and $n = -1.29$ [64].

In 2011, the investigation by Wu et al. also demonstrated that the Einstein-Roscoe model can describe the effect of solid particles on viscosity in the case of both room temperature and high temperature [86]. It was also found that this model can be applied to solid particles with irregular shape without any modifications of the model parameters.

2.4 Methods of viscosity measurements

This section discusses the methods with which the viscosity of slag at high temperature is measured.

2.4.1 Rotating cylinder method

A rotating cylinder viscometer is the most widely used method to measure the viscosity of the slag at high temperature. Usually, an inner cylinder (or bob) is placed in an outer cup (or cylinder), as shown in **Fig. 2.15**. In this figure the inner cylinder is rotated whereas the outer cup is fixed, and the cup is filled with the sample of the slag. When the inner cylinder is rotated at a constant speed, the viscosity can be determined from the measurement of torque that is required to rotate the inner cylinder. When the gap between the inner cylinder and the outer cup is small enough, the absolute viscosity measurement is feasible and thereby the viscosity can be calculated with the following equation [87].

$$\eta = \frac{T}{4\pi L \omega} \left(\frac{1}{r_i^2} - \frac{1}{r_o^2} \right) \quad (2.63)$$

where: η is the viscosity ($\text{Pa}\cdot\text{s}$); T is the torque ($\text{N}\cdot\text{m}$); ω is the angular velocity (s^{-1}); L is the depth of penetration (m); r_i and r_o are the radii of the inner and outer cylinders (m), respectively. When the ratio of radii of the outer and inner cylinders is greater than 1.1, the absolute viscosity measurement is not feasible. However, for given experimental conditions, r_i , r_o , and L are known, the viscosity can be calculated with

$$\eta = C_0 \frac{T}{\omega} \quad (2.64)$$

where: C_0 is the equipment constant which can be obtained from calibration with liquids of known viscosity.

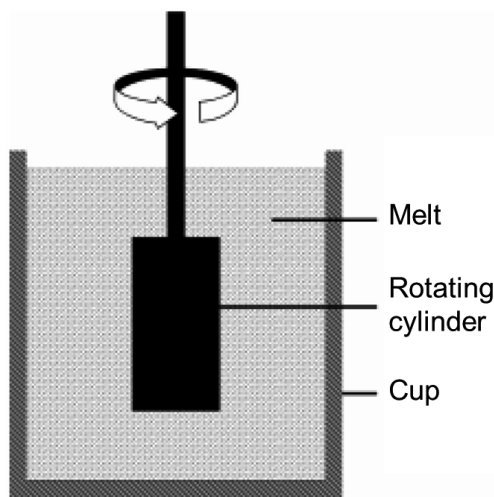


Fig. 2.15. Schematic diagram of the rotating cylinder method [87]

Besides the method of rotated inner cylinder and fixed outer cup, the principle is the same with the method of rotated outer cup and fixed inner cylinder. The rotational method is simple and only several parameters are required to calculate the viscosity. However, the centering of the inner cylinder is very important for the measurement accuracy. Another drawback is that the cylinder is made of refractory material, which may react with the slag at high temperature.

2.4.2 Falling body method

When a solid body (with the shape of sphere, cylinder, or tube) falls through a fluid, both the downward gravitational force and the dragged upwards force due to viscosity act on the body. The resultant force will determine the descent or ascent velocity of the falling body. Using the falling body method, the viscosity is calculated based on Stokes' law.

$$\eta = \frac{2r^2g(\rho_{\text{sphere}} - \rho_{\text{liquid}})}{9v} \quad (2.65)$$

where: η is the viscosity (Pa•s); g is the gravitational acceleration (m/s^2); r is the radius of the sphere (m); v is the velocity of the sphere (m/s); ρ is the density (kg/m^3).

The falling body method is convenient for viscosity measurements. One drawback for this method is that the falling sphere is not totally free. Instead, it is suspended by a very fine thread or wire to control the rate of fall, which makes it difficult to obtain consistent results [88].

2.4.3 Capillary method

Capillary viscometers have also been widely used for measuring viscosity. **Fig. 2.16** shows a schematic diagram of the capillary method. A sample liquid drains or is forced through a fine-pore tube (capillary tube) and the viscosity can be calculated with

$$\eta = \frac{\pi r^4 \Delta p t}{8 V L} \quad (2.66)$$

where: η is the viscosity (Pa•s); Δp is the pressure drop through capillary (kg/ms^2); V the volume of liquid (m^3); t is the time (s); r and L are the radius and length of capillary (m), respectively.

Performing the absolute viscosity measurement is difficult for the capillary viscometer [87]. Therefore, the relative viscosity measurement requiring the calibration of the instrument is often adopted.

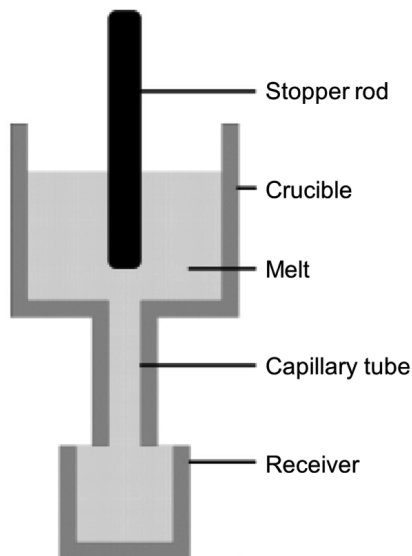


Fig. 2.16. Schematic diagram of the capillary method [87]

2.4.4 Parallel plates method

The parallel plates method can be used to measure the viscosity of samples in the range from 5 to 11 on the logarithmic poise scale. The sample to be tested is sandwiched between two horizontal plates inside a well-insulated furnace, as depicted in **Fig. 2.17(a)**. The upper plate is actually a plunger, with which the sample is loaded and the rate of sagging is recorded as a function of time using a linear voltage displacement transducer or a similar instrument. The deformation of the sample is determined by the viscosity. As shown in **Fig. 2.17(b)**, for no-slip samples, the radial velocity of the sample in contact with the plates is zero, and the viscosity in the case of no-slip can be calculated with [89]

$$\eta = \frac{2\pi Mgh^5}{3V \left(\frac{dh}{dt} \right) (2\pi h^3 + V)} \quad (2.67)$$

where: M is the applied load (kg), g is the gravitational acceleration (m/s^2); dh/dt is the deformation or sagging rate (m/s); h and V are the height (m) and volume (m^3) of the sample, respectively. For perfect-slip samples, the radial velocity is a function of radius only, and thereby the viscosity can be calculated with

$$\eta = \frac{Mgh^2}{3V\left(\frac{dh}{dt}\right)} \quad (2.68)$$

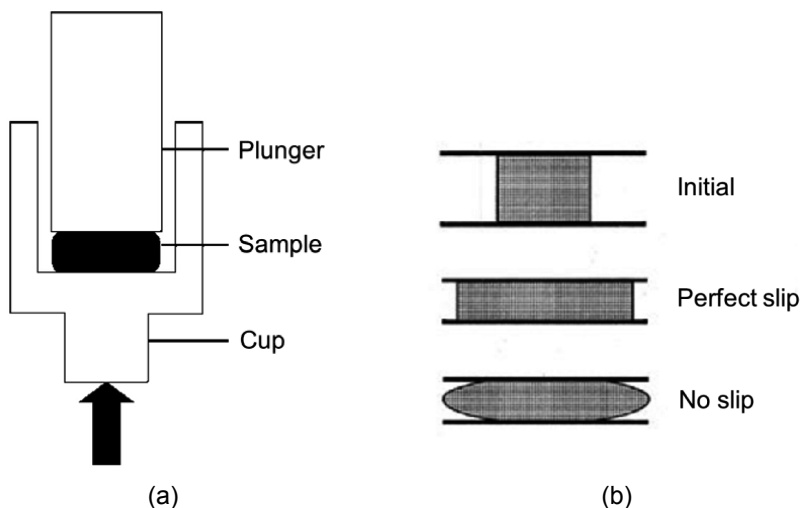


Fig. 2.17. Schematic diagram of the parallel plates method [90] and deformation of the sample [89]

2.4.5 Rod elongation method

The rod elongation method has been widely used for the viscosity measurement in the range from 8 to 14.5 on the logarithmic poise scale. The viscosity is calculated with Eq. (2.69) [19].

$$\eta = \frac{Lmg}{3\pi r^2 v} \quad (2.69)$$

where: v is the elongation velocity (m/s); m is the mass related with the load (kg); g is the gravitational acceleration (m/s^2); L and r are the length and radius of a filament (m), respectively.

3 Experiments

In the experimental study, a rotating cylinder viscometer is used to determine the viscosity. The structure of the apparatus for viscosity measurements is shown in **Fig. 3.1**, which consists of three main components: a rotational viscometer, a magnetic coupling, and a furnace.

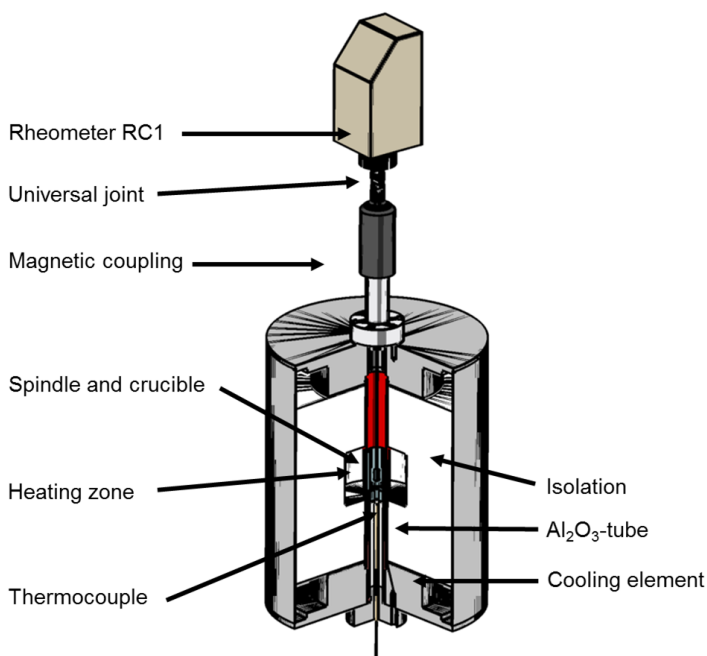


Fig. 3.1. Structure and schematic of the experimental setup for viscosity measurements

The furnace equipped with molybdenum silicide (MoSi_2) heating elements can heat up to the temperature of 1650°C and the pressure within the Al_2O_3 tube can reach up to 5 bar. To achieve a sufficient cooling effect, two independent recycled water cooling systems at the top and bottom of the furnace are designed. Two thermocouples are adopted to control the temperature during the operation. One is used to measure the temperature of crucible; the other is used to detect the temperature of the heating

elements. The furnace should be perpendicular to the ground, which insures that the crucible stands perpendicular to the ground. Otherwise, the centering of the spindle and the crucible cannot be consistent.

More attention should be paid to the gastight joint between the cooling element and the Al_2O_3 tube, as shown in **Fig. 3.1**. Otherwise, the leak of protecting gas will directly change the atmosphere within the Al_2O_3 tube and thereby cause a potential oxidation in the case of the molybdenum crucible and spindle. It brings a deviation of viscosity due to contamination of slag as well as the change in dimension of the crucible and spindle. The viscosity of some systems such as $\text{FeO}/\text{Fe}_2\text{O}_3$ -containing systems is strongly influenced by the partial pressure of oxygen. Moreover, the leak of protecting gas such as argon or hydrogen might cause a serious degradation of the heating elements of MoSi_2 .

A commercial viscometer (Rheometer RC 1) is employed to measure the torque generated by the slag. The technical specification of this viscometer is as follows.

- Maximum torque: 50 mNm
- Resolution of torque: 0.01 mNm
- Range of revolution speed: 0.7–800 r/min
- Accuracy of torque: $\pm 1\%$

The viscometer is originally designed for use at room temperature. Here, it is incorporated into the high temperature furnace by using the magnetic coupling. With this method, the shaft of the viscometer is not exposed to the high temperature, at which the performance of the viscometer such as the measurement accuracy might be influenced. The use of the magnetic coupling can also allow a pressured vessel and thereby the investigation of the pressure dependence of viscosity is feasible. In addition, the partial pressure of oxygen can be easily controlled within the sealed vessel. Then the influence of the partial pressure of oxygen on viscosity of systems containing the transition metal oxides, such as FeO and Fe_2O_3 , can be investigated.

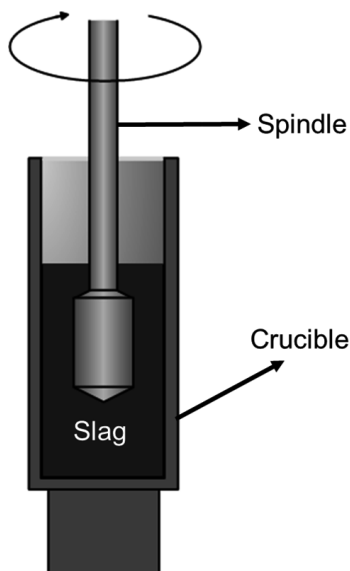


Fig. 3.2. Spindle and crucible

In terms of spindle and crucible (see **Fig. 3.2**), molybdenum is employed due to its high melting temperature (2623°C). The diameters of the bob and crucible are 14 mm and 29 mm, respectively. That means the ratio of radii of crucible and bob is greater than 1.1, and thereby the absolute viscosity measurement is not applicable. Thus, the equipment constant C_0 should be calibrated with liquids of known viscosity, and the viscosity is determined by Eq. (2.64).

To calibrate the viscometer, the first step is to measure the torque losses at the magnetic coupling as well as mechanical joints. By idling the viscometer, the torque losses can be measured. As shown in **Fig. 3.3**, the torque losses linearly increase over the rotational speed. The torque losses remain the same at the constant rotational speeds. It can be seen that the measured torque losses have some random deviations. One source of the deviation is the spindle that involves a certain bending. The spindle with a certain bending cannot rotate perpendicular to the ground, and possibly further results in an undesired turbulence, even a non-Newtonian flow condition between spindle and crucible, which produces a random deviation of the torque measured.

Therefore, the spindle needs to be straightened. Another possible source is the gear joint between the magnetic coupling and viscometer, in which the gears cannot occlude well with each other. Thus, the transmission of torque is not stable, which brings a random deviation. To obtain a better transmission of torque, a universal joint is recommended to replace the gear joint.

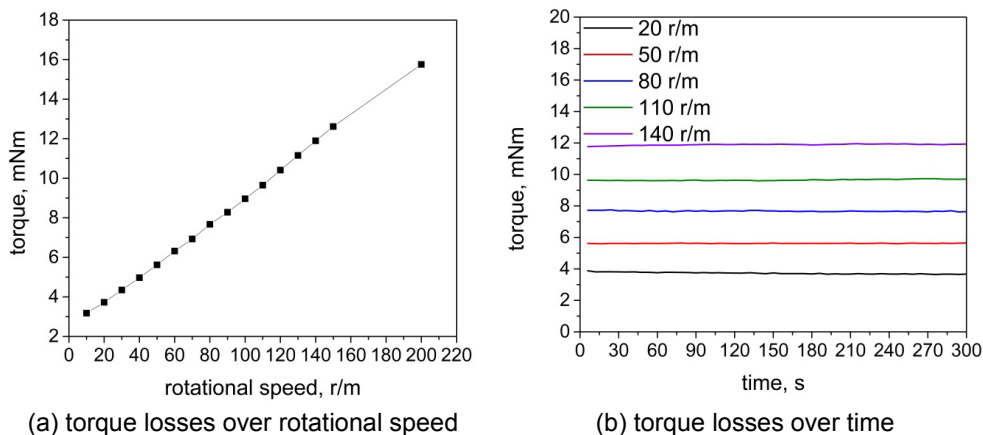


Fig. 3.3. Torque losses over rotational speed and time

It should be pointed out that the deviation of the torque losses sometimes might be greater than the torque generated by the slag. This might cause a negative value of viscosity. To prevent this error, magnitude of the torque losses should be much smaller than that of the torque generated by the slag. It is noted that an increased ratio of torque generated by the slag and torque losses leads to an increased accuracy of viscosity measurement. Normally, such ratio can be increased by increasing the rotational speed. For a given sample of slag, the maximum revolution speed allowed by the viscometer at a certain temperature can be determined before the viscosity measurement, which is performed by the LabVIEW programming.

The magnetic coupling used here normally causes a relative large torque loss. Besides the increased ratio of torque generated by the slag and torque losses, the modification of magnetic coupling might be considered.

Besides the transmission of torque, temperature measurement also needs to be calibrated. The viscosity is strongly dependent on temperature and improper temperature measurement might cause a significant deviation of viscosity. In the current apparatus, the obtained temperature is the temperature of the bottom of the crucible rather than molten slag itself. To detect the temperature deviation, the crucible is filled with alumina powders and the temperature profile along a longitudinal axis is drawn, as shown in **Fig. 3.4**.

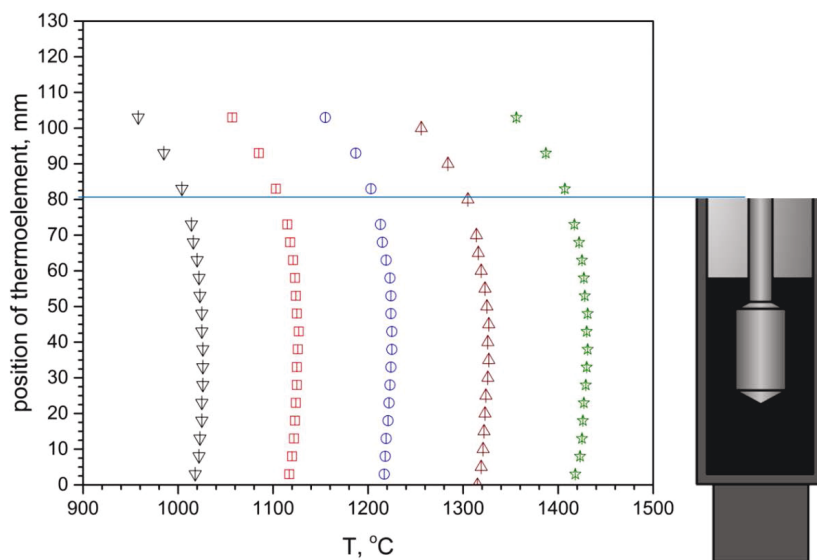


Fig. 3.4. Temperature profile along a longitudinal axis

It was observed that the temperature detected is around 20°C lower than that of slag, although the deviation differs a little at different temperatures.

After calibration of the torque losses and temperature, the equipment constant C_0 is determined with the standard glass, i.e. PTB G3. Then another standard glass, i.e. HVG DGG1, is employed to validate the equipment constant C_0 which is obtained from the standard glass of PTB G3. Reliability of the equipment constant C_0 is shown in **Fig. 3.5**. With the viscometer calibrated, the viscosity of four real coal ashes was measured

under a reducing atmosphere (with protective gas Ar/4%H₂). Before the viscosity measurement, the flow temperature was obtained by the hot stage microscope.

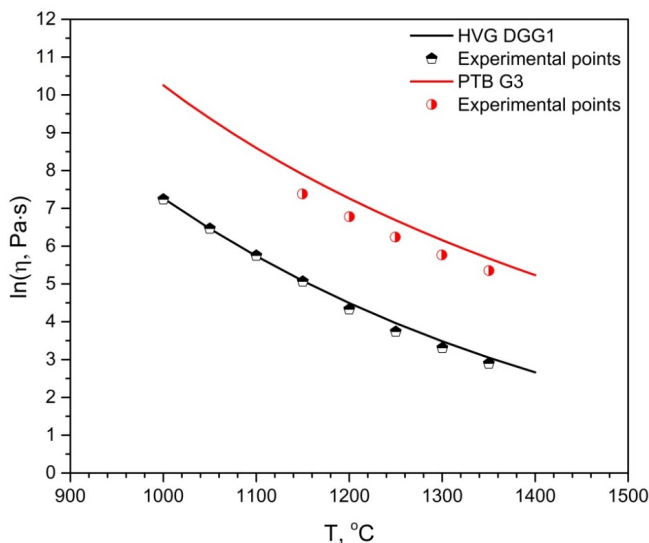


Fig. 3.5. Calibration and validation of viscometer

It should be pointed out that the equipment constant C_0 is dependent on temperature, due to the fact that the dimension of the crucible and spindle does not remain constant due to thermal expansion. Therefore, the equipment constant C_0 determined at room temperature normally cannot be applied at the high temperature.

Due to high-temperature measurement, deviation of slag composition is also paid attention to. The oxidation of spindle and crucible, for example, results in a change of slag composition. Evaporation of alkali oxides also causes an obvious composition deviation, especially at high temperature. Another source of experimental error is the atmosphere, which can seriously influence the oxidation state of transition metal elements, such as iron.

4 Modelling

In the first part of this section, a new viscosity model is firstly developed for pure oxides and binary systems, and then is extended to multicomponent systems without Al_2O_3 and further with Al_2O_3 . Finally, the new model is extended to describe the viscosity of systems containing FeO and Fe_2O_3 . In the second part of this section, a brief description of the optimization procedure for the model parameters is given.

4.1 Model description

The viscosity of a Newtonian fluid is caused by the internal fluid friction, which is related to the momentum transfer between species (i.e. atoms, molecules, or ions), as well as the inter-species forces (i.e. interatomic forces, intermolecular forces, and interionic forces). In view of viscosity mechanism, the viscosity is not only dependent on the size and shape of species, but also on the interaction forces. Therefore, the structure of species involved should be taken into account to study the dependences of viscosity on temperature and composition. In the current viscosity model, the viscosity is linked to the type and distribution of species, as well as the connectivity of species.

The Arrhenius-like models are capable of describing the temperature dependence of viscosity, which can be expressed as

$$\eta = A^* \cdot T^n \cdot \exp\left(\frac{E_\eta}{R \cdot T}\right) \quad (4.1)$$

where: η is the viscosity; T is the absolute temperature; E_η is the activation energy for viscous flow; R is the gas constant; A^* and n are constants. Zhang and Jahanshahi stated that the performances of the Arrhenius-like models are similar in describing the temperature dependence of viscosity [65]. To simplify the model, the constant n is zero in the current viscosity model. Moreover, Eq. (4.1) can be transformed to the logarithmic form.

$$\ln \eta = A + 1000 \cdot B/T \quad (4.2)$$

where: $A = \ln A^*$


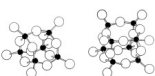
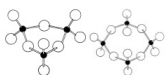
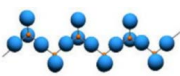
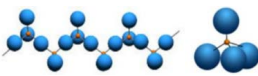

$$B = E_\eta / (1000 \cdot R)$$

Such Arrhenius-like models can effectively calculate the viscosity of a system, which consists of only one species, due to no dependence of the viscosity on composition. A real challenge is now to calculate the viscosity of a multicomponent melt, which consists of various species. The structural dependence of viscosity should be taken into account.

4.1.1 Structural dependence of viscosity

The basic structural units of silicate melts are silica tetrahedra, which can further form a chain structure, a ring structure, or a network structure. As an example, in $\text{SiO}_2\text{--CaO}$ melts the structural change with respect to CaO content is presented in **Table 4.1**.

Table 4.1. Structural change with respect to CaO content in $\text{SiO}_2\text{--CaO}$ melts

CaO, mol%	Structure features	
$X_{\text{CaO}} \leq 12$	3-dimensional network in the form of $[\text{Si}_n \text{O}_{3n}]^{-2n}$	
$12 < X_{\text{CaO}} \leq 33$	Anion complexes in the form of $[\text{Si}_{n-r} \text{O}_{n \cdot (2r+1)}]^{-2n}$	
$33 < X_{\text{CaO}} \leq 50$	Ring structure in the form of $[\text{Si}_n \text{O}_{3n}]^{-2n}$	
$50 < X_{\text{CaO}} \leq 67$	Chain structure in the form of $[\text{Si}_n \text{O}_{3n+1}]^{-2(n+1)}$	
$67 < X_{\text{CaO}} \leq 75$	Chain structure and monomer $[\text{SiO}_4]^{4-}$ and O^{2-}	
$X_{\text{CaO}} > 75$	Monomer $[\text{SiO}_4]^{4-}$ and O^{2-}	

It is seen from **Table 4.1** that with increasing CaO content the silica structure tends to be simpler and smaller, from 3-dimensional network structure, to ring-chain complexes, then further to ring structure and chain structure, finally to silica tetrahedra. It should be pointed out that all these structural units here are only dominant in a range of defined CaO content. Actually, these structural units coexist in dynamic equilibrium with each other. The slag structure has a significant influence on the viscosity. Such a structural change from 3-dimensional network structure to silica tetrahedra causes a decrease in viscosity. As seen from **Fig. 4.1**, with increasing content of CaO the viscosity decreases at temperatures of 1600°C and 1700°C. This indicates that a greater degree of polymerization (larger silica structural units) results in a higher viscosity.

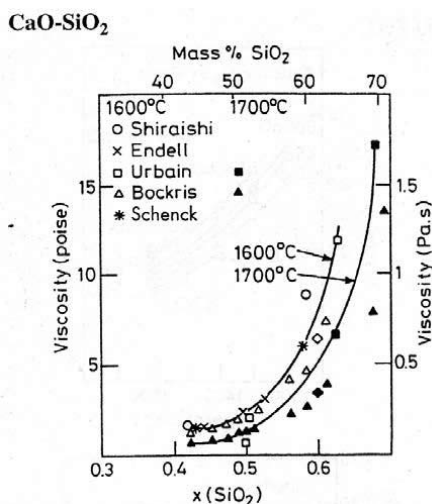


Fig. 4.1. Viscosity of the system $\text{SiO}_2\text{--CaO}$ at temperatures of 1600°C and 1700°C [91]

One simple experiment was carried out to prove this idea. As **Fig. 4.2** shows, with increasing concentration of PVP (a kind of polymer) the viscosity increases at different temperatures from 301 K to 353 K. It is found that addition of the PVP to the water leads to a linear increase in viscosity at the beginning but a sharper increase when the concentration of PVP is above 5%. This change in relationship between viscosity and concentration of PVP could be caused by the behavior of the molecules in the solution.

With increasing concentration of PVP the separate individual polymer chains interconnect with each other and thereby form larger structural units (see **Fig. 4.2**), which cause a dramatic increased viscosity.

In fact, the logarithmic viscosity (in Pa·s) of molten SiO₂-based binary systems can span over 14 orders of magnitude as a function of silica composition, in which a non-linear relationship between viscosity and composition occurs. The internal structure of molten slag should be taken into account to well describe the composition dependence of viscosity.

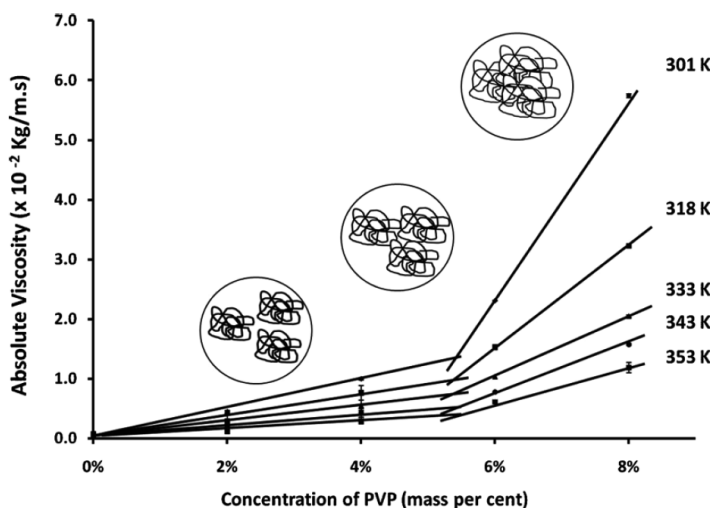


Fig. 4.2. Viscosity of polyvinylpyrrolidone solution of various concentrations at different temperatures [92]

4.1.2 Common structural base between the viscosity and Gibbs energy

To describe the structural change in a multicomponent melt consisting of various species, the type of species needs to be determined firstly. Aune et al. revealed that the viscosity and Gibbs energy have a common structural base [93]. From the experimental

viscosities, common species can be obtained by taking the second derivative of the logarithmic viscosity with respect to composition.

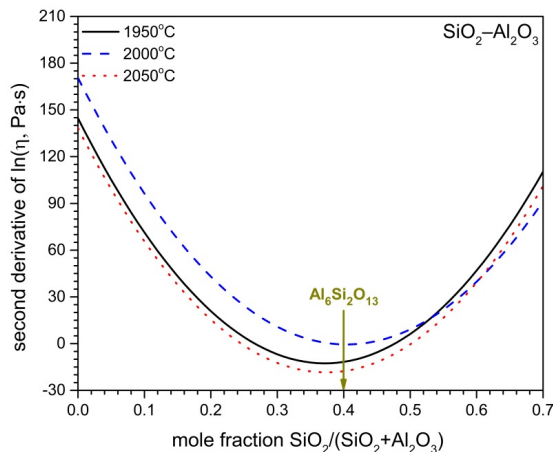


Fig. 4.3. Second derivative of $\ln(\eta)$ with respect to mole fraction of SiO_2 at temperatures of 1950°C, 2000°C, and 2050°C in the system $\text{SiO}_2\text{--Al}_2\text{O}_3$

As shown in **Fig. 4.3**, the minimum points of the lines 1950°C, 2000°C, and 2050°C correspond to the silica mole fractions 0.37, 0.40, and 0.37, respectively. The average value of the silica mole fractions 0.38 is close to the value of 0.4 corresponding to a liquid component (species) $\text{Al}_6\text{Si}_2\text{O}_{13}$, which was introduced for slag using the modified associate species model. On the other hand, this component relates to the solid compound $\text{Al}_6\text{Si}_2\text{O}_{13}$ ($=3\text{Al}_2\text{O}_3 \cdot 2\text{SiO}_2$, mullite) which was first identified by Bowen and Greig [94] in the phase diagram of the binary system $\text{SiO}_2\text{--Al}_2\text{O}_3$. With the same method, the common species CaSiO_3 and $\text{Na}_2\text{Si}_2\text{O}_5$ are obtained for the systems $\text{SiO}_2\text{--CaO}$ and $\text{SiO}_2\text{--Na}_2\text{O}$, respectively, as seen from **Figs. 4.4** and **4.5**. It is found that not all necessary common species can be identified by taking the second derivative of the logarithmic viscosity with respect to composition, which might be caused by the lack of experimental data covering the whole range of compositions. Nevertheless, it has been clearly indicated that a common structural base arises between the viscosity and Gibbs

energy and furthermore the viscosity of high temperature melts can be appropriately described by coupling the Gibbs energy and viscosity [93].

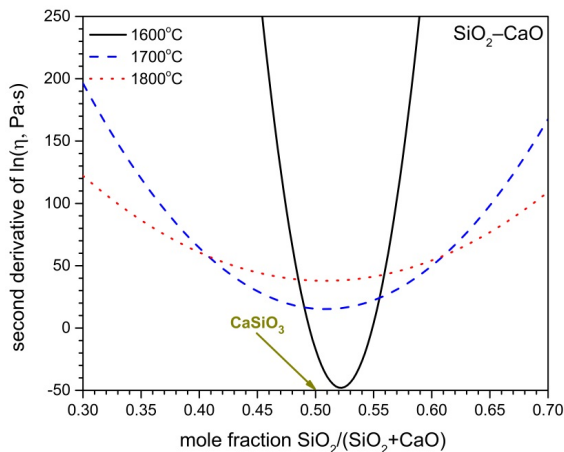


Fig. 4.4. Second derivative of $\ln(\eta)$ with respect to mole fraction of SiO_2 at temperatures of 1600°C , 1700°C , and 1800°C in the system $\text{SiO}_2\text{--CaO}$

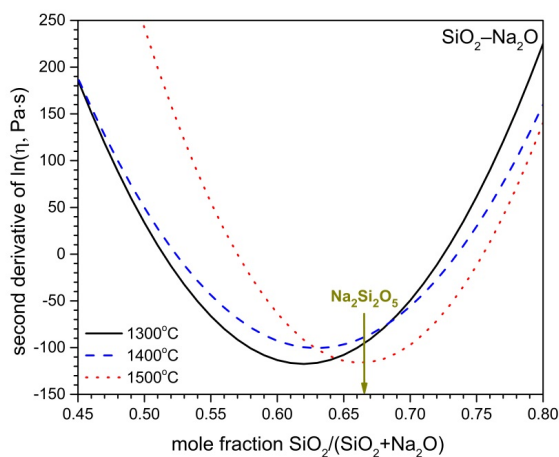


Fig. 4.5. Second derivative of $\ln(\eta)$ with respect to mole fraction of SiO_2 at temperatures of 1300°C , 1400°C , and 1500°C in the system $\text{SiO}_2\text{--Na}_2\text{O}$

4.1.3 Description of the Gibbs energy using the modified associate species model

Since the viscosity and Gibbs energy have the same structural base, the type of species can be determined from the Gibbs energy. The modified associate species model, used by Besmann and Spear [95] and applied for the slag relevant oxide systems [96–100], is employed to describe the Gibbs energy of the liquid phase, which can be expressed by Eq. (4.3).

$$G = \sum_i X_i \cdot G_i^0 + R \cdot T \cdot \sum_i X_i \cdot \ln X_i + G^{\text{ex}} \quad (4.3)$$

where: subscript i represents i -th associate species in solution; X_i is the mole fraction; G_i^0 is the Gibbs energy of the pure i -th associate species; R is the gas constant, T is the absolute temperature; G^{ex} is the excess Gibbs energy to summarize all other contributions to the Gibbs energy except for the entropy contribution, which can be expressed by the following equation according to the Redlich-Kister polynomial relationship.

$$G^{\text{ex}} = \sum_{i < j} \sum X_i \cdot X_j \sum_{k=0}^{n_{ij}} L_{ij}^{(k)} (X_i - X_j)^k \quad (4.4)$$

where: $L_{ij}^{(k)}$ is the interaction coefficient between corresponding i -th and j -th associate species, which is given by

$$L_{ij}^{(k)} = A_{ij}^{(k)} + B_{ij}^{(k)} \cdot T + C_{ij}^{(k)} \cdot T \cdot \ln T + D_{ij}^{(k)} \cdot T^2 + \dots \quad (4.5)$$

where: $A_{ij}^{(k)}$, $B_{ij}^{(k)}$, $C_{ij}^{(k)}$, $D_{ij}^{(k)}$ etc. are the interaction parameters. In general, it is sufficient to consider the first two terms to describe the change in Gibbs energy.

Using this modified associate species model and optimized thermodynamic parameters, a good agreement in terms of phase diagrams and activities is achieved. For example, the phase diagram of the binary system $\text{SiO}_2\text{--Al}_2\text{O}_3$, as shown in **Fig. 4.7**, is reproduced

very well. Also, the reproduction of liquidus surface in the ternary system $\text{SiO}_2\text{--Al}_2\text{O}_3\text{--CaO}$ is performed very well, as presented in **Fig. 4.6**.

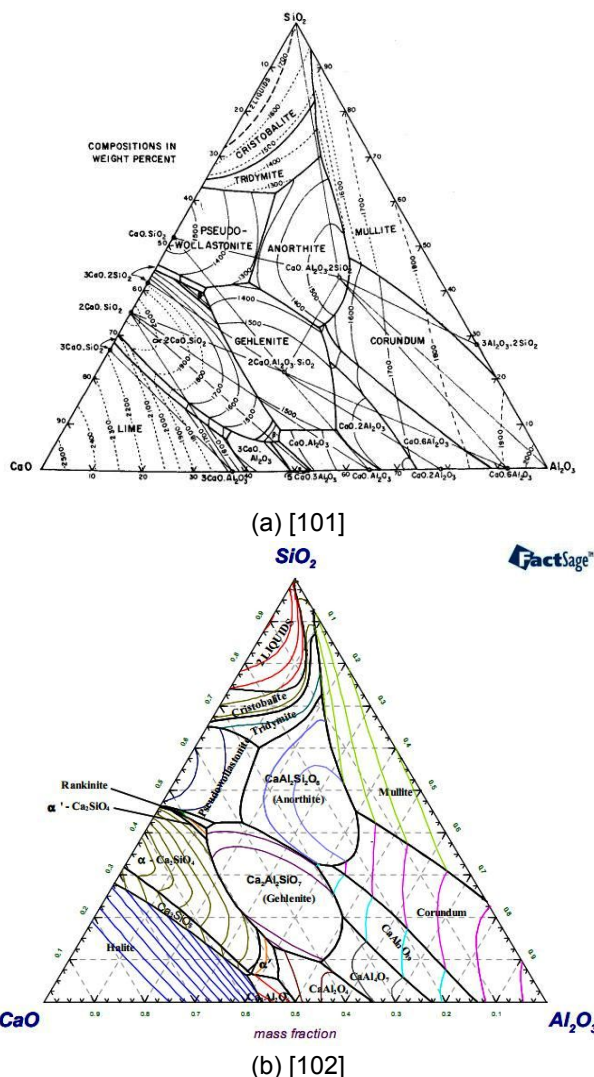


Fig. 4.6. Accordance of the phase diagram of the system $\text{SiO}_2\text{--Al}_2\text{O}_3\text{--CaO}$ between experimental points (a) and model predictions (b)

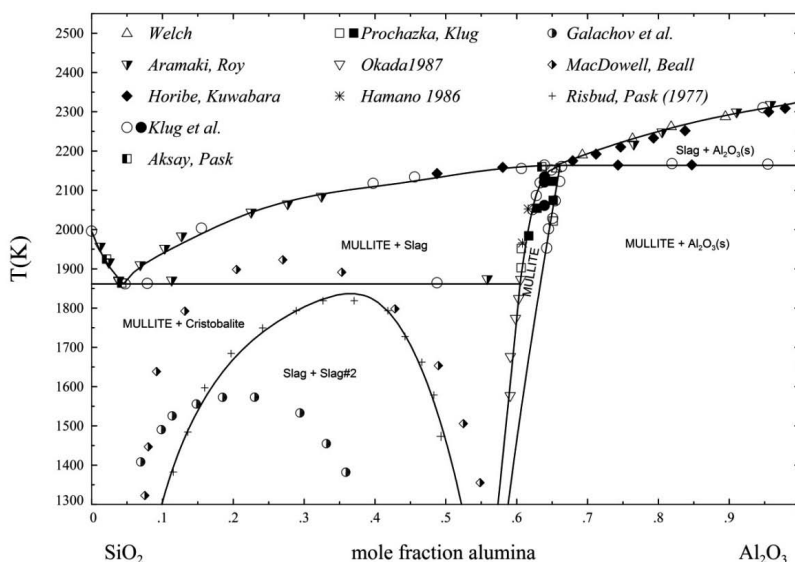


Fig. 4.7. Phase diagram of the system SiO_2 - Al_2O_3 [98]

4.1.4 Linking the viscosity of slag to its structure

Since the Gibbs energy for the slag is well described with the modified associate species model, in which each associate species represents one type of stoichiometric species, the associate species can be considered to be reasonable for the common structural base. It should be pointed out that each associate species employed in the modified associate species model is expressed with the formula that contains a total of two non-oxygen atoms allowing equal weighting of each associate species with regard to its entropic contribution in the ideal mixing term [95], as shown in **Table 4.2**.

The modified associate species model can also give a reliable distribution of associate species, which is consistent with the experimental Q^n species distribution. From **Fig. 4.9**, the associate species distribution is in good agreement with the Q^n species distribution [103–105] obtained from NMR and Raman spectra for the system SiO_2 - Na_2O , in which

the species Q^2 , Q^3 , and Q^4 correspond to the associate species Na_2SiO_3 , $Na_2Si_2O_5$, and SiO_2 , respectively.

Table 4.2. Definition of associate species and structural units for pure oxides and binary systems

Compounds	Associate species	Structural units
SiO_2	Si_2O_4	SiO₂
Al_2O_3	Al_2O_3	AlO_{1.5}
CaO	Ca_2O_2	CaO
MgO	Mg_2O_2	MgO
Na_2O	Na_2O	NaO_{0.5}
K_2O	K_2O	KO_{0.5}
$Al_6Si_2O_{13}$	$\frac{1}{4} \cdot Al_6Si_2O_{13}$	Al₃SiO_{6.5}
$CaSiO_3$	$CaSiO_3$	CaSiO₃
Ca_2SiO_4	$\frac{2}{3} \cdot Ca_2SiO_4$	Ca₂SiO₄
$MgSiO_3$	$MgSiO_3$	MgSiO₃
Mg_2SiO_4	$\frac{2}{3} \cdot Mg_2SiO_4$	Mg₂SiO₄
Na_4SiO_4	$\frac{2}{5} \cdot Na_4SiO_4$	Na₄SiO₄
Na_2SiO_3	$\frac{2}{3} \cdot Na_2SiO_3$	Na₂SiO₃
$Na_2Si_2O_5$	$\frac{1}{2} \cdot Na_2Si_2O_5$	NaSiO_{2.5}
K_2SiO_3	$\frac{2}{3} \cdot K_2SiO_3$	K₂SiO₃
$K_2Si_2O_5$	$\frac{1}{2} \cdot K_2Si_2O_5$	KSiO_{2.5}
$K_2Si_4O_9$	$\frac{1}{3} \cdot K_2Si_4O_9$	K_{0.5}SiO_{2.25}
$CaAl_2O_4$	$\frac{2}{3} \cdot CaAl_2O_4$	Ca_{0.5}AlO₂
$MgAl_2O_4$	$\frac{2}{3} \cdot MgAl_2O_4$	Mg_{0.5}AlO₂
$NaAlO_2$	$NaAlO_2$	NaAlO₂
$KAlO_2$	$KAlO_2$	KAlO₂

The associate species distribution gives a good base to represent the internal structure of the slag. It is noted that the associate species are independent molecular-like complexes, which are not stable substances in melts but nevertheless in dynamic equilibrium with each other. Each associate species represents one kind of structural unit. **Fig. 4.8** illustrates the structure of the associate species CaSiO_3 , as well as its contour.

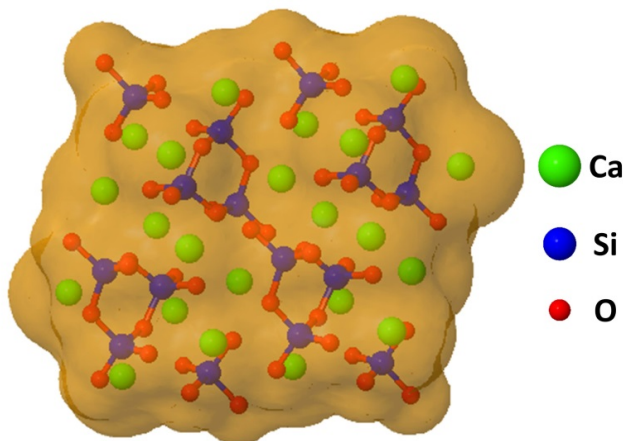


Fig. 4.8. Structural representation of the associate species CaSiO_3 [106]

The slag structure, therefore, at some level can be described with the associate species distribution. As shown in **Fig. 4.9**, the species Na_4SiO_4 , instead of a silica network structure, forms at the beginning by adding SiO_2 to pure Na_2O at a temperature of 1200°C . When the mole fraction of SiO_2 reaches 0.25, the species Na_2SiO_3 starts to form. Then, the formation of the species $\text{Na}_2\text{Si}_2\text{O}_5$ and SiO_2 occurs when the mole fraction of SiO_2 is approaching 1. Each species is dominant in a range of defined composition. For example, the species $\text{Na}_2\text{Si}_2\text{O}_5$ prevails in the range from 0.55 to 0.8 mole fraction of silica. For the fully liquid systems $\text{SiO}_2\text{--CaO}$ and $\text{SiO}_2\text{--CaO--Na}_2\text{O}$ the structural change represented with the distribution of associate species is also shown in **Figs. 4.10** and **4.11**, respectively.

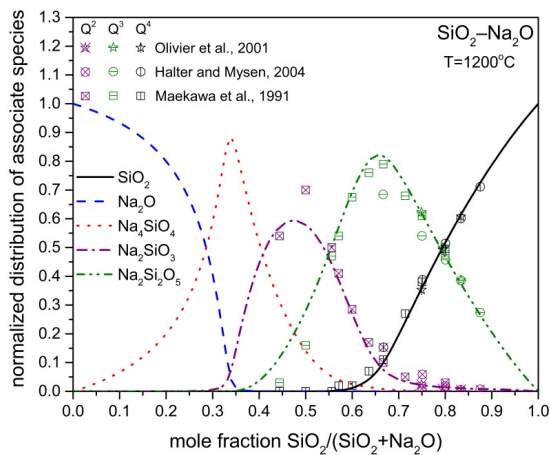


Fig. 4.9. Normalized distribution of associate species for the system $\text{SiO}_2\text{--Na}_2\text{O}$

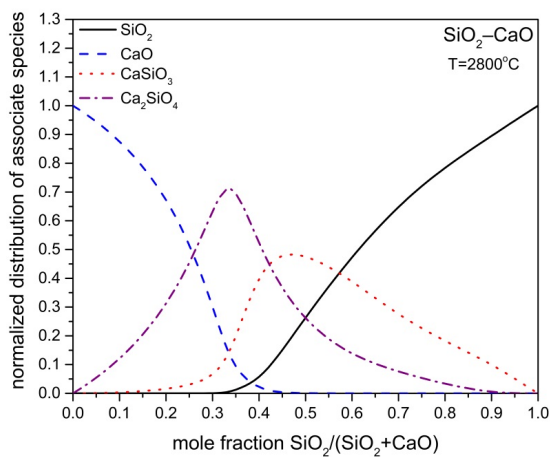


Fig. 4.10. Normalized distribution of associate species in the fully liquid system $\text{SiO}_2\text{--CaO}$ at 2800°C

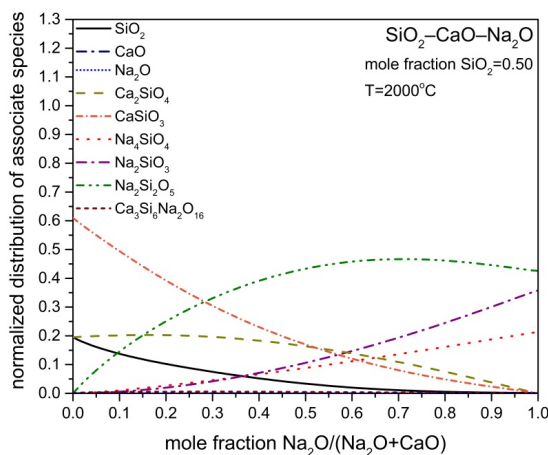


Fig. 4.11. Normalized distribution of associate species in the fully liquid system SiO_2 – CaO – Na_2O at 2000°C and 0.50 mole fraction SiO_2

However, it is not sufficient to describe the dependence of viscosity on structure using only the associate species distribution due to the fact that the associate species themselves are not sensitive to their own connectivity. In a pure silica melt, for example, the structure is described with only one associate species SiO_2 . In fact, the pure silica melt consists of various silica clusters [28, 107], which can be related to the connectivity of the associate species SiO_2 . A higher degree of connectivity results in a larger structural unit, and therefore an increased viscosity.

The connectivity of each associate species can be reflected by the degree of polymerization reaction. In principle, all potential polymerizations should be considered to describe the structural change with respect to temperature and composition. However, this introduces a high number of model parameters and increases the computing time. In the current viscosity model, the main polymerizations are abstracted as silica polymerizations due to the fact that the polymerizations occur mainly through linking silica tetrahedra. Furthermore, not all silica polymerizations have a significant contribution to the viscosity. Only when the size of a silica cluster which results from silica polymerization reaches a critical value [77], the viscosity can dramatically increase.

It is also noted that the silica polymerization is independent of the nature of the silicate melt, reported by Zaitsev and Mogutnov [108].

4.1.5 Viscosity of the pure oxides and binary systems

The viscosity of the system consisting of various species, therefore, can be described with two parts: an ideal viscosity part and an excess viscosity part. The ideal viscosity part is based on the assumption that every associate species is a discrete structural unit without any polymerization. As listed in **Table 4.2**, the discrete structural units are expressed with the formula that contains only one reference atom (marked in bold), which has the same composition as the associate species. To simplify the formula of the discrete structural unit, a simple stoichiometry as shown in the column of compounds in **Table 4.2** is used hereafter. In the framework of the discrete structural units, the sizes of all associate species involved are at a comparable scale, i.e. the monomer-like scale. This kind of associate species is described as monomeric associate species and the viscosity contributed from this scale is defined as the ideal viscosity part. Whereas the viscosity contributed from higher scales is defined as the excess part of viscosity, which results from the critical silica polymerizations that have significant contributions to the viscosity. In the SiO₂-based binary systems, the excess viscosity part can be described by relying on two common critical silica clusters, i.e. (SiO₂)_{n₁} and (SiO₂)_{n₂}, which are products of the self-polymerization of silica. Consequently, the viscosity is calculated with Eq. (4.6).

$$\begin{aligned}\ln \eta &= \ln \eta_{\text{ideal}} + \ln \eta_{\text{excess}} \\ &= (\sum_i X_i \cdot \ln \eta_i) + (\ln \eta_{\text{SiO}_2\text{-pol.}}),\end{aligned}\quad (4.6)$$

where: $\ln \eta_i = A_i + B_i/T$,

$$\begin{aligned}\ln \eta_{\text{SiO}_2\text{-pol.}} &= \sum_j (A_{(\text{SiO}_2)_{n_j}} + B_{(\text{SiO}_2)_{n_j}}/T) \cdot (X_{\text{SiO}_2}^{n_j}), \\ j &= 1, 2.\end{aligned}$$

η_{ideal} and η_{excess} are the ideal viscosity part and the excess viscosity part respectively; X_i is the mole fraction of the monomeric associate species i ; η_i is the viscosity

contribution from the monomeric associate species i ; $\eta_{\text{SiO}_2\text{-pol.}}$ is the excess viscosity part resulting from the critical silica polymerizations; n_j is the integer coefficient that relates to a particular degree of polymerization; A_i and B_i are the temperature and composition independent constants respectively for the ideal viscosity part; $A_{(\text{SiO}_2)_{n_j}}$ and $B_{(\text{SiO}_2)_{n_j}}$ are the temperature and composition independent constants respectively for the excess viscosity part; T is the absolute temperature; $X_{\text{SiO}_2}^{n_j}$ is the weighting factor indicating the relative contribution of the excess viscosity part. The weighting factor is derived from the mole fraction of the critical silica cluster. In view of chemical equilibrium, there is a dynamic equilibrium between the monomeric associate species SiO_2 and the critical silica cluster $(\text{SiO}_2)_{n_j}$, as shown in Eq. (4.7).

$$n_j \text{SiO}_2 = (\text{SiO}_2)_{n_j} \quad (4.7)$$

The mole fraction of the critical silica cluster, therefore, can be calculated by the mole fraction of the monomeric associate species SiO_2 , as shown in Eq. (4.8).

$$X_{(\text{SiO}_2)_{n_j}} = K_{n_j} \cdot X_{\text{SiO}_2}^{n_j} \quad (4.8)$$

where: $X_{(\text{SiO}_2)_{n_j}}$ is the mole fraction of the critical silica cluster $(\text{SiO}_2)_{n_j}$, K_{n_j} is an equilibrium constant for a particular degree of polymerization. Here, the mole fraction in place of activity is used to calculate the mole fraction of the critical silica cluster. To simplify the equation to estimate the excess viscosity part, the equilibrium constant K_{n_j} is implicitly incorporated into the model parameters $A_{(\text{SiO}_2)_{n_j}}$ and $B_{(\text{SiO}_2)_{n_j}}$. Moreover, a possible dependence of K_{n_j} on temperature is ignored.

4.1.6 Viscosity of the multicomponent systems without Al_2O_3

In the current model the viscosity is linked to the type and distribution of species, as well as the connectivity of species. With the same principle, the model can be extended to describe the viscosity of multicomponent systems. For multicomponent systems, the monomeric associate species used for the description of the slag structure may contain

some ternary associate species besides the monomeric associate species for the pure oxides and binary systems. In the ternary system $\text{SiO}_2\text{--MgO--K}_2\text{O}$ two ternary associate species K_2SiMgO_4 and $\text{K}_2\text{Si}_5\text{MgO}_{12}$ are employed to describe the structural dependence of the viscosity, while no ternary associate species are required for the ternary system $\text{SiO}_2\text{--MgO--CaO}$. The viscosity of the ternary system $\text{SiO}_2\text{--MgO--CaO}$, in consequence, can be directly extrapolated from the binary systems $\text{SiO}_2\text{--MgO}$ and $\text{SiO}_2\text{--CaO}$, in which the optimized model parameters for the pure oxides and binary systems remain constant.

In the multicomponent systems without Al_2O_3 , four ternary associate species $\text{Na}_2\text{Si}_6\text{Ca}_3\text{O}_{16}$, K_2SiCaO_4 , K_2SiMgO_4 , and $\text{K}_2\text{Si}_5\text{MgO}_{12}$ are employed for the description of the slag structure, and the remaining monomeric associate species are identical to those used in the pure oxides and binary systems. The sizes of the four ternary associate species are subjected to the monomer-like scale, which behave like the other monomeric associate species, such as CaSiO_3 and $\text{Na}_2\text{Si}_2\text{O}_5$. Their viscosity contribution can be effectively described in the framework of the ideal viscosity part. Therefore, the viscosity of the multicomponent systems without Al_2O_3 can be calculated with Eq. (4.6), i.e. the model developed for pure oxides and binary systems.

4.1.7 Viscosity of the Al_2O_3 -containing multicomponent systems

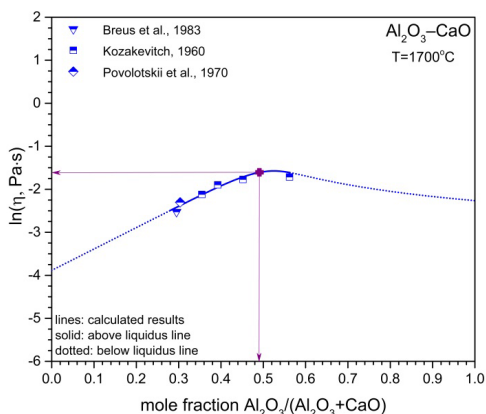
In the Al_2O_3 -containing multicomponent systems, three kinds of Al^{3+} -containing associate species, as listed in **Table 4.3**, are employed to describe the Al^{3+} -induced structural change. These associate species indicate the different structural roles of Al^{3+} depending on composition and temperature and are in dynamic equilibrium with each other. For the type of non-tetrahedra, Al^{3+} plays the role of a network modifier. When Al^{3+} is charge-compensated by Ca^{2+} , Mg^{2+} , Na^+ , or K^+ and forms a quasi-tetrahedron, Al^{3+} behaves as a network former. Although the Al^{3+} -based quasi-tetrahedra CaAl_2O_4 , MgAl_2O_4 , NaAlO_2 , KAlO_2 , and $\text{Ca}_3\text{Al}_{10}\text{Na}_4\text{O}_{20}$ behave like silica tetrahedra, these quasi-tetrahedra themselves are not capable of forming large network structures, which is indirectly proved by the magnitude of the viscosity of the Al_2O_3 -containing binary systems.

Table 4.3. The Al^{3+} -containing associate species and structural units

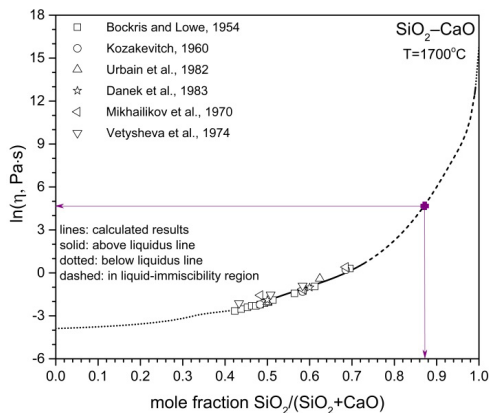
Type of structures	Compounds	Associate species	Structural units
Non-tetrahedra	Al_2O_3	Al_2O_3	$\text{AlO}_{1.5}$
	$\text{Al}_6\text{Si}_2\text{O}_{13}$	$\frac{1}{4} \cdot \text{Al}_6\text{Si}_2\text{O}_{13}$	$\text{Al}_3\text{SiO}_{6.5}$
	$\text{Na}_2\text{Al}_4\text{O}_7$	$\frac{1}{3} \cdot \text{Na}_2\text{Al}_4\text{O}_7$	$\text{Na}_{0.5}\text{AlO}_{1.75}$
	$\text{K}_2\text{Al}_4\text{O}_7$	$\frac{1}{3} \cdot \text{K}_2\text{Al}_4\text{O}_7$	$\text{K}_{0.5}\text{AlO}_{1.75}$
Al^{3+} -based quasi-tetrahedra	CaAl_2O_4	$\frac{2}{3} \cdot \text{CaAl}_2\text{O}_4$	$\text{Ca}_{0.5}\text{AlO}_2$
	MgAl_2O_4	$\frac{2}{3} \cdot \text{MgAl}_2\text{O}_4$	$\text{Mg}_{0.5}\text{AlO}_2$
	NaAlO_2	NaAlO_2	NaAlO_2
	KAlO_2	KAlO_2	KAlO_2
	$\text{Ca}_3\text{Al}_{10}\text{Na}_4\text{O}_{20}$	$\frac{2}{17} \cdot \text{Ca}_3\text{Al}_{10}\text{Na}_4\text{O}_{20}$	$\text{Ca}_{0.3}\text{AlNa}_{0.4}\text{O}_2$
Al^{3+} -based quasi-tetrahedra bonded with SiO_2 tetrahedra	$\text{CaSi}_2\text{Al}_2\text{O}_8$	$\frac{2}{5} \cdot \text{CaSi}_2\text{Al}_2\text{O}_8$	$\text{Ca}_{0.5}\text{SiAlO}_4$
	$\text{Mg}_2\text{Si}_5\text{Al}_4\text{O}_{18}$	$\frac{2}{11} \cdot \text{Mg}_2\text{Si}_5\text{Al}_4\text{O}_{18}$	$\text{Mg}_{0.4}\text{SiAl}_{0.8}\text{O}_{3.6}$
	NaSiAlO_4	$\frac{2}{3} \cdot \text{NaSiAlO}_4$	NaSiAlO_4
	$\text{NaSi}_3\text{AlO}_8$	$\frac{2}{5} \cdot \text{NaSi}_3\text{AlO}_8$	$\text{Na}_{1/3}\text{SiAl}_{1/3}\text{O}_{8/3}$
	KSiAlO_4	$\frac{2}{3} \cdot \text{KSiAlO}_4$	KSiAlO_4
	KSi_2AlO_6	$\frac{1}{2} \cdot \text{KSi}_2\text{AlO}_6$	$\text{K}_{0.5}\text{SiAl}_{0.5}\text{O}_3$

Fig. 4.12 shows that the experimental data [109–111] are well reproduced with the model developed for pure oxides and binary systems. It can also be seen from this figure that the logarithmic viscosities of the systems SiO_2 – CaO and Al_2O_3 – CaO are 4.7 and -1.6 respectively at 1700°C for a constant content (0.87 mole fraction) of tetrahedral structural units (SiO_2 and CaAl_2O_4 for the systems SiO_2 – CaO and Al_2O_3 – CaO , respectively) corresponding to the maximum of the CaAl_2O_4 species at this temperature, **Fig. 4.12(c)**. That is, at this condition the absolute viscosity value of the system SiO_2 – CaO is about 540 times larger than that of the system Al_2O_3 – CaO , which implies that the polymerization of the quasi-tetrahedron CaAl_2O_4 is very limited

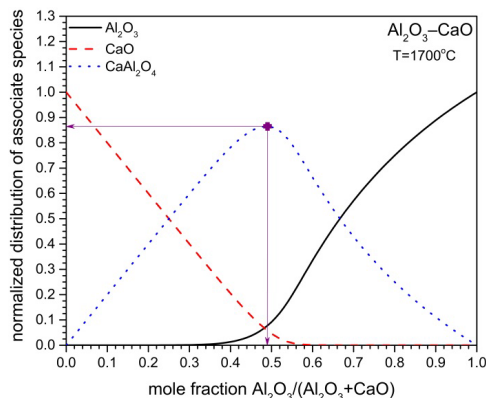
compared to the polymerization of the tetrahedron SiO_2 . Nevertheless, when SiO_2 is present, the Al^{3+} -based quasi-tetrahedra can easily interconnect with the silica network structure, and hence form larger structural units, whose sizes are not within the monomer-like scale. These resulting larger structural units, in general, cause a significant increase in viscosity. Thus, the viscosity contributed from higher scales cannot be described with only two common critical silica clusters.



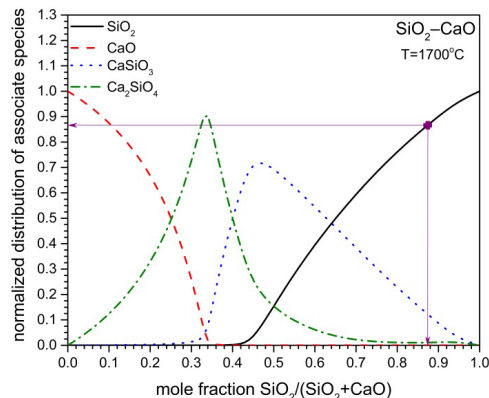
(a) viscosity of the system Al_2O_3 -CaO at 1700°C



(b) viscosity of the system SiO_2 -CaO at 1700°C



(c) associate species distribution of the system Al_2O_3 -CaO at 1700°C



(d) associate species distribution of the system SiO_2 -CaO at 1700°C

Fig. 4.12. Viscosity comparison of the systems Al_2O_3 -CaO and SiO_2 -CaO at 1700°C for the same concentration of the tetrahedral structural units

To effectively describe the excess viscosity part for the Al_2O_3 -containing multicomponent systems, two kinds of the polymerization are introduced, which are described as self- and inter-polymerization. It is assumed that both the Al^{3+} -based quasi-tetrahedra and silica tetrahedra can self-polymerize. Due to the fact that the silica polymerization is independent of the nature of the silicate melt, the self-polymerization of silica tetrahedra is already described with two common critical silica clusters. Thus, the remaining self-polymerization is mainly caused by the Al^{3+} -based quasi-tetrahedra. As **Fig. 4.12** implies, the degree of the self-polymerization for only Al^{3+} -based quasi-tetrahedra is very small and can be ignored. However, the presence of silica causes an increased degree of self-polymerization of the Al^{3+} -based quasi-tetrahedra, which is described by making use of the silicon-aluminium based ternary associate species as listed in **Table 4.3**. Nevertheless, not all potential degrees of self-polymerization of each associate species involved are introduced. Similar to the treatment of silica polymerization, here only one critical self-polymerization of each associate species involved is employed to describe the excess viscosity part resulting from the self-polymerization of the Al^{3+} -based quasi-tetrahedra that bond with the silica tetrahedra. Therefore, the excess viscosity part caused by the self-polymerization is given by

$$\ln \eta_{\text{self-pol.}} = \sum_j (A_{(\text{SiO}_2)_{n_j}} + B_{(\text{SiO}_2)_{n_j}}/T) \cdot (X_{\text{SiO}_2}^{n_j}) + \sum_k (A_{(\text{Si-Al})_k} + B_{(\text{Si-Al})_k}/T) \cdot (X_{(\text{Si-Al})_k}^{n_k}), \quad (4.9)$$

where: $j = 1, 2$.

$$k = 1, 2, 3, \dots$$

$(\text{Si-Al})_k$: the silicon-aluminium based ternary associate species,

n_k : the integer coefficient that relates to a particular degree of self-polymerization.

Besides the self-polymerization, the Al^{3+} -based quasi-tetrahedra can inter-polymerize with the silica tetrahedra. During the inter-polymerization, the Al^{3+} -based quasi-tetrahedra interconnect with the silica network structures, and thereby give a sharp

increase in viscosity because of the formation of larger silica network structures. The Al^{3+} -based quasi-tetrahedra that link to the silica network structure are described by relying on the silicon-aluminium based ternary associate species. Similar to the treatment of the self-polymerization, only one critical inter-polymerization for each associate species involved is employed to describe the excess viscosity part resulting from the inter-polymerization. Therefore, the excess viscosity part caused by the inter-polymerization is given by

$$\ln \eta_{\text{inter-pol.}} = \sum_m (A_{(\text{Si-Al})_m} + B_{(\text{Si-Al})_m}/T) \cdot (X_{(\text{Si-Al})_m} \cdot X_{\text{SiO}_2}^{n_m}), \quad (4.10)$$

where: $m = 1, 2, 3 \dots$

$(\text{Si} - \text{Al})_m$: the silicon-aluminium based ternary associate species,

n_m : the integer coefficient that relates to a particular degree of inter-polymerization.

Combining Eq. (4.9) and Eq. (4.10) the excess viscosity part for the Al_2O_3 -containing multicomponent systems is given by

$$\begin{aligned} \ln \eta_{\text{excess}} &= \ln \eta_{\text{self-pol.}} + \ln \eta_{\text{inter-pol.}} \\ &= \sum_j (A_{(\text{SiO}_2)_{n_j}} + B_{(\text{SiO}_2)_{n_j}}/T) \cdot (X_{\text{SiO}_2}^{n_j}) \\ &\quad + \sum_k (A_{(\text{Si-Al})_k} + B_{(\text{Si-Al})_k}/T) \cdot (X_{(\text{Si-Al})_k}^{n_k}) \\ &\quad + \sum_m (A_{(\text{Si-Al})_m} + B_{(\text{Si-Al})_m}/T) \cdot (X_{(\text{Si-Al})_m} \cdot X_{\text{SiO}_2}^{n_m}) \end{aligned} \quad (4.11)$$

Hence, the viscosity of the Al_2O_3 -containing multicomponent systems is described with Eq. (4.6), where the $\ln \eta_{\text{excess}}$ term is replaced with Eq. (4.11).

4.1.8 Viscosity of the $\text{FeO}/\text{Fe}_2\text{O}_3$ -containing systems

In the $\text{FeO}/\text{Fe}_2\text{O}_3$ -containing systems, one challenge is to describe the redox reaction of Fe^{2+} and Fe^{3+} . The redox reaction of Fe^{2+} and Fe^{3+} as a function of temperature,

composition and partial pressure of oxygen can be well described by way of the associate species distribution, which is calculated by using a completely self-consistent thermodynamic dataset. For example, the ferrous-ferric ratio for the system Fe_2O_3 – CaO is displayed by the associate species distribution, as seen from **Fig. 4.13**. It is noted that the ferrous-ferric ratio is dependent on temperature, composition and partial pressure of oxygen.

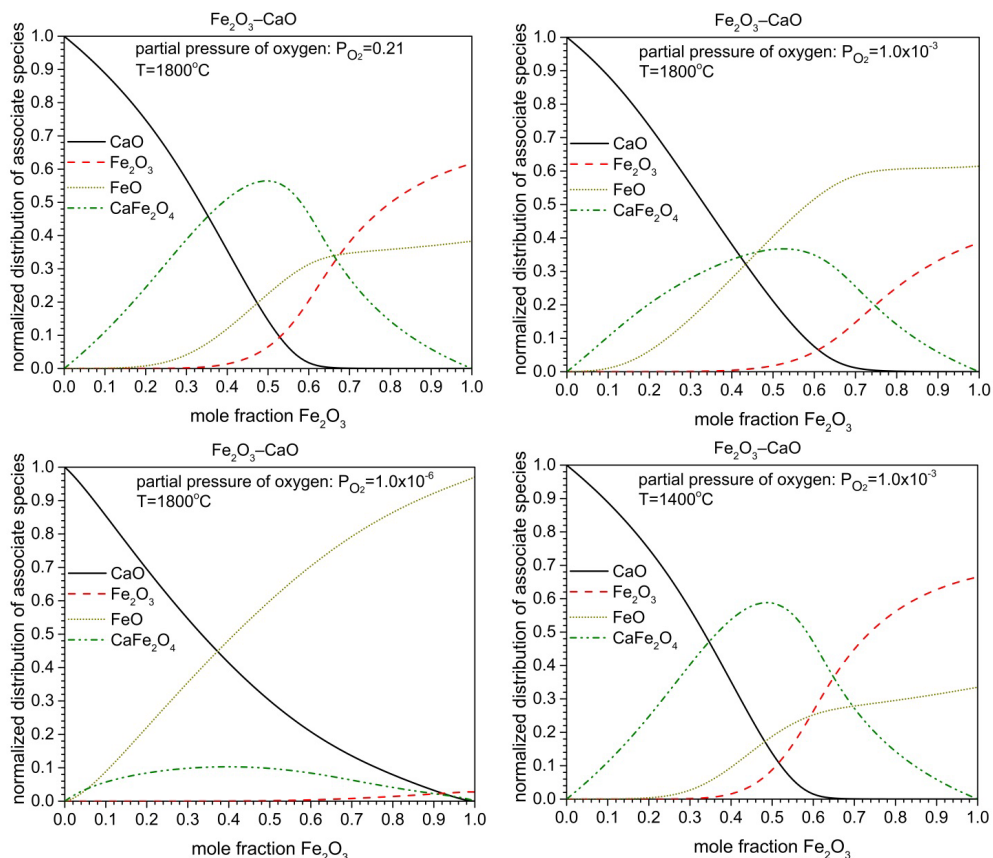


Fig. 4.13. The associate species distribution in the system Fe_2O_3 – CaO

When modelling the viscosity of the $\text{FeO}/\text{Fe}_2\text{O}_3$ -containing systems, another challenge arises due to the fact that Fe^{2+} behaves as a network modifier whereas Fe^{3+} plays the role of an amphoteric. For description of the $\text{Fe}^{2+}/\text{Fe}^{3+}$ -induced structural change in the system SiO_2 – Al_2O_3 – CaO – MgO – Na_2O – K_2O – FeO – Fe_2O_3 , 14 Fe-containing associate

species are employed, as listed in **Table 4.4**. The structural role of each associate species is clearly indicated. For instance, the associate species CaFe_2O_4 , MgFe_2O_4 , NaFeO_2 , and KFeO_2 presenting Fe^{3+} -based quasi-tetrahedra behave as network formers, in which Fe^{3+} is charge-compensated by Ca^{2+} , Mg^{2+} , Na^+ , or K^+ . Moreover, not all Fe^{3+} behave as network formers. The associate species Fe_2O_3 represents the structural role of a network modifier. It should be pointed out that all these Fe-containing species are in dynamic equilibrium with each other and also with the other associate species already employed for the system $\text{SiO}_2\text{--Al}_2\text{O}_3\text{--CaO--MgO--Na}_2\text{O--K}_2\text{O}$.

Table 4.4. The Fe-containing associate species and structural units

Structural role of $\text{Fe}^{2+}/\text{Fe}^{3+}$	Compounds	Associate species	Structural units
Network modifiers	FeO	Fe_2O_2	FeO
	Fe_2O_3	Fe_2O_3	FeO_{1.5}
	FeNa_2O_2	$\frac{2}{3}\cdot\text{FeNa}_2\text{O}_2$	FeNa₂O₂
	FeSiO_3	FeSiO_3	FeSiO₃
	Fe_2SiO_4	$\frac{2}{3}\cdot\text{Fe}_2\text{SiO}_4$	Fe₂SiO₄
	$\text{FeSi}_2\text{CaO}_6$	$\frac{1}{2}\cdot\text{FeSi}_2\text{CaO}_6$	Fe_{0.5}SiCa_{0.5}O₃
	$\text{FeSi}_2\text{MgO}_6$	$\frac{1}{2}\cdot\text{FeSi}_2\text{MgO}_6$	Fe_{0.5}SiMg_{0.5}O₃
	$\text{FeSiNa}_2\text{O}_4$	$\frac{1}{2}\cdot\text{FeSiNa}_2\text{O}_4$	FeSiNa₂O₄
Charge compensators for Al^{3+}	FeAl_2O_4	$\frac{2}{3}\cdot\text{FeAl}_2\text{O}_4$	Fe_{0.5}AlO₂
	$\text{Fe}_2\text{Si}_5\text{Al}_4\text{O}_{18}$	$\frac{2}{11}\cdot\text{Fe}_2\text{Si}_5\text{Al}_4\text{O}_{18}$	Fe_{0.4}SiAl_{0.8}O_{3.6}
Network formers	CaFe_2O_4	$\frac{2}{3}\cdot\text{CaFe}_2\text{O}_4$	Ca_{0.5}FeO₂
	MgFe_2O_4	$\frac{2}{3}\cdot\text{MgFe}_2\text{O}_4$	Mg_{0.5}FeO₂
	NaFeO_2	NaFeO_2	NaFeO₂
	KFeO_2	KFeO_2	KFeO₂

Since the redox reaction of Fe^{2+} and Fe^{3+} as well as their structural role are properly described, the viscosity of the $\text{FeO}/\text{Fe}_2\text{O}_3$ -containing systems can be described using the associate species distribution as well as a proper connectivity of the associate

species. In contrast to the Al^{3+} -based quasi-tetrahedra, Fe^{3+} -based quasi-tetrahedra are less stable and not generally bonded with SiO_2 tetrahedra. Based on this fact, the self- and inter-polymerization of the Fe^{3+} -based quasi-tetrahedra can be ignored. Among the Fe-containing associate species, only the associate species $\text{Fe}_2\text{Si}_5\text{Al}_4\text{O}_{18}$ has potential self- and inter-polymerization, in which Fe^{2+} is charge compensator for Al^{3+} . The viscosity contributed from the remaining associate species can be described in the framework of the ideal viscosity part. Therefore, the viscosity of the $\text{FeO}/\text{Fe}_2\text{O}_3$ -containing systems is described with Eq. (4.6), in which the $\ln \eta_{\text{excess}}$ term is replaced with Eq. (4.11).

4.2 Optimization procedure

An overview of the optimization procedure is presented in **Fig. 4.14**. The critical steps are to obtain reliable experimental data and then to optimize the model parameters.

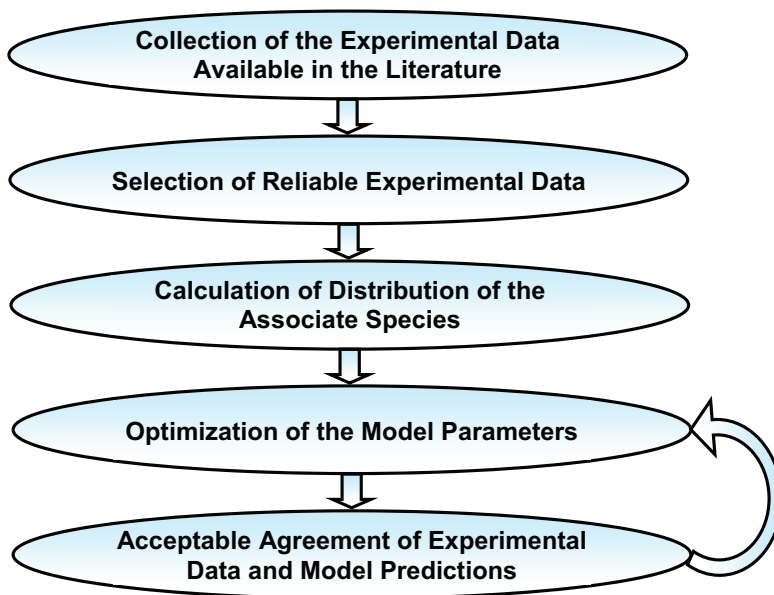


Fig. 4.14. Presentation of the model development process

For optimization of the model parameters, the first step is to collect the experimental data available in the literature. The existing experimental data used in this thesis are mainly from the SciGlass database [112], which contains more than 268000 oxide glasses and melts. For the system $\text{SiO}_2\text{--Al}_2\text{O}_3\text{--CaO--MgO--Na}_2\text{O--K}_2\text{O--FeO--Fe}_2\text{O}_3$, among the 254 subsystems 109 subsystems have experimental data available in the literature. As an example, the summary of experimental data for pure oxides and binary systems in the system $\text{SiO}_2\text{--Al}_2\text{O}_3\text{--CaO--MgO--Na}_2\text{O--K}_2\text{O}$ is listed in **Table 4.5**.

Table 4.5. Summary of experimental data used for pure oxides and binary systems in the system $\text{SiO}_2\text{--Al}_2\text{O}_3\text{--CaO--MgO--Na}_2\text{O--K}_2\text{O}$

System	No. of literature ^a	No. of total data	No. of reliable data ^b
SiO_2	64	1418	239
Al_2O_3	7	58	36
$\text{SiO}_2\text{--Al}_2\text{O}_3$	9	203	73
$\text{SiO}_2\text{--CaO}$	34	518	308
$\text{SiO}_2\text{--MgO}$	6	93	56
$\text{SiO}_2\text{--Na}_2\text{O}$	92	2264	688
$\text{SiO}_2\text{--K}_2\text{O}$	26	590	166
$\text{Al}_2\text{O}_3\text{--CaO}$	22	285	136

^aMostly extracted from SciGlass database

^bReferences in this thesis only refer to data used in the graphs.

The reliability of the existing experimental data should be paid considerable attention to. In general, the error sources of viscosity measurement at high temperature are described as the composition, temperature, atmosphere, phase, and measuring method. The molten slag, for example, is easily contaminated by crucible or sensor materials. In terms of its temperature, the results obtained by thermocouples have higher precision than those using optical pyrometers. The atmosphere during the measurement can seriously influence the oxidation state of transition metal elements, such as iron. The presence of solid phases can dramatically increase the viscosity of the slag. Moreover, the result is subjected to the measuring method itself, because of its own systematic error. In order to select reliable experimental data, the experimental data are carefully

analyzed and comprehensively compared with each other. The principles of this step are as follows:

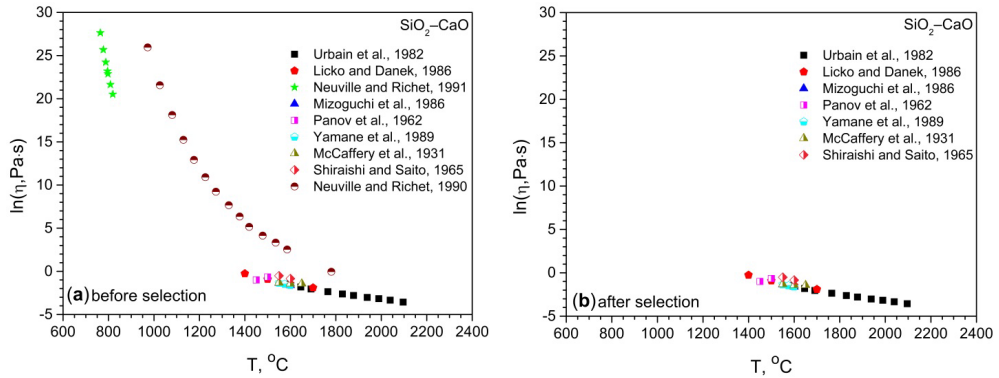


Fig. 4.15. Comparison of the experimental data before and after selection in the system $\text{SiO}_2\text{--CaO}$ at 0.50 mole fraction SiO_2

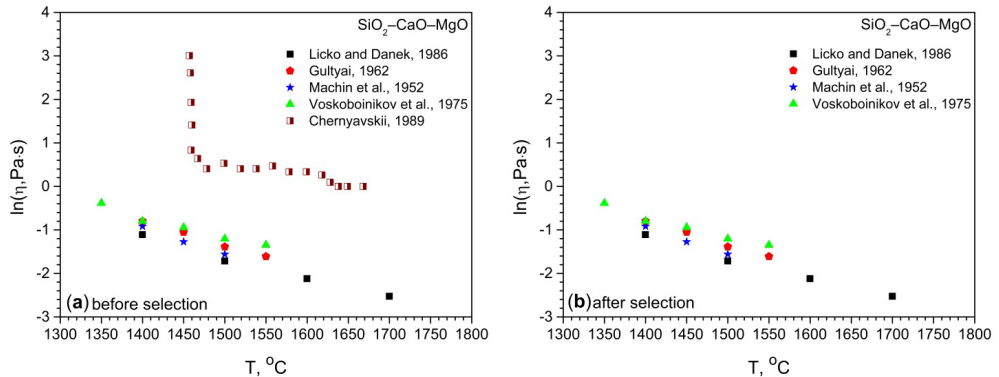


Fig. 4.16. Comparison of the experimental data before and after selection in the system $\text{SiO}_2\text{--CaO--MgO}$ at 0.40 mole fraction SiO_2 and 0.37 mole fraction CaO

- The experimental data of solid and liquid mixtures should be excluded firstly since the current model is designed for the fully liquid system. The thermodynamic database, developed by Yazhenskikh et al. [96–100], is employed to calculate the melting temperature.

- Comparisons of existing experimental data (such as viscosities [13, 113–124] for the systems $\text{SiO}_2\text{--CaO}$ and $\text{SiO}_2\text{--CaO--MgO}$) are performed by using a temperature-viscosity chart at identical composition, as shown in **Figs. 4.15** and **4.16**. The reliable experimental points are determined by two features: they have the same trend like lying on one line and they are given by at least two authors. Those experimental points with large deviation from the line are considered to be unreliable. Concerning the experimental points given by only one author, they are considered to be unverifiable.
- In addition, another principle should be pointed out. If one author offered both reliable and unreliable experimental data, all the experimental data from this author are excluded. If the unverifiable experimental data come from a trustable author, they would also be thought of as reliable experimental data.

The next step is to employ the ChemSheet module to calculate the concentration of associate species for the corresponding reliable experimental data, followed by optimization of model parameters, which is performed by Excel solver or Matlab solver. The average absolute value of difference between experimental data and model predictions is employed to be a criterion for judging the optimization performance. The ideal result is that average absolute values are equal to zero for all systems studied.

Due to the relative reliability and imbalance of experimental data, for example 2113 experimental data points for the system $\text{SiO}_2\text{--Al}_2\text{O}_3\text{--CaO}$ while only 36 for the system Al_2O_3 , the step by step optimization approach from lower order systems to higher order systems is not the best strategy for the current optimization. Since the viscosities of lower order systems, such as MgO , can be determined by way of extrapolation of corresponding higher order systems, such as $\text{SiO}_2\text{--MgO}$, $\text{Al}_2\text{O}_3\text{--MgO}$ or CaO--MgO , the influences of experimental data and extrapolation of other related systems on the optimization of model parameters are assumed to be equal. Therefore, a better strategy is to optimize model parameters at the same time for all related systems, which is implemented by ideal point approach, as explained as follows.

- To obtain ideal point for each system. Ideal points are the best fitting results, i.e. the smallest average absolute values f_i^0 that can be obtained by changing all related model parameters of the current model, which is given by

$$f_i^0 = \frac{1}{N} \cdot \sum_{j=1}^N |\ln \eta_{j,\text{cal}} - \ln \eta_{j,\text{exp}}| \quad (4.12)$$

where: subscript i represents slag system i; N is the number of reliable experimental points in each slag system and subscript j represents j-th experimental point; $\eta_{j,\text{cal}}$ is the calculated viscosity value; $\eta_{j,\text{exp}}$ is the experimental viscosity value.

- To construct the evaluation function, as shown in Eq. (4.13).

$$f(x) = \sqrt{\sum_{i=1}^N e_i \cdot (f_i(x) - f_i^0)^2} \quad (4.13)$$

where: x represents all model parameters (x here is a matrix); $f_i(x)$ is the expression of average absolute value for system i; e_i is the weighting factor depending on the amount of the reliable experimental data points.

- To minimize the evaluation function $f(x)$ to achieve the best fitting results.

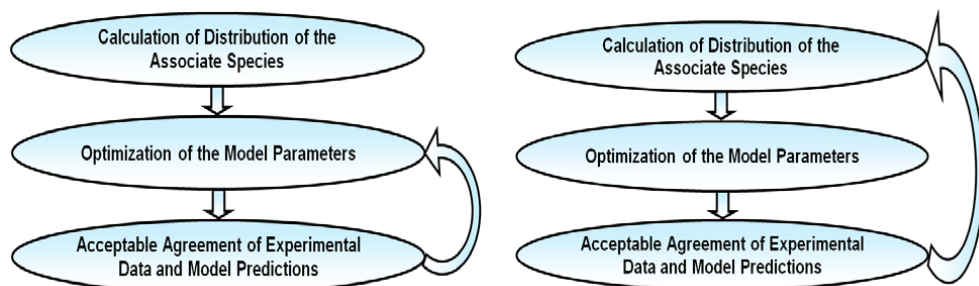
The step followed is to evaluate the model parameters optimized. If a satisfactory agreement between experimental data and model prediction is achieved, the optimization process will end. Otherwise, the optimization loop, as shown in **Fig. 4.14**, starts to work and will not stop until the best fitting results are obtained by the current model. During the optimization loop, sometimes the model parameters should be changed by hand since the evaluation function $f(x)$ in this case may be not global convergent and there exist local minima, and therefore the results obtained are possibly local minima. In addition, some boundary conditions such as the magnitude and sequence of the activation energy of viscous flow for model parameters are required.

For the FeO/Fe₂O₃-containing systems, the partial pressure of oxygen is required due to the redox reaction of FeO and Fe₂O₃, besides the composition and temperature. However, many experimental data from the SciGlass database are lacking clear partial pressure of oxygen, even without giving any information of it. In order to maximize the use of existing experimental data, some indirect information below is employed to estimate the partial pressure of oxygen.

- $\text{Fe}^{2+}/\Sigma \text{Fe}$
- $\text{Fe}^{3+}/\Sigma \text{Fe}$
- Reducing atmosphere
- Oxidizing atmosphere
- Neutral atmosphere

The ferrous-ferric ratio, which is obtained by Mössbauer spectra, is equal to the ratio of Fe²⁺- and Fe³⁺-based associate species in the melts, in which the change of ferrous-ferric ratio during the quenching process is ignored. Using the ferrous-ferric ratio, the partial pressure of oxygen can be reversely obtained. Concerning the reducing, oxidizing and neutral atmospheres, they are treated as variables. Then, a certain range of partial pressure of oxygen is set for each atmosphere during the optimization. By way of example, for the reducing and neutral atmospheres the partial pressure of oxygen is assumed to be limited in the range of 10⁻¹² and 10⁻⁶, whereas the partial pressure of oxygen is assumed to be within the range of 10⁻⁶ and 0.21 for the oxidizing atmosphere. With this boundary condition, the so called optimized partial pressure of oxygen is obtained. Furthermore, the partial pressure of oxygen controlled with CO/CO₂ is also handled by the same method.

Due to the fact that the partial pressure of oxygen is treated as a variable, the associate species distribution of a molten slag at a certain temperature is not constant any more. Therefore, the recalculation of the associate species distribution is required during the optimization process, as shown in **Fig. 4.17**. This modified optimization process is much more time consuming than the original one.



(a) constant partial pressure of oxygen

(b) variable partial pressure of oxygen

Fig. 4.17. The optimization process without and with the consideration of variable partial pressure of oxygen

5 Results and discussion

Based on the reliable experimental data, the model parameters for pure oxides and binary systems in the system $\text{SiO}_2\text{--Al}_2\text{O}_3\text{--CaO--MgO--Na}_2\text{O--K}_2\text{O}$ have been assessed, as listed in **Table 5.1**.

Table 5.1. Optimized model parameters as well as predicted theoretical viscosity and activation energy of viscous flow for pure oxides and binary systems

Structural unit i	Model parameters		Predicted theoretical viscosity and activation energy of viscous flow	
	A_i	B_i	$\eta_{T \rightarrow \infty}, \text{Pa}\cdot\text{s}$	$E_\eta, \text{kJ/mol}$
SiO_2	-11.8412	26.0077	7.20×10^{-6}	216
$(\text{SiO}_2)_6$	-7.4709	33.3646	2.48×10^{-4c}	308^c
$(\text{SiO}_2)_{109}$	-0.0002	9.8636	9.98×10^{-1d}	820^d
Al_2O_3	-7.9870	11.2921	3.40×10^{-4}	94
CaO	-12.2950	16.5938	4.57×10^{-6}	138
MgO	-12.3174	18.2211	4.47×10^{-6}	151
Na_2O	-10.1825	7.1809	3.78×10^{-5}	60
K_2O	-13.3501	10.1628	1.59×10^{-6}	84
$\text{Al}_6\text{Si}_2\text{O}_{13}$	-12.6651	36.4609	3.16×10^{-6}	303
CaSiO_3	-13.0951	21.0209	2.06×10^{-6}	175
Ca_2SiO_4	-11.2518	16.4112	1.30×10^{-5}	136
MgSiO_3	-15.1634	25.5891	2.60×10^{-7}	213
Mg_2SiO_4	-8.2317	11.2175	2.66×10^{-4}	93
Na_4SiO_4	-11.0638	10.7120	1.57×10^{-5}	89
Na_2SiO_3	-14.0539	18.0752	7.88×10^{-7}	150
$\text{Na}_2\text{Si}_2\text{O}_5$	-9.4354	18.0752	7.98×10^{-5}	150
K_2SiO_3	-10.3290	12.1253	3.27×10^{-5}	101
$\text{K}_2\text{Si}_2\text{O}_5$	-6.8797	19.5232	1.03×10^{-3}	162
$\text{K}_2\text{Si}_4\text{O}_9$	-12.0645	19.5232	5.76×10^{-6}	162
CaAl_2O_4	-14.5789	26.0077	4.66×10^{-7}	216
MgAl_2O_4	-14.5789	26.0077	4.66×10^{-7}	216
NaAlO_2	-12.0605	26.0077	5.78×10^{-6}	216
KAlO_2	-11.8412	26.0077	7.20×10^{-6}	216

^cThe equilibrium constant for the silica cluster $(\text{SiO}_2)_6$ is assumed to be 0.9.

^dThe equilibrium constant for the silica cluster $(\text{SiO}_2)_{109}$ is assumed to be 0.1.

It is noted that the model parameters of the pure oxides CaO, MgO, Na₂O, and K₂O needed to be assessed by way of extrapolation of corresponding binary systems, since there are no experimental data available in the literature resulting from the very high melting temperature of CaO and MgO respectively, as well as the very high reactivity of Na₂O and K₂O. Also, the model parameters of the binary systems Al₂O₃–MgO, Al₂O–Na₂O, and Al₂O₃–K₂O were assessed by the same methodology.

As **Table 5.1** indicates, each structural unit i has only one set of model parameters A_i and B_i , unlike the Hurst model requiring different sets of model parameters for different conditions. Very few model parameters are required for the current viscosity model, compared to the Quasi-chemical viscosity model. Moreover, the model parameters have a clear physico-chemical meaning. The model parameters A_i correspond to the theoretical viscosities when the temperature is approaching infinity, whereas the model parameters B_i are related to the activation energy for viscous flow. The theoretical viscosity (denoted with $\eta_{T \rightarrow \infty}$) as well as the activation energy for viscous flow, as listed in **Table 5.1**, are recalculated from the model parameters A_i and B_i . It is easy to understand that the values of model parameters A_i and B_i are negative and positive respectively and moreover, the values of model parameters B_i exhibit the same order of magnitude. In contrast, in the model of Kim et al. [79] the values of model parameters indicating the activation energy for viscous flow are not always positive and also of a very different order of magnitude.

It is seen from **Table 5.1**, that the values of model parameters B_i for SiO₂, CaAl₂O₄, MgAl₂O₄, NaAlO₂, and KAlO₂ are equal, which can be accepted because of their similar structure (quasi-tetrahedron) at the monomer-like scale. That is why the species CaAl₂O₄ and NaAlO₂ are assumed to have the same effect on the viscosity as the species SiO₂ in the model of Kim et al. [79]. However, in the current model the species SiO₂, CaAl₂O₄, MgAl₂O₄, NaAlO₂, and KAlO₂ have different viscosity contributions, which are displayed by the model parameters A_i according to the bond strength. Another aspect should be pointed out that the model parameters B_i for SiO₂, (SiO₂)₆ and (SiO₂)₁₀₉ cannot be directly compared. The model parameter B_i for SiO₂ is indeed related to the activation energy, whereas the model parameters B_i for (SiO₂)₆ and

$(\text{SiO}_2)_{109}$ are related to the activation energy as well as the equilibrium constant K_{n_j} (see Eq. (4.8)). The value of the equilibrium constant K_{n_j} should be lower than 1 for the silica clusters $(\text{SiO}_2)_6$ and $(\text{SiO}_2)_{109}$, which implies that the corresponding activation energies could be greater than that of SiO_2 . For reasonably assumed values of $K_{n_1}=0.9$ and $K_{n_2}=0.1$, the activation energies for the silica clusters $(\text{SiO}_2)_6$ and $(\text{SiO}_2)_{109}$ are 308 kJ/mol and 820 kJ/mol respectively, which are greater than the activation energy of 216 kJ/mol for SiO_2 . The corresponding predicted theoretical viscosities follow the order: $(\text{SiO}_2)_{109} > (\text{SiO}_2)_6 > \text{SiO}_2$ when the temperature is approaching infinity.

Concerning the model parameters B_i for Na_2SiO_3 and $\text{Na}_2\text{Si}_2\text{O}_5$, the activation energy of the species $\text{Na}_2\text{Si}_2\text{O}_5$, in principle, should be larger than that of the species Na_2SiO_3 because of the higher degree of polymerization of the species $\text{Na}_2\text{Si}_2\text{O}_5$. However, they tend to be equal during the numerical optimization process, which can be accepted at the monomer-like scale. The same holds for $\text{K}_2\text{Si}_2\text{O}_5$ and $\text{K}_2\text{Si}_4\text{O}_9$.

Table 5.2. Optimized model parameters as well as predicted theoretical viscosity and activation energy of viscous flow for ternary or higher order systems^e

Structural unit i	Model parameters		Predicted theoretical viscosity and activation energy of viscous flow	
	A_i	B_i	$\eta_{T \rightarrow \infty}, \text{Pa}\cdot\text{s}$	$E_\eta, \text{kJ/mol}$
$\text{Na}_2\text{Si}_6\text{Ca}_3\text{O}_{16}$	-2.600	17.027	7.43×10^{-02}	141.56
K_2SiCaO_4	-3.000	11.000	4.98×10^{-02}	91.45
K_2SiMgO_4	-35.598	10.996	3.47×10^{-16}	91.42
$\text{K}_2\text{Si}_5\text{MgO}_{12}$	-2.675	20.756	6.89×10^{-02}	172.57
$\text{Ca}_3\text{Al}_{10}\text{Na}_4\text{O}_{20}$	-3.001	10.999	4.97×10^{-02}	91.45
$\text{CaSi}_2\text{Al}_2\text{O}_8$	-19.299	34.848	4.15×10^{-09}	289.73
$\text{Mg}_2\text{Si}_5\text{Al}_4\text{O}_{18}$	-15.123	31.382	2.70×10^{-07}	260.91
NaSiAlO_4	-3.209	10.967	4.04×10^{-02}	91.18
$\text{NaSi}_3\text{AlO}_8$	-6.569	11.456	1.40×10^{-03}	95.25
KSialO_4	-2.999	11.001	4.98×10^{-02}	91.46
KS_2AlO_6	-6.670	17.759	1.27×10^{-03}	147.65

^eThe model parameters for the self- and inter-polymerization are not included here.

The model parameters for ternary or higher order systems in the system $\text{SiO}_2\text{--Al}_2\text{O}_3\text{--CaO--MgO--Na}_2\text{O--K}_2\text{O}$ are also given, as listed in **Table 5.2**. More than 4500 experimental data are selected to assess the model parameters for the ternary associate species. Nevertheless, very few experimental data are given for some ternary systems such as $\text{SiO}_2\text{--CaO--K}_2\text{O}$ and $\text{SiO}_2\text{--MgO--K}_2\text{O}$, and even no experimental data are available for the ternary system $\text{Al}_2\text{O}_3\text{--CaO--Na}_2\text{O}$. In consequence, the model parameters for the ternary associate species such as K_2SiCaO_4 , K_2SiMgO_4 , $\text{K}_2\text{Si}_5\text{MgO}_{12}$, and $\text{Ca}_3\text{Al}_{10}\text{Na}_4\text{O}_{20}$ are assessed by way of extrapolation of the corresponding higher order systems. The model parameters introduced for the multicomponent systems have the same physico-chemical meaning as for the pure oxides and binary systems.

As **Table 5.2** shows, the values of the model parameters B_i for KSi_2AlO_6 and KSiAlO_4 follow the order: $\text{KSi}_2\text{AlO}_6 > \text{KSiAlO}_4$, which is reasonable from the view of the degree of polymerization. The same holds for $\text{NaSi}_3\text{AlO}_8$ and NaSiAlO_4 as well as for $\text{K}_2\text{Si}_5\text{MgO}_{12}$ and K_2SiMgO_4 . It is noted that the activation energy of the associate species $\text{CaSi}_2\text{Al}_2\text{O}_8$ is greater than that of the associate species $\text{Mg}_2\text{Si}_5\text{Al}_4\text{O}_{18}$, which could be caused by the fact that the associate species $\text{Mg}_2\text{Si}_5\text{Al}_4\text{O}_{18}$ is less stable than the associate species $\text{CaSi}_2\text{Al}_2\text{O}_8$ [125]. It should be pointed out that the influence of the associate species K_2SiCaO_4 and $\text{Ca}_3\text{Al}_{10}\text{Na}_4\text{O}_{20}$ on the viscosity is small, and thereby the corresponding model parameters A_i and B_i seem to be not changed during the optimization process.

For $\text{FeO/Fe}_2\text{O}_3$ -containing systems, the model parameters are still being assessed, whose values are currently listed in Appendix. Nevertheless, the first results of viscosity are also presented in this section.

To demonstrate the performance of the current viscosity model, below for the representative systems the calculated viscosities are compared to the experimental data. Moreover, the viscosity extrapolated to the range below the melting temperature is presented with dotted lines and the liquid immiscibility in the systems such as $\text{SiO}_2\text{--CaO}$ and $\text{SiO}_2\text{--MgO}$ is marked with dashed lines.

5.1 Pure oxides

Due to no composition dependence of viscosity for the pure oxides, the viscosity of pure oxides can be calculated with the Arrhenius model, as shown in Eq. (4.2). The monomeric associate species are capable of describing the temperature-induced structural change for the pure oxides Al_2O_3 , CaO , MgO , Na_2O , and K_2O , whereas the temperature-induced structural change for the SiO_2 is described with the coexisting monomeric associate species SiO_2 and two common critical silica clusters.

5.1.1 SiO_2

Many experimental data of molten silica have been reported, due to its technological importance for high temperature processes including liquid phases. As **Fig. 5.1** shows, the experimental data [13, 126–130] are reproduced very well with the current viscosity model and the viscosity decreases with increasing temperature.

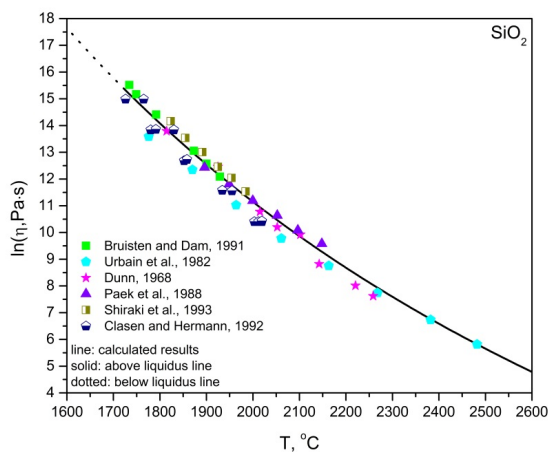


Fig. 5.1. Comparison between experimental data and calculated data for SiO_2

It can be seen that the viscosity of molten pure silica is very high. For example, the viscosity is above 300 Pa·s even at 2500°C and the viscosity can reach up to more than 5 million Pa·s when the temperature falls down to the melting temperature. A possible

reason for this very high viscosity is the silica network structure. Although the silica network structure collapses due to very high temperature, more than one structural unit still coexists [131]. This structural feature can be reflected by the coexisting monomeric associate species SiO_2 and two common critical silica clusters in the current viscosity model. Hereby, these two common critical silica clusters are obtained by fitting experimental data of both pure molten silica and all SiO_2 -based binary systems. As shown in **Table 5.1**, one of the critical silica clusters corresponds to a 6-membered, 3-dimensionally structural unit, which is consistent with most experimental and theoretical structural data [132]. The number of silica tetrahedra of the other critical silica cluster is 109, which has not direct experimental support but nevertheless has the same order of magnitude of that employed in the molecular dynamics simulation [133].

5.1.2 Al_2O_3

Compared to pure silica, the amount of existing experimental data of molten alumina is very small due to its high melting temperature. The experimental data given by Elyutin et al. [134], Urbain [135], and Zubarev et al. [136] are compared with the calculated data, as shown in **Fig. 5.2**.

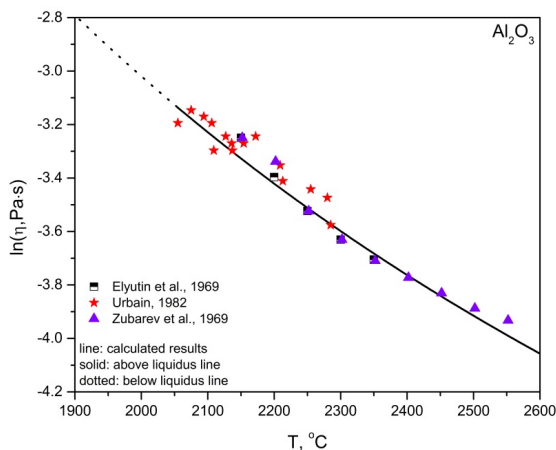


Fig. 5.2. Comparison between experimental data and calculated data for Al_2O_3

Although Elyutin et al. and Urbain used a rotational viscometer to measure the viscosity and Zubarev et al. employed the fiber elongation method, their experimental data can be reproduced within the experimental error with the current viscosity model. For the molten alumina, only one monomeric associate species Al_2O_3 is required to represent the structure of molten alumina. The model parameter B of the monomeric associate species Al_2O_3 can be recalculated to the activation energy for viscous flow, whose value of 94 kJ/mol is close to the value of 110 kJ/mol reported by Urbain [135].

5.1.3 CaO, MgO, Na_2O , and K_2O

The viscosities of pure oxides CaO, MgO, Na_2O , and K_2O are predicted, in which the model parameters are assessed by way of extrapolation of corresponding binary systems. Using the assessed model parameters, the temperature-induced viscosity behaviors, as shown in **Fig. 5.3**, are reasonable from the view of the bond strength between cations and oxygen ions. In general, a stronger bond strength results in a higher viscosity [65]. The bond strength for these oxides follows the order: $\text{SiO}_2 > \text{Al}_2\text{O}_3 > \text{MgO} > \text{CaO} > \text{Na}_2\text{O} > \text{K}_2\text{O}$, which is consistent with the viscosity order indicated in **Fig. 5.3**.

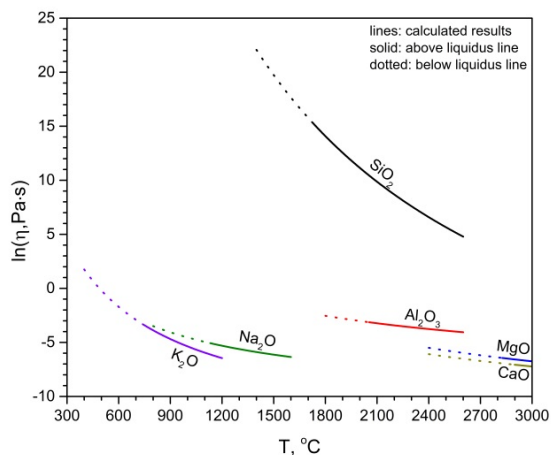


Fig. 5.3. Viscosities of the pure oxides SiO_2 , Al_2O_3 , CaO, MgO, Na_2O , and K_2O

5.2 Binary systems

In the SiO_2 -based binary systems, a challenging viscosity behavior is described by Avramov et al. [74] as the so called lubricant effect, in which the network modifiers play the role of lubricants allowing silica clusters to glide more easily with each other. Thus, the viscosity of molten silica drastically decreases when a small amount of network modifiers, such as Al_2O_3 , CaO , MgO , Na_2O , and K_2O , is added into the pure silica melt. To describe the lubricant effect, the composition-induced structural change is taken into account. In the current viscosity model, such structural change can be described by the monomeric associate species and two common critical silica clusters. Based on the effective description of the slag structure, the viscosity of the SiO_2 -based binary systems can be described by Eq. (4.6). Moreover, the viscosity extension from SiO_2 -based binary systems to the pure SiO_2 works very well, unlike the Zhang-Jahanshahi model [65], in which the viscosity values extrapolated from SiO_2 -based binary systems to the pure SiO_2 are different.

5.2.1 SiO_2 - Al_2O_3 and Al_2O_3 - CaO

Based on three monomeric associate species SiO_2 , Al_2O_3 , and $\text{Al}_6\text{Si}_2\text{O}_{13}$ and two common critical silica clusters $(\text{SiO}_2)_6$ and $(\text{SiO}_2)_{109}$, the experimental data [13, 110, 128, 134] of the binary system SiO_2 - Al_2O_3 can be reproduced very well for temperatures from 1800°C to 2200°C , as shown in **Fig. 5.4**. The viscosity values extrapolated from the binary system SiO_2 - Al_2O_3 to the pure oxides SiO_2 and Al_2O_3 also work well. Moreover, the lubricant effect can be predicted very well. It is noted that only 3 mol% Al_2O_3 , at 1800°C , lead to a decrease of the viscosity from ca. $1.3 \times 10^6 \text{ Pa}\cdot\text{s}$ to ca. $4.6 \times 10^3 \text{ Pa}\cdot\text{s}$.

Without introduction of the two common critical silica clusters as mentioned above, the lubricant effect cannot be described, as shown in **Fig. 5.5**. The red double-headed arrows indicate the difference in viscosity calculated with the original Arrhenius model and the current model. In the original Arrhenius model the magnitude of the viscosity extrapolated from the binary system SiO_2 - Al_2O_3 to the pure oxide SiO_2 is much smaller

than that of pure oxide SiO_2 . This indicates that the variation of viscosity is not linear to the concentration of the associate species SiO_2 .

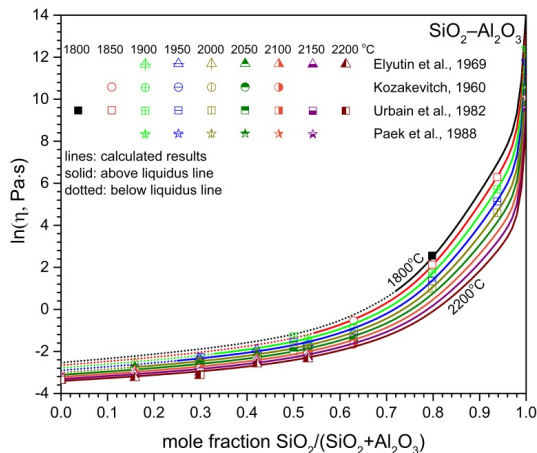


Fig. 5.4. Comparison between experimental data and calculated data in the system $\text{SiO}_2\text{--Al}_2\text{O}_3$

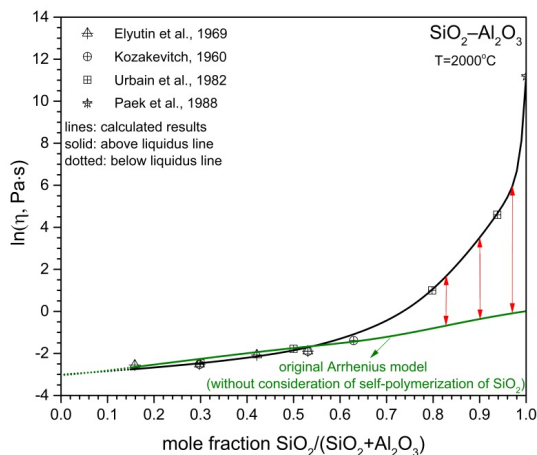


Fig. 5.5. The effect of self-polymerization of SiO_2 on viscosity

In the binary system $\text{SiO}_2\text{--Al}_2\text{O}_3$, Al_2O_3 behaves as a network modifier, whereas it can play the role of a network former in the binary systems $\text{Al}_2\text{O}_3\text{--CaO}$. **Fig. 5.6** indicates that the viscosity maxima occur somewhere in the middle, because of the amphoteric or charge compensation effect. This effect can be successfully described using the monomeric associate species CaAl_2O_4 , in which Al^{3+} associates with Ca^{2+} . A monomeric associate species CaAl_2O_4 behaves like a monomeric associate species SiO_2 . The corresponding activation energy of the monomeric associate species CaAl_2O_4 is the same as that of the monomeric associate species SiO_2 , as given in **Table 5.1**.

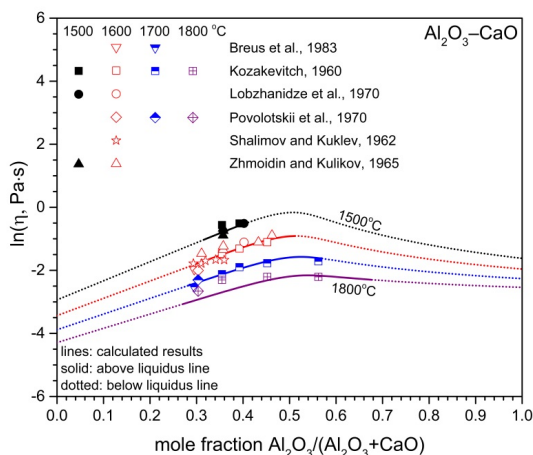


Fig. 5.6. Comparison between experimental data and calculated data in the system $\text{Al}_2\text{O}_3\text{--CaO}$

The experimental data [109–111, 137–139] presented in **Fig. 5.6** are fitted well with the current viscosity model. It can be seen that the peak of the viscosity maximum is slightly shifted towards the Al_2O_3 -rich side with increasing temperature. The viscosity maximum is more pronounced when the temperature decreases. That means that the amphoteric or charge compensation effect tends to be weak with increasing temperature. Moreover, the nearer to the fully charge compensated composition, the larger spacing of the viscosity isotherms.

5.2.2 $\text{Al}_2\text{O}_3\text{--MgO}$, $\text{Al}_2\text{O}_3\text{--Na}_2\text{O}$, and $\text{Al}_2\text{O}_3\text{--K}_2\text{O}$

Similar to the system $\text{Al}_2\text{O}_3\text{--CaO}$, the binary systems $\text{Al}_2\text{O}_3\text{--MgO}$, $\text{Al}_2\text{O}_3\text{--Na}_2\text{O}$, and $\text{Al}_2\text{O}_3\text{--K}_2\text{O}$ also have the amphoteric or charge compensation effect, which is described with the monomeric associate species MgAl_2O_4 , NaAlO_2 , and KAlO_2 , respectively.

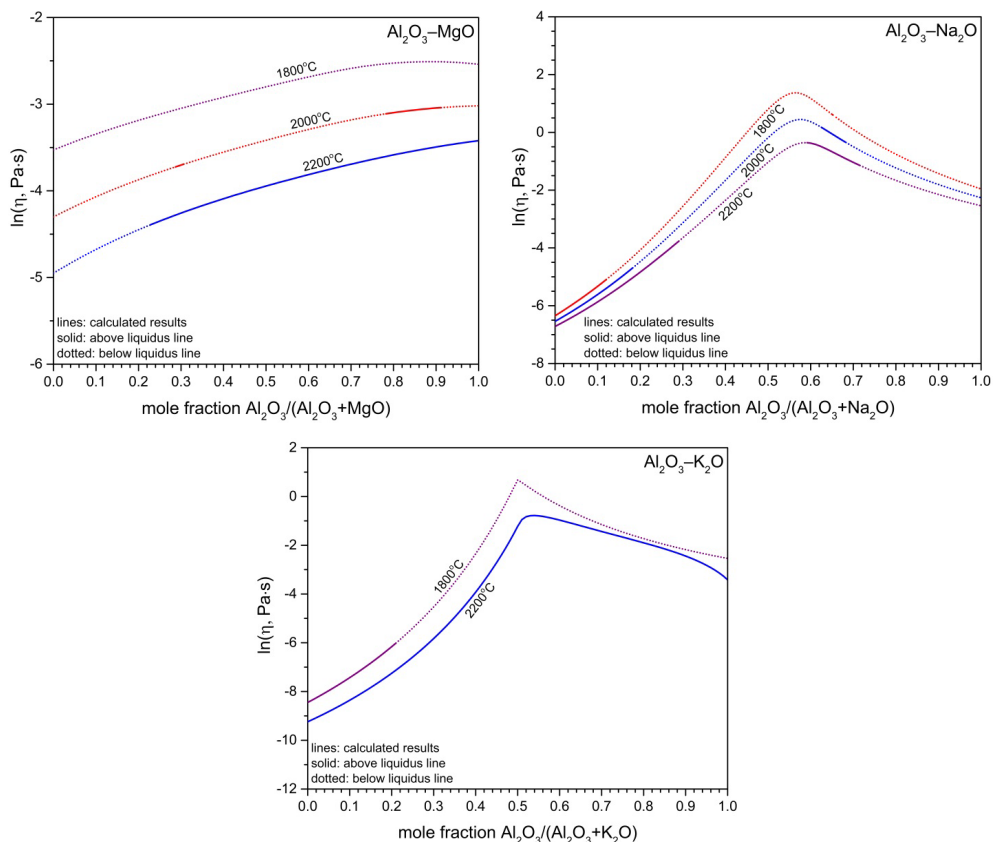


Fig. 5.7. Charge compensation effect in the systems $\text{Al}_2\text{O}_3\text{--MgO}$, $\text{Al}_2\text{O}_3\text{--Na}_2\text{O}$, and $\text{Al}_2\text{O}_3\text{--K}_2\text{O}$

Due to the different coulombic forces between the cations and oxygen anions, the charge compensation effect induced viscosity behavior varies, as shown in **Fig. 5.7**. It is pointed out that in the binary system $\text{Al}_2\text{O}_3\text{--K}_2\text{O}$ a smooth viscosity behavior around the fully charge compensated composition is transformed into a wedge-shaped behavior when the temperature is lowered from 2200°C to 1800°C. On the one hand, the unusual

wedge-shaped behavior is reasonable in the framework of the current model. As seen from **Fig. 5.8**, the concentration of the species KAlO_2 is almost 1 at the fully charge compensated composition. This indicates that at the temperature of 1800°C the system $\text{Al}_2\text{O}_3\text{--K}_2\text{O}$ almost consists of quasi-tetrahedra KAlO_2 , and therefore the viscosity sharply decreases when the mole fraction $\text{Al}_2\text{O}_3/(\text{Al}_2\text{O}_3+\text{K}_2\text{O})$ is approaching 0 or 1 from 0.5, which is similar to the lubricant effect demonstrated in the SiO_2 -based binary systems. On the other hand, an unusual (also wedge-shaped) distribution of the associate KAlO_2 is found at 1800°C , whereas the distribution of the associate NaAlO_2 is normal at the same temperature. It is noted that the distribution of the associate NaAlO_2 can also be a wedged shape when the temperature is lower than 700°C . This indicates that the shape of the distribution of the associate NaAlO_2 is dependent on temperature. The same is true for the associate KAlO_2 .

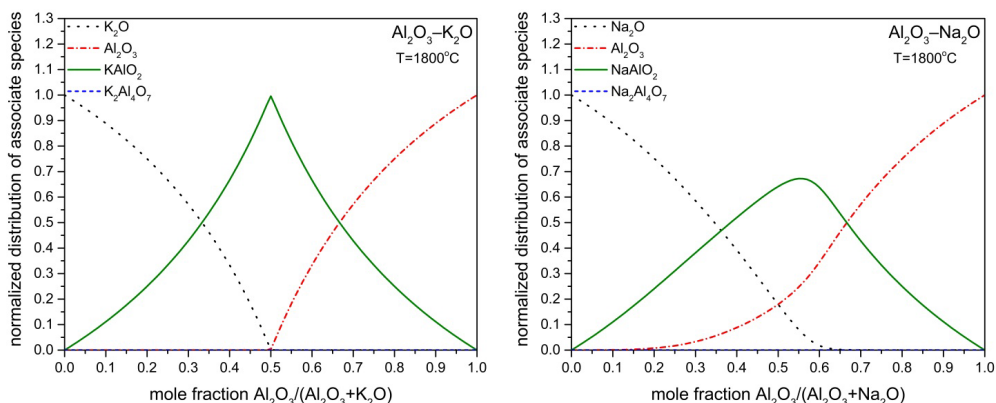


Fig. 5.8. Normalized distribution of associate species in the systems $\text{Al}_2\text{O}_3\text{--K}_2\text{O}$ and $\text{Al}_2\text{O}_3\text{--Na}_2\text{O}$

5.2.3 $\text{SiO}_2\text{--CaO}$ and $\text{SiO}_2\text{--MgO}$

Unlike Al_2O_3 , CaO and MgO always behave as network modifiers, which break the covalent bonds between silicon ions and oxygen ions and lead to a decrease in viscosity. In the binary system $\text{SiO}_2\text{--CaO}$, the CaO -induced rupture of the covalent bonds between silicon ions and oxygen ions can be described with the monomeric

associate species CaSiO_3 and Ca_2SiO_4 , and therefore the induced decrease of the viscosity can be described with the current viscosity model. **Fig. 5.9** shows that the calculated data are in good agreement with the experimental data [13, 110, 113, 115, 128, 140–144] within the experimental errors, at temperatures from 1500°C to 1900°C. It is noted that the viscosity prediction in the liquid immiscibility is marked with dashed lines, although the viscosity behavior in this range is assumed to be the same as that of a homogenous liquid phase. Moreover, the lubricant effect can be predicted for this system.

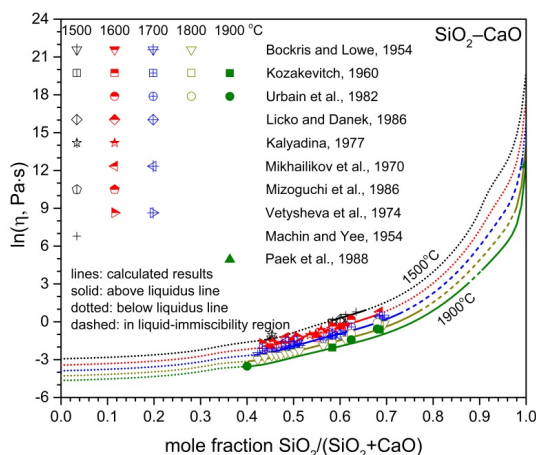


Fig. 5.9. Comparison between experimental data and calculated data in the system $\text{SiO}_2\text{--CaO}$

In terms of the binary system $\text{SiO}_2\text{--MgO}$, the experimental data [13, 28, 113, 145] are also reproduced well with the current viscosity model, as shown in **Fig. 5.10**. To describe the MgO -induced structural change, the monomeric associate species MgSiO_3 and Mg_2SiO_4 are employed, which are the same type of the monomeric associate species used in the binary system $\text{SiO}_2\text{--CaO}$.

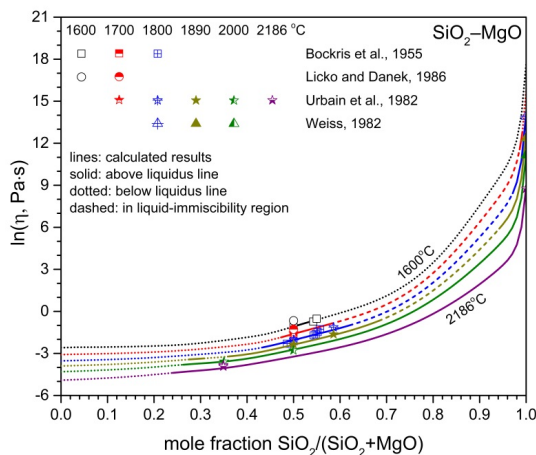


Fig. 5.10. Comparison between experimental data and calculated data in the system $\text{SiO}_2\text{--MgO}$

5.2.4 $\text{SiO}_2\text{--Na}_2\text{O}$ and $\text{SiO}_2\text{--K}_2\text{O}$

The viscosities of the systems containing Na_2O and K_2O are more complex, compared to the systems $\text{SiO}_2\text{--Al}_2\text{O}_3$, $\text{SiO}_2\text{--CaO}$, and $\text{SiO}_2\text{--MgO}$. As **Fig. 5.11** shows, the viscosity dramatically decreases when small amounts of alkali oxides are added to silica because of the lubricant effect. Then, it further gradually decreases until somewhere in the middle, followed by another strong decrease of the viscosity, the so called weak lubricant effect, due to the possible ring structures [79]. The Na_2O -induced structural change can be presented with the monomeric associate species Na_4SiO_4 , Na_2SiO_3 , and $\text{Na}_2\text{Si}_2\text{O}_5$. As a result, the experimental data [115, 146–156] are reproduced very well with the current viscosity model.

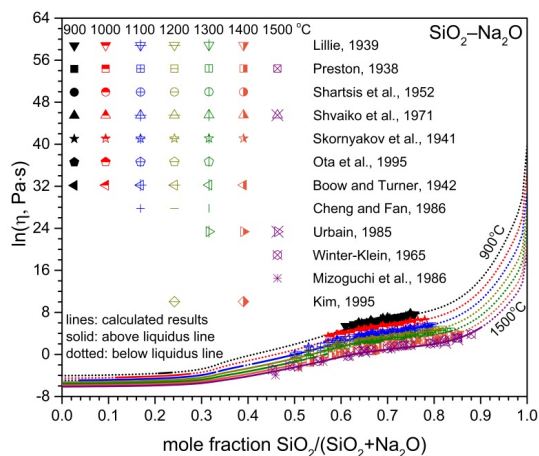


Fig. 5.11. Comparison between experimental data and calculated data in the system $\text{SiO}_2\text{--Na}_2\text{O}$

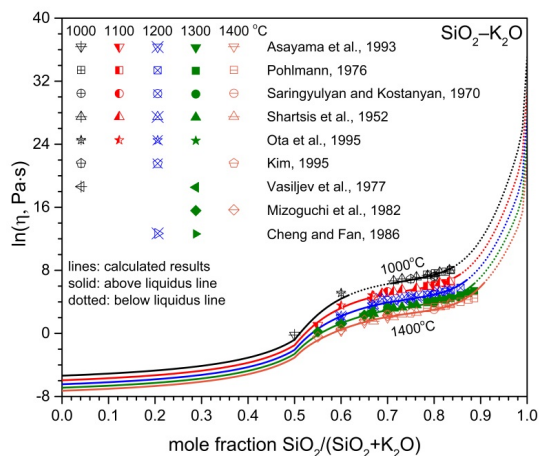


Fig. 5.12. Comparison between experimental data and calculated data in the system $\text{SiO}_2\text{--K}_2\text{O}$

The viscosity behavior of the binary system $\text{SiO}_2\text{--K}_2\text{O}$ is similar to that of the binary system $\text{SiO}_2\text{--Na}_2\text{O}$, as given in **Fig. 5.12**. The monomeric associate species K_2SiO_3 , $\text{K}_2\text{Si}_2\text{O}_5$, and $\text{K}_2\text{Si}_4\text{O}_9$, employed for describing the K_2O -induced structural change, however, are not exactly the same type as that in the system $\text{SiO}_2\text{--Na}_2\text{O}$. Using these monomeric associate species, the calculated data are in good agreement with the experimental data [148, 151, 153, 154, 157–161] at different temperatures from 1000°C to 1400°C .

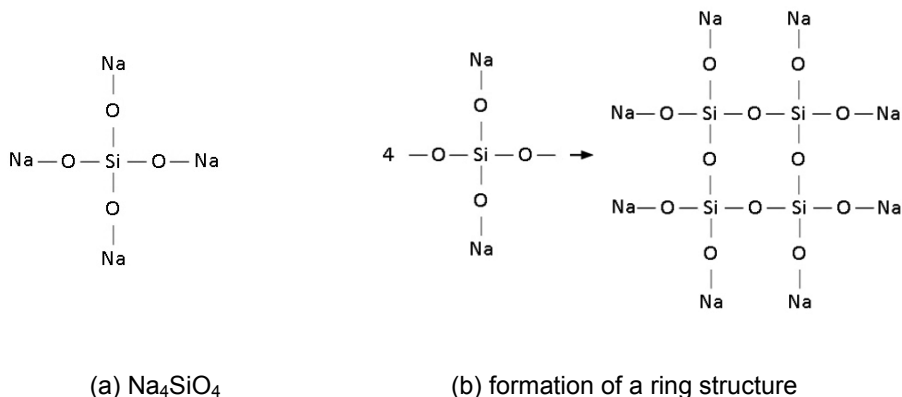


Fig. 5.13. Formation of ring structure for the monomeric associate species

It is noted that the so called weak lubricant effect of the system $\text{SiO}_2\text{--K}_2\text{O}$ is stronger than that of the system $\text{SiO}_2\text{--Na}_2\text{O}$. This possibly results from the monomeric associate species Na_4SiO_4 behaving as a network modifier, like Na_2O , which has no possibility to polymerize, to further form a larger structural unit, as shown in **Fig. 5.13(a)**. The other types of the monomeric associate species employed for describing Na_2O - and K_2O -induced structural change can possibly further form ring structures, such as the monomeric associate species Na_2SiO_3 , as shown in **Fig. 5.13(b)**.

5.3 Multicomponent systems without Al_2O_3

The viscosity of the multicomponent systems without Al_2O_3 is described with the model developed for the pure oxides and binary systems, in which four ternary associate species $\text{Na}_2\text{Si}_6\text{Ca}_3\text{O}_{16}$, K_2SiCaO_4 , K_2SiMgO_4 , and $\text{K}_2\text{Si}_5\text{MgO}_{12}$ are employed to describe

the structural changes induced by the different network modifiers. Four representative systems $\text{SiO}_2\text{--CaO--MgO}$, $\text{SiO}_2\text{--CaO--Na}_2\text{O}$, $\text{SiO}_2\text{--Na}_2\text{O--K}_2\text{O}$, and $\text{SiO}_2\text{--CaO--MgO--Na}_2\text{O--K}_2\text{O}$ are presented in this section. The influences of the network modifiers CaO, MgO, Na_2O , and K_2O on the viscosity are compared. The viscosity behavior when substituting one network modifier for another at constant temperatures or for constant SiO_2 contents is described. Moreover, the viscosities extrapolated from lower order systems to corresponding higher order systems are compared to the experimental data.

5.3.1 $\text{SiO}_2\text{--CaO--MgO}$

For the system $\text{SiO}_2\text{--CaO--MgO}$, no ternary associate species are employed and instead the composition-induced structural change is effectively described by relying on the monomeric associate species that are employed for the pure oxides and binary systems. As a result, the calculated viscosities agree well with the experimental data [13, 28, 113, 121, 123, 140, 141, 162–164], as shown in **Fig. 5.14**.

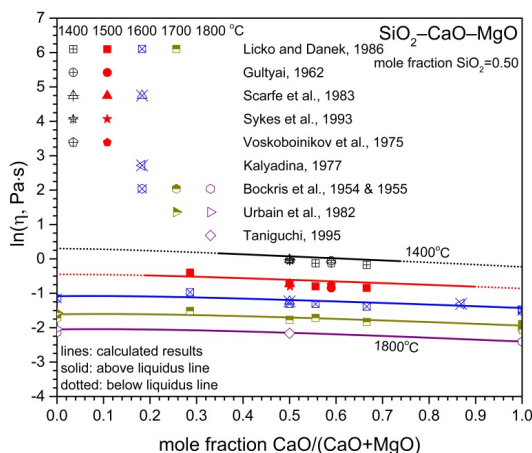


Fig. 5.14. Comparison between experimental data and calculated data in the system $\text{SiO}_2\text{--CaO--MgO}$ at 1400°C, 1500°C, 1600°C, 1700°C, and 1800°C for the SiO_2 content of 0.50 mole fraction

It is noted that the substitution of CaO for MgO for a constant SiO_2 content of 0.5 mole fraction causes a gradual decrease in viscosity at temperatures from 1400°C to 1800°C . This indicates that CaO has a greater ability to decrease the viscosity than MgO in the system $\text{SiO}_2\text{--CaO--MgO}$ because of the weaker bond strength of CaO. In contrast, in the Urbain model the network modifiers CaO and MgO are assumed to have the same effect on the viscosity [54]. The different effects of CaO and MgO on the viscosity are also presented in **Fig. 5.15**. At a constant temperature of 1600°C , the viscosity gradually decreases when substituting CaO for MgO for different SiO_2 contents ranging from 0.30 mole fraction to 0.70.

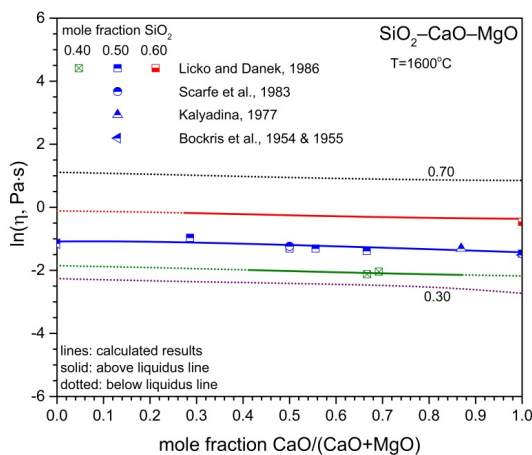


Fig. 5.15. Comparison between experimental data and calculated data in the system $\text{SiO}_2\text{--CaO--MgO}$ at 1600°C for the SiO_2 contents of 0.30, 0.40, 0.50, 0.60, and 0.70 mole fraction

In addition, it is demonstrated that the extension of viscosities from the binary systems $\text{SiO}_2\text{--CaO}$ and $\text{SiO}_2\text{--MgO}$ to the ternary system $\text{SiO}_2\text{--CaO--MgO}$ works well, which implies that the current model is a self-consistent model. In contrast, in the Zhang-Jahanshahi model the extrapolated viscosities involve self-conflicting values [65].

5.3.2 $\text{SiO}_2\text{--CaO--Na}_2\text{O}$

For the description of the composition-induced structural change in the system $\text{SiO}_2\text{--CaO--Na}_2\text{O}$, the ternary associate species $\text{Na}_2\text{Si}_6\text{Ca}_3\text{O}_{16}$ is employed besides the monomeric associate species for the pure oxides and binary systems. **Fig. 5.16** presents that the calculated viscosities are in good agreement with the experimental data given by Shvaiko et al. [165], Washburn et al. [166], Cheng and Fan [153], and Kim [154]. For a constant SiO_2 content of 0.75 mole fraction, the viscosity increases when replacing Na_2O with CaO at temperatures from 1100°C to 1400°C . It is noted that the alkali oxide Na_2O results in a sharper decrease in viscosity than alkaline earth oxides CaO and MgO , which is caused by the lower bond strength of Na_2O .

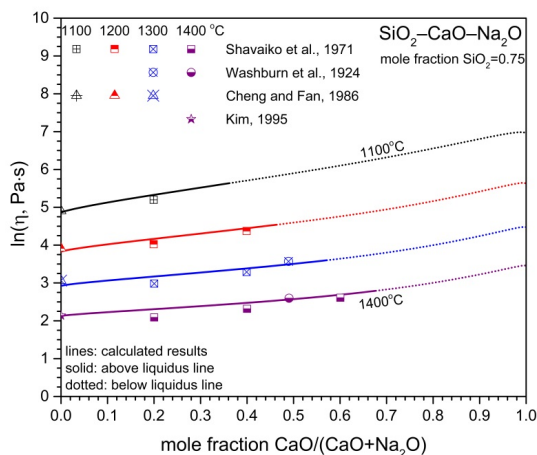


Fig. 5.16. Comparison between experimental data and calculated data in the system $\text{SiO}_2\text{--CaO--Na}_2\text{O}$ at 1100°C , 1200°C , 1300°C , and 1400°C for the SiO_2 content of 0.75 mole fraction

At a constant temperature of 1300°C , the substitution of CaO for Na_2O leads to a gradual increase in viscosity for different SiO_2 contents from 0.30 mole fraction to 0.70, as shown in **Fig. 5.17**. With the current model the calculated viscosities satisfactorily fit with the experimental data [166–170]. It is noted that the slope of the viscosity-

composition curves obviously varies for different SiO_2 contents in the system SiO_2 – CaO – Na_2O , which is not that case in the system SiO_2 – CaO – MgO . This implies that with the change of the SiO_2 content, the magnitude of the viscosity change differs between systems containing the alkaline earth oxides and systems containing alkali oxides.

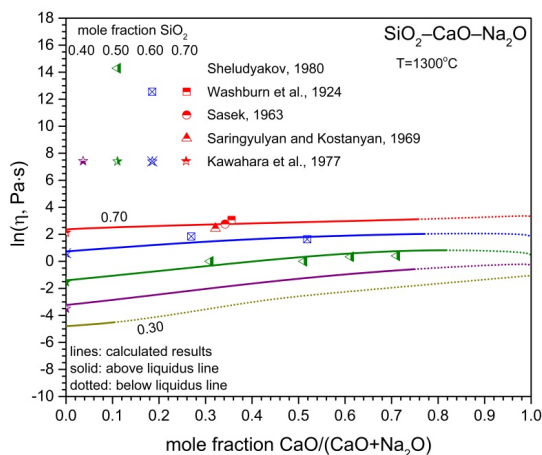


Fig. 5.17. Comparison between experimental data and calculated data in the system SiO_2 – CaO – Na_2O at 1300°C for the SiO_2 contents of 0.30, 0.40, 0.50, 0.60, and 0.70 mole fraction

5.3.3 SiO_2 – Na_2O – K_2O

In contrast to the ternary system SiO_2 – CaO – Na_2O , no ternary associate species for the ternary system SiO_2 – Na_2O – K_2O are used to describe the composition-induced structural change, which is effectively described with the monomeric associate species employed for the pure oxides and binary systems. The alkali oxide K_2O plays a similar structural role for viscosity as Na_2O , which also decreases the viscosity more dramatically than the alkaline earth oxides CaO and MgO . According to the order of the bond strength ($\text{Na}_2\text{O} > \text{K}_2\text{O}$), the viscosity should follow the order: SiO_2 – $\text{Na}_2\text{O} > \text{SiO}_2$ – K_2O . Nevertheless, the substitution of Na_2O for K_2O does not always lead to an

increase in viscosity, which could be caused by the formation of the ring structures as described for the systems $\text{SiO}_2\text{--Na}_2\text{O}$ and $\text{SiO}_2\text{--K}_2\text{O}$.

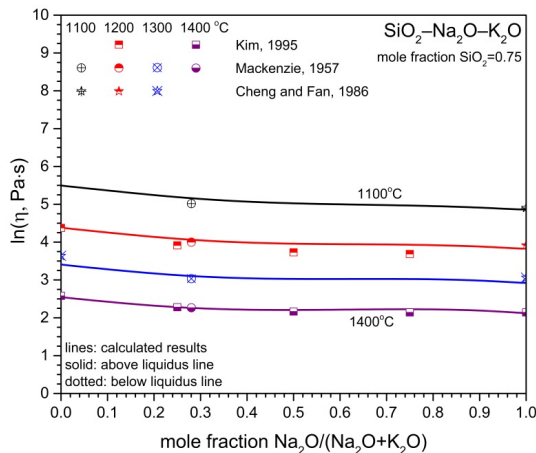


Fig. 5.18. Comparison between experimental data and calculated data in the system $\text{SiO}_2\text{--Na}_2\text{O--K}_2\text{O}$ at 1100°C, 1200°C, 1300°C, and 1400°C for the SiO_2 content of 0.75 mole fraction

As **Fig. 5.18** shows, the viscosity decreases when replacing K_2O with Na_2O for a constant SiO_2 content of 0.75 mole fraction at temperatures from 1100°C to 1400°C. It is noted that a good performance is given for the extension of viscosities from the binary systems $\text{SiO}_2\text{--Na}_2\text{O}$ and $\text{SiO}_2\text{--K}_2\text{O}$ to the ternary system $\text{SiO}_2\text{--Na}_2\text{O--K}_2\text{O}$, in which the experimental data [153, 154, 171] are well reproduced.

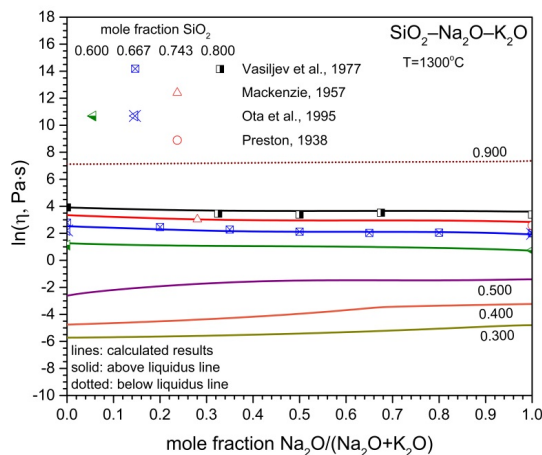


Fig. 5.19. Comparison between experimental data and calculated data in the system $\text{SiO}_2\text{--Na}_2\text{O--K}_2\text{O}$ at 1300°C for the SiO_2 contents of 0.300, 0.400, 0.500, 0.600, 0.667, 0.743, 0.800, and 0.900 mole fraction

As seen from **Fig. 5.19**, the trend of the viscosity with respect to mole fraction $\text{Na}_2\text{O}/(\text{Na}_2\text{O}+\text{K}_2\text{O})$ varies for different SiO_2 contents from 0.3 mole fraction to 0.9 at a constant temperature of 1300°C . The slope of the viscosity-composition curves shifts from positive to negative when the SiO_2 content is lowered from 0.9 mole fraction to 0.8, or from negative to positive when the SiO_2 content is lowered from 0.6 mole fraction to 0.5. This implies that the K_2O -induced ring structures have higher degrees of polymerization than those induced by Na_2O for the SiO_2 contents from 0.6 mole fraction to 0.8, which thereby results in a higher contribution of the viscosity for K_2O . With the current model, the experimental data [147, 151, 160, 171] in the same range of the SiO_2 contents (see **Fig. 5.19**) are well reproduced.

5.3.4 $\text{SiO}_2\text{--CaO--MgO--Na}_2\text{O--K}_2\text{O}$

When the model is extended to the quinary system $\text{SiO}_2\text{--CaO--MgO--Na}_2\text{O--K}_2\text{O}$, the combined effect of different oxides CaO , MgO , Na_2O , and K_2O on the viscosity is taken into account. To describe the structural change induced by these four oxides, four

ternary associate species $\text{Na}_2\text{Si}_6\text{Ca}_3\text{O}_{16}$, K_2SiCaO_4 , K_2SiMgO_4 , and $\text{K}_2\text{Si}_5\text{MgO}_{12}$ are employed. As shown in **Fig. 5.20**, the experimental data [172] are reproduced well with the current viscosity model, which indicates that the model parameters optimized for corresponding lower order systems are reasonable. It is noted that the viscosity decreases for all mass ratios $\text{Na}_2\text{O}/\text{K}_2\text{O}$ with increasing temperature. Moreover, the viscosity decreases with increasing mass ratio $\text{Na}_2\text{O}/\text{K}_2\text{O}$ at the same temperature, which is caused by two potential reasons. One is that the substitution of Na_2O for K_2O leads to a decrease in viscosity for the specific SiO_2 contents, which are defined in the system $\text{SiO}_2\text{--Na}_2\text{O--K}_2\text{O}$. Another reason is that the content of “free” SiO_2 , i.e. its mole fraction, is not constant but decreases with increasing mass ratio $\text{Na}_2\text{O}/\text{K}_2\text{O}$.

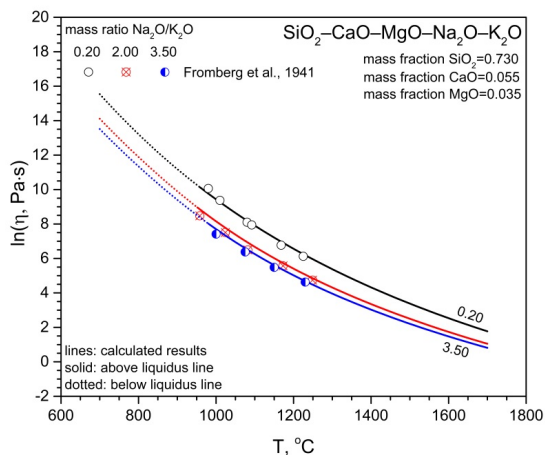


Fig. 5.20. Comparison between experimental data and calculated data in the system $\text{SiO}_2\text{--CaO--MgO--Na}_2\text{O--K}_2\text{O}$ for 0.730 mass fraction SiO_2 , 0.055 mass fraction CaO , 0.035 mass fraction MgO as well as 0.20, 2.00, and 3.50 mass ratio $\text{Na}_2\text{O}/\text{K}_2\text{O}$

5.4 Multicomponent systems with Al_2O_3

When Al_2O_3 is present, the effect of network modifiers CaO , MgO , Na_2O , and K_2O on the viscosity is different from that in the multicomponent system without Al_2O_3 due to the Al_2O_3 -induced amphoteric or charge compensation effect. For the description of the Al_2O_3 -induced structural change, seven Al^{3+} -containing ternary associate species $\text{CaSi}_2\text{Al}_2\text{O}_8$, $\text{Mg}_2\text{Si}_5\text{Al}_4\text{O}_{18}$, NaSiAlO_4 , KSiAlO_4 , $\text{NaSi}_3\text{AlO}_8$, KSi_2AlO_6 , and $\text{Ca}_3\text{Al}_{10}\text{Na}_4\text{O}_{20}$ are employed representing the structural changes caused by the different network modifiers. Eight representative systems $\text{SiO}_2\text{--Al}_2\text{O}_3\text{--CaO}$, $\text{SiO}_2\text{--Al}_2\text{O}_3\text{--MgO}$, $\text{SiO}_2\text{--Al}_2\text{O}_3\text{--Na}_2\text{O}$, $\text{SiO}_2\text{--Al}_2\text{O}_3\text{--K}_2\text{O}$, $\text{SiO}_2\text{--Al}_2\text{O}_3\text{--CaO--MgO}$, $\text{SiO}_2\text{--Al}_2\text{O}_3\text{--CaO--Na}_2\text{O}$, $\text{SiO}_2\text{--Al}_2\text{O}_3\text{--Na}_2\text{O--K}_2\text{O}$, and $\text{SiO}_2\text{--Al}_2\text{O}_3\text{--CaO--MgO--Na}_2\text{O--K}_2\text{O}$ are presented in this section. The effects of the different network modifiers CaO , MgO , Na_2O , and K_2O on the Al_2O_3 -induced viscosity maximum are compared. The position and magnitude of the viscosity maximum as a function of composition and temperature are predicted. Moreover, the viscosity behavior when replacing Al_2O_3 with SiO_2 for constant contents of the network modifiers is predicted and the viscosities extrapolated from lower order systems to corresponding higher order systems are compared to the experimental data.

5.4.1 $\text{SiO}_2\text{--Al}_2\text{O}_3\text{--CaO}$ and $\text{SiO}_2\text{--Al}_2\text{O}_3\text{--MgO}$

For the description of the composition-induced structural change in the system $\text{SiO}_2\text{--Al}_2\text{O}_3\text{--CaO}$, one ternary associate species $\text{CaSi}_2\text{Al}_2\text{O}_8$ is used besides the monomeric associate species for the pure oxides and binary systems, in which the associate species Al_2O_3 , $\text{Al}_6\text{Si}_2\text{O}_{13}$, CaAl_2O_4 , and $\text{CaSi}_2\text{Al}_2\text{O}_8$ are employed to describe the Al^{3+} -induced structural change. The associate species Al_2O_3 and $\text{Al}_6\text{Si}_2\text{O}_{13}$ behave as network modifiers, whereas the associate species CaAl_2O_4 and $\text{CaSi}_2\text{Al}_2\text{O}_8$ behave as network formers, which are employed to describe the amphoteric or charge compensation effect. As seen from **Fig. 5.21**, the viscosity maximum for the system $\text{SiO}_2\text{--Al}_2\text{O}_3\text{--CaO}$ is well described for a constant SiO_2 content of 0.5 mole fraction at temperatures from 1400°C to 2000°C . With the current model, the calculated viscosities are in good agreement with experimental data [13, 110, 121, 123, 173–176]. It is found that the position of the viscosity maximum is not exactly at the fully charge-

compensated composition but slightly shifted towards the Al_2O_3 -rich side with increasing temperature, which results from the corresponding shift in distribution of the associate species involved. Meanwhile, the viscosity maximum tends to be less pronounced due to lower stability of the Al^{3+} -based quasi-tetrahedral structures. Moreover, the larger spacing of viscosity isotherms occurs when approaching the fully charge-compensated composition, which was already observed by Grundy et al. [78].

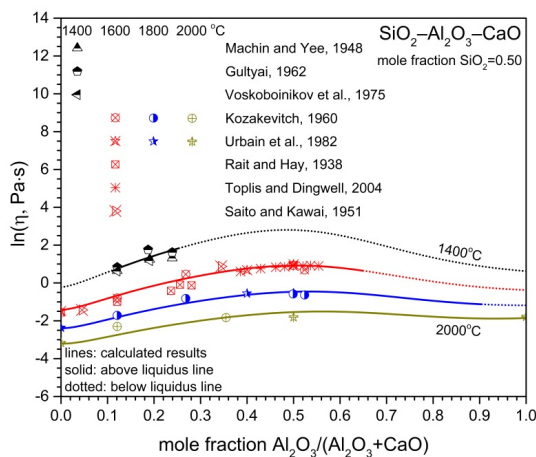


Fig. 5.21. Comparison between experimental data and calculated data in the system $\text{SiO}_2\text{--Al}_2\text{O}_3\text{--CaO}$ at 1400°C, 1600°C, 1800°C, and 2000°C for the SiO_2 content of 0.50 mole fraction

In addition to the temperature dependence, the Al_2O_3 -induced viscosity maximum is dependent on the SiO_2 content. As seen from **Fig. 5.22**, at a constant temperature of 1600°C, the position of the viscosity maximum varies for different SiO_2 contents from 0.40 mole fraction to 0.75. It is noted that the position of the viscosity maximum shifts towards the Al_2O_3 -rich side in the case of the SiO_2 content of 0.40 mole fraction. In contrast, the position of the viscosity maximum corresponds to the vicinity of the fully charge-compensated composition for the SiO_2 contents from 0.50 mole fraction to 0.75. Moreover, the viscosity maximum tends to be more pronounced when the SiO_2 content

increases from 0.4 mole fraction to 0.67. With the current model the calculated viscosities agree well with the experimental data [13, 110, 141, 142, 174–179].

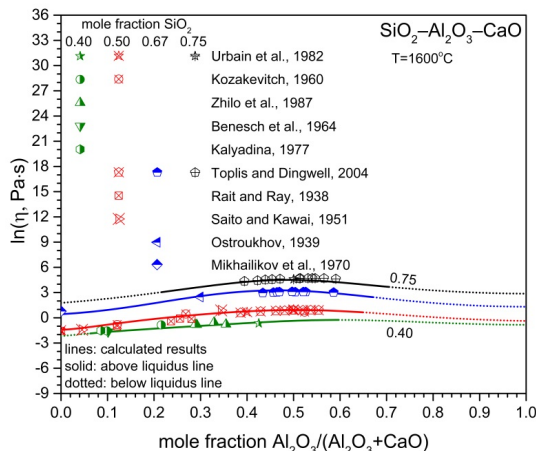


Fig. 5.22. Comparison between experimental data and calculated data in the system $\text{SiO}_2\text{--Al}_2\text{O}_3\text{--CaO}$ at 1600°C for the SiO_2 contents of 0.40, 0.50, 0.67, and 0.75 mole fraction

The viscosity behavior at the fully charge-compensated composition was investigated by many researchers [13, 110, 118, 162, 175, 180, 181], as seen from **Fig. 5.23**, in which the experimental data are well reproduced. This indicates that the change in viscosity at the fully charge-compensated composition with respect to composition and temperature can be well described with the current model. In contrast, for the description of the Al_2O_3 -induced viscosity maximum additional fitting terms related to the Al_2O_3 and network modifiers are used for the Quasi-chemical viscosity model [76], whereas additional associates such as CaAl_2O_4 and NaAlO_2 are used for the model developed by Grundy et al. [78].

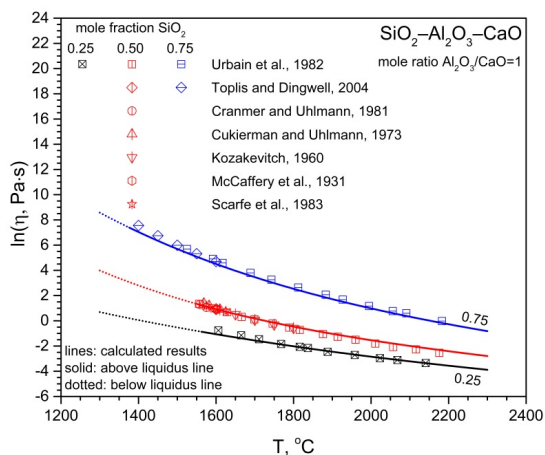


Fig. 5.23. Comparison between experimental data and calculated data in the system $\text{SiO}_2\text{-Al}_2\text{O}_3\text{-CaO}$ at 1 mole ratio $\text{Al}_2\text{O}_3/\text{CaO}$ for the SiO_2 contents of 0.25, 0.50, and 0.75 mole fraction

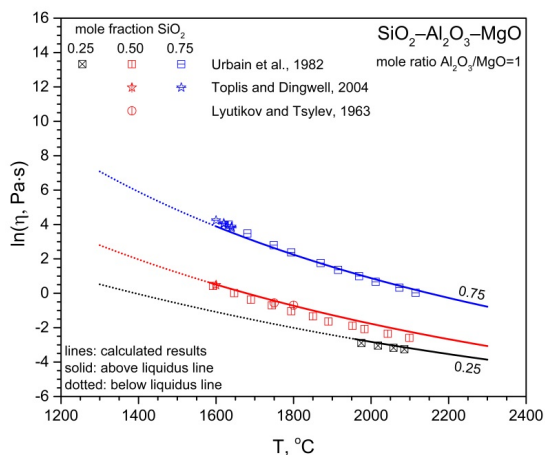


Fig. 5.24. Comparison between experimental data and calculated data in the system $\text{SiO}_2\text{-Al}_2\text{O}_3\text{-MgO}$ at 1 mole ratio $\text{Al}_2\text{O}_3/\text{MgO}$ for the SiO_2 contents of 0.25, 0.50, and 0.75 mole fraction

In contrast to the system $\text{SiO}_2\text{--Al}_2\text{O}_3\text{--CaO}$, the associate species MgAl_2O_4 and $\text{Mg}_2\text{Si}_5\text{Al}_4\text{O}_{18}$ are used to describe the Al^{3+} -induced charge compensation effect for the system $\text{SiO}_2\text{--Al}_2\text{O}_3\text{--MgO}$, in which the associate species MgAl_2O_4 is the same type of the associate species as CaAl_2O_4 , whereas the associate species $\text{Mg}_2\text{Si}_5\text{Al}_4\text{O}_{18}$ is different from the associate species $\text{CaSi}_2\text{Al}_2\text{O}_8$. This indicates that the structural change induced by the alkaline earth oxides CaO and MgO differs when they act as charge compensators for Al_2O_3 , which could explain the difference of the viscosity behavior in the systems $\text{SiO}_2\text{--Al}_2\text{O}_3\text{--CaO}$ and $\text{SiO}_2\text{--Al}_2\text{O}_3\text{--MgO}$. With the current model, as seen from **Fig. 5.24**, the viscosities [13, 175, 182] have been well predicted. It is noted that for the system $\text{SiO}_2\text{--Al}_2\text{O}_3\text{--MgO}$ the magnitude of the viscosity at the fully charge-compensated composition is smaller than that for the system $\text{SiO}_2\text{--Al}_2\text{O}_3\text{--CaO}$.

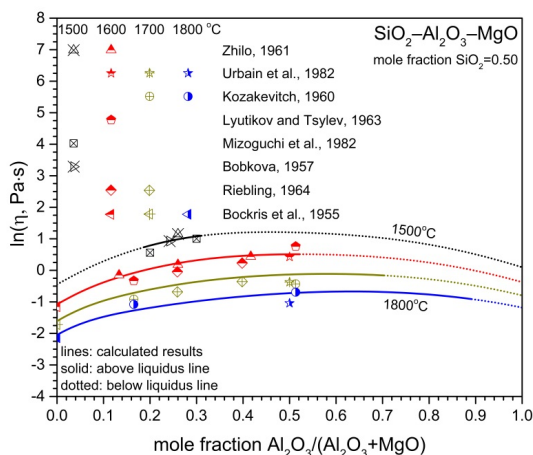


Fig. 5.25. Comparison between experimental data and calculated data in the system $\text{SiO}_2\text{--Al}_2\text{O}_3\text{--MgO}$ at 1500°C, 1600°C, 1700°C, and 1800°C for the SiO_2 content of 0.50 mole fraction

Nevertheless, for these two systems the influences of the temperature and SiO_2 content on the position of the viscosity maximum are similar. As **Fig. 5.25** shows, for a constant SiO_2 content of 0.5 mole fraction the viscosity maximum is slightly shifted towards the Al_2O_3 -rich side when the temperature is increased from 1500°C to 1800°C. **Fig. 5.26**

shows that at a constant temperature of 1600°C the viscosity maximum corresponds to the vicinity of the fully charge-compensated composition for different SiO_2 contents from 0.45 mole fraction to 0.75. The experimental data [13, 28, 110, 161, 175, 182–186] given in **Figs. 5.25** and **5.26** are well reproduced with the current model.

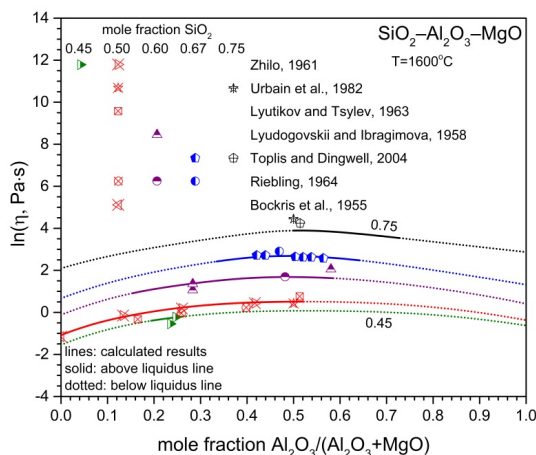


Fig. 5.26. Comparison between experimental data and calculated data in the system $\text{SiO}_2\text{--Al}_2\text{O}_3\text{--MgO}$ at 1600°C for the SiO_2 contents of 0.45, 0.50, 0.60, 0.67, and 0.75 mole fraction

5.4.2 $\text{SiO}_2\text{--Al}_2\text{O}_3\text{--Na}_2\text{O}$ and $\text{SiO}_2\text{--Al}_2\text{O}_3\text{--K}_2\text{O}$

In contrast to the alkaline earth aluminosilicate systems, the alkali aluminosilicate systems exhibit more complicated viscosity behavior. To describe the Al^{3+} -induced structural change in the system $\text{SiO}_2\text{--Al}_2\text{O}_3\text{--Na}_2\text{O}$, the associate species Al_2O_3 , $\text{Al}_6\text{Si}_2\text{O}_{13}$, $\text{Na}_2\text{Al}_4\text{O}_7$, NaAlO_2 , NaSiAlO_4 , and $\text{NaSi}_3\text{AlO}_8$ are employed, in which the associate species Al_2O_3 , $\text{Al}_6\text{Si}_2\text{O}_{13}$, and $\text{Na}_2\text{Al}_4\text{O}_7$ behave as network modifiers, whereas the associate species NaAlO_2 , NaSiAlO_4 , and $\text{NaSi}_3\text{AlO}_8$ play the role of network formers. As seen from **Fig. 5.27**, with the current model the experimental data [13, 187–191] are satisfactorily reproduced, although the experimental data involve

some deviations, especially for the viscosities at a constant SiO_2 content of 0.67 mole fraction. It is noted that the viscosity trend obviously varies on the Al_2O_3 -poor side for different SiO_2 contents, and moreover for constant SiO_2 contents the viscosity behavior markedly differs between the Al_2O_3 -poor side and the Al_2O_3 -rich side, which is similar to the behavior of the activation energy for viscous flow when substituting Al_2O_3 for Na_2O [187]. In contrast, such viscosity behavior is not covered by the model of Grundy et al. [78].

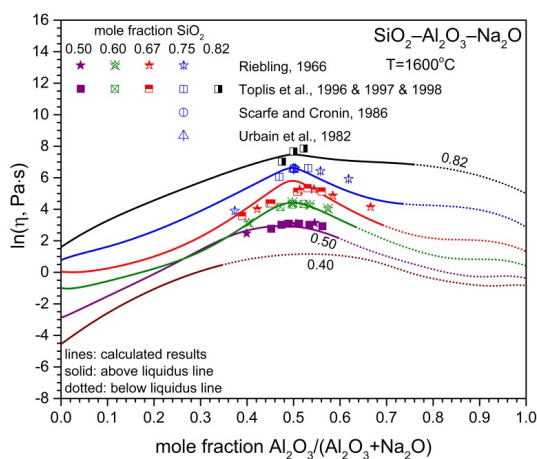


Fig. 5.27. Comparison between experimental data and calculated data in the system $\text{SiO}_2\text{--Al}_2\text{O}_3\text{--Na}_2\text{O}$ at 1600°C for the SiO_2 contents of 0.40, 0.50, 0.60, 0.67, 0.75, and 0.82 mole fraction

By relying on the distribution of the associate species involved, the Al_2O_3 -induced viscosity maximum is satisfactorily described, in which the predicted position of the viscosity maximum tends to correspond to the fully charge-compensated composition for different SiO_2 contents from 0.60 mole fraction to 0.82, whereas the viscosity maximum is shifted to the Al_2O_3 -poor side for the SiO_2 content of 0.50 mole fraction and to the Al_2O_3 -rich side for the SiO_2 content of 0.4 mole fraction, as shown in **Fig. 5.27**. It is noted that the experimental data given by Riebling et al. and Toplis et al. shows an obvious shift in position of the viscosity maximum towards the Al_2O_3 -rich side for the

SiO_2 content of 0.67 mole fraction, which should be caused by the presence of a tricluster species ($\text{AlSi}_2\text{O}_{5.5}$) [192]. When such tricluster species forms, a threefold coordinated oxygen arises, as demonstrated in **Fig. 5.28**.

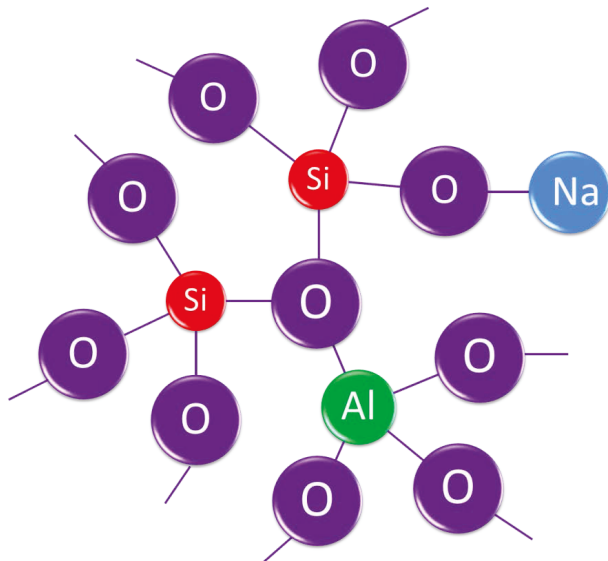


Fig. 5.28. Schematic presentation of a tricluster species $\text{AlSi}_2\text{O}_{5.5}$

In the current model the associate species NaAlO_2 , NaSiAlO_4 , and $\text{NaSi}_3\text{AlO}_8$ but not such tricluster species are employed to describe the viscosity maximum. More investigations concerning the associate species introduced for the system $\text{SiO}_2\text{--Al}_2\text{O}_3\text{--Na}_2\text{O}$ might be needed.

The temperature dependence of the viscosity maximum for the system $\text{SiO}_2\text{--Al}_2\text{O}_3\text{--Na}_2\text{O}$ is presented in **Fig. 5.29**. With the current model, the experimental data [146, 154, 187, 188, 191, 193] are satisfactorily predicted. It is noted that the position of the viscosity maximum remains constant when the temperature is changed from 1000°C to 1600°C for a constant SiO_2 content of 0.67 mole fraction. Moreover, the viscosity maximum is more pronounced when the temperature decreases, which is similar to the alkaline earth aluminosilicate systems.

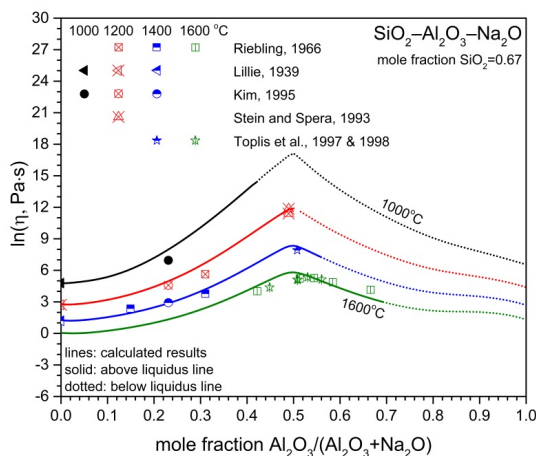


Fig. 5.29. Comparison between experimental data and calculated data in the system $\text{SiO}_2\text{--Al}_2\text{O}_3\text{--Na}_2\text{O}$ at 1000°C, 1200°C, 1400°C, and 1600°C for the SiO_2 content of 0.67 mole fraction

In addition, the viscosity behavior at the fully charge-compensated composition as a function of the SiO_2 content and temperature is presented in **Fig. 5.30**. The current model allows a good performance in reproducing experimental data [13, 120, 180, 187–189, 191, 193–195], although for the SiO_2 content of 0.67 mole fraction there is a small deviation at temperatures above 1400°C.

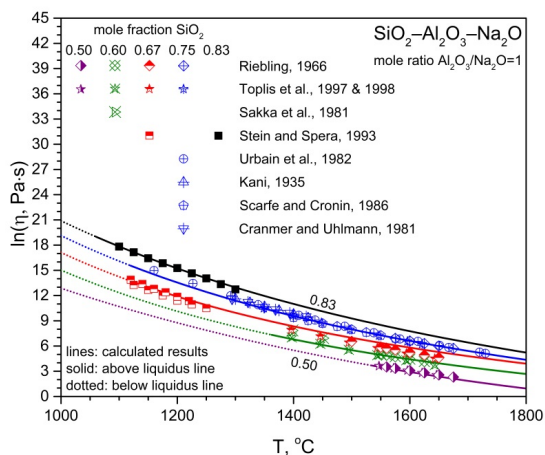


Fig. 5.30. Comparison between experimental data and calculated data in the system $\text{SiO}_2\text{-Al}_2\text{O}_3\text{-Na}_2\text{O}$ at 1 mole ratio $\text{Al}_2\text{O}_3/\text{Na}_2\text{O}$ for the SiO_2 contents of 0.50, 0.60, 0.67, 0.75, and 0.83 mole fraction

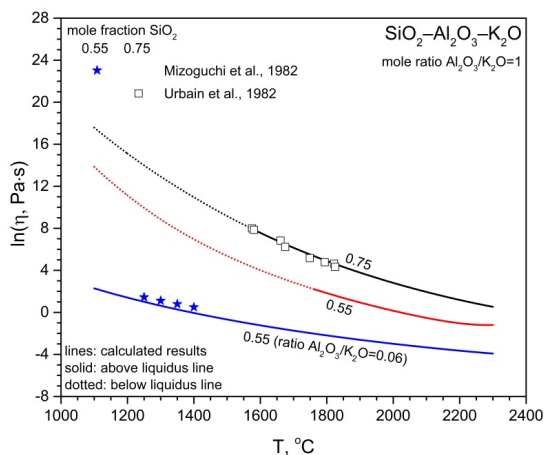


Fig. 5.31. Comparison between experimental data and calculated data in the system $\text{SiO}_2\text{-Al}_2\text{O}_3\text{-K}_2\text{O}$ at 1 (or 0.06) mole ratio $\text{Al}_2\text{O}_3/\text{K}_2\text{O}$ for the SiO_2 contents of 0.55 and 0.75 mole fraction

The associate species KSi_2AlO_6 in place of $\text{NaSi}_3\text{AlO}_8$ is employed to describe the Al^{3+} -induced structural change for the system $\text{SiO}_2\text{--Al}_2\text{O}_3\text{--K}_2\text{O}$, in which the remaining associate species are the same type of the associate species as employed for the system $\text{SiO}_2\text{--Al}_2\text{O}_3\text{--Na}_2\text{O}$. A limited amount of experimental data for the system $\text{SiO}_2\text{--Al}_2\text{O}_3\text{--K}_2\text{O}$ is available in the literature and the model parameters are assessed by the existing experimental data and also by way of extrapolation from the corresponding higher order systems. The current optimized model parameters allow a good agreement of the calculated viscosities and existing experimental data [13, 120, 161], and also a reasonable prediction of the viscosity in the range where no experimental data are available. As **Fig. 5.31** shows, at the fully charge-compensated composition, an increase in SiO_2 content leads to an increased viscosity at the same temperature, whereas at the same SiO_2 content of 0.55 mole fraction the magnitude of the viscosity at the fully charge-compensated composition is larger than that at mole ratio $\text{Al}_2\text{O}_3/\text{K}_2\text{O}$ of 0.06.

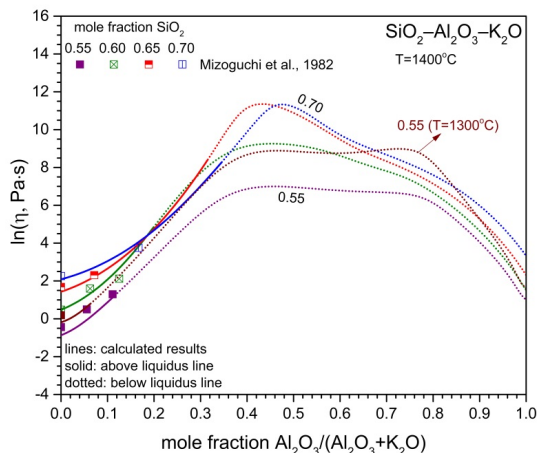


Fig. 5.32. Comparison between experimental data and calculated data in the system $\text{SiO}_2\text{--Al}_2\text{O}_3\text{--K}_2\text{O}$ at 1400°C (or 1300°C) for the SiO_2 contents of 0.55, 0.60, 0.65, and 0.70 mole fraction

Fig. 5.32 shows the dependence of the position of the viscosity maximum on temperature and composition for the system $\text{SiO}_2\text{--Al}_2\text{O}_3\text{--K}_2\text{O}$. In contrast to the system $\text{SiO}_2\text{--Al}_2\text{O}_3\text{--Na}_2\text{O}$, a viscosity behavior (a smooth stepped shape) on the Al_2O_3 -rich side is also presented. The position of the viscosity maximum is slightly shifted towards the Al_2O_3 -poor side and is dependent on the SiO_2 content. It is noted that on the Al_2O_3 -poor side the viscosity-composition curves for the SiO_2 contents from 0.60 mole fraction to 0.70 intersect with each other, which could result from the different ring structures that causes the weak lubricant effect in the system $\text{SiO}_2\text{--K}_2\text{O}$. This intersection is indicated by the experimental data given by Mizoguchi et al. [161], which are well reproduced with the current model. It is found that a local viscosity minimum occurs in the Al_2O_3 -rich side (near to the fully charge compensated composition) for the SiO_2 content of 0.55 mole fraction when the temperature is lowered to 1300°C . Such local viscosity minimum was observed by Toplis and Dingwell for the system $\text{SiO}_2\text{--Al}_2\text{O}_3\text{--CaO}$ [175].

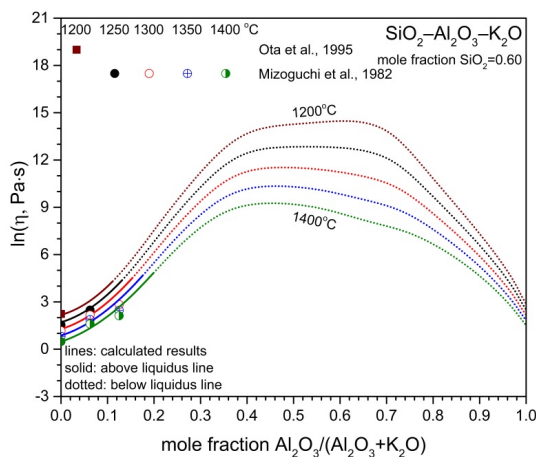


Fig. 5.33. Comparison between experimental data and calculated data in the system $\text{SiO}_2\text{--Al}_2\text{O}_3\text{--K}_2\text{O}$ at 1200°C , 1250°C , 1300°C , 1350°C , and 1400°C for the SiO_2 content of 0.60 mole fraction

For the system $\text{SiO}_2\text{--Al}_2\text{O}_3\text{--K}_2\text{O}$ the temperature dependence of the position of the viscosity maximum is presented in **Fig. 5.33**. At the temperatures above 1250°C , the

viscosity maximum is located in the Al_2O_3 -poor side for the constant SiO_2 content of 0.60 mole fraction, whereas a viscosity plateau tends to occur when the temperature is lowered to 1250°C . When the temperature is further lowered, the viscosity maximum is shifted towards the Al_2O_3 -rich side. It is obvious that more experimental data are needed to better assess the model parameters for alkali aluminosilicate systems.

5.4.3 SiO_2 – Al_2O_3 – CaO – MgO

For the system SiO_2 – Al_2O_3 – CaO – MgO , the viscosity is extrapolated from the corresponding lower order systems such as SiO_2 – Al_2O_3 – CaO and SiO_2 – CaO – MgO , in which no additional associate species as well as no additional model parameters are introduced.

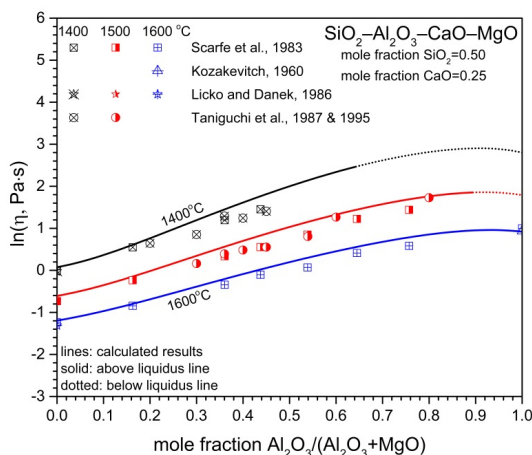


Fig. 5.34. Comparison between experimental data and calculated data in the system SiO_2 – Al_2O_3 – CaO – MgO at 1400°C , 1500°C , and 1600°C as well as 0.50 mole fraction SiO_2 and 0.25 mole fraction CaO

As shown in **Fig. 5.34**, the experimental data [110, 113, 162, 164, 196] are satisfactorily predicted, although a small deviation between the calculated data and the experimental data occurs. It is seen that the viscosity maximum does not occur at the ideal compositional position (mole fraction $\text{Al}_2\text{O}_3/(\text{Al}_2\text{O}_3+\text{MgO})=1$) and the position of the

viscosity maximum is shifted from 0.93 mole fraction to 0.91 mole fraction $\text{Al}_2\text{O}_3/(\text{Al}_2\text{O}_3+\text{MgO})$ when the temperature is lowered from 1600°C to 1400°C, which is reasonable due to the fact that not all Al^{3+} are charge-compensated by alkaline earth cations Ca^{2+} .

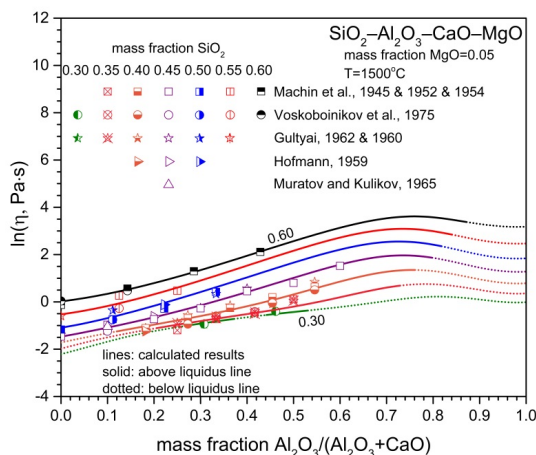


Fig. 5.35. Comparison between experimental data and calculated data in the system $\text{SiO}_2\text{--Al}_2\text{O}_3\text{--CaO--MgO}$ at 1500°C as well as 0.05 mass fraction MgO and 0.30, 0.35, 0.40, 0.45, 0.50, 0.55, and 0.60 mass fraction SiO_2

From **Fig. 5.35** it can be seen that with the current model the calculated values are in good agreement with the experimental data [121–123, 144, 197–200]. It is noted that the position of the viscosity maximum is dependent on the mass fraction of SiO_2 . The viscosity maximum is slightly shifted towards the left as the SiO_2 content is increased from 0.30 mass fraction to 0.50, whereas it is slightly shifted towards the right as the SiO_2 content is increased from 0.50 mass fraction to 0.60. Moreover, the viscosity maximum occurs at the Al_2O_3 -rich side.

5.4.4 $\text{SiO}_2\text{--Al}_2\text{O}_3\text{--CaO--Na}_2\text{O}$

By way of extrapolation from corresponding lower order systems, the viscosity of the system $\text{SiO}_2\text{--Al}_2\text{O}_3\text{--CaO--Na}_2\text{O}$ is predicted and the dependence of the viscosity on

composition and temperature is well described. As seen from **Fig. 5.36**, the calculated viscosities agree well with the experimental data [167, 180, 201–203]. It is noted that the viscosities of the four slags follow the order: slag 1 > slag 2 > slag 3 > slag 4, which is caused by the charge compensation effect. This order is consistent with the order of the sum of the SiO_2 and Al_2O_3 contents although the amount of the charge compensators for Al^{3+} might be not enough for slag 1.

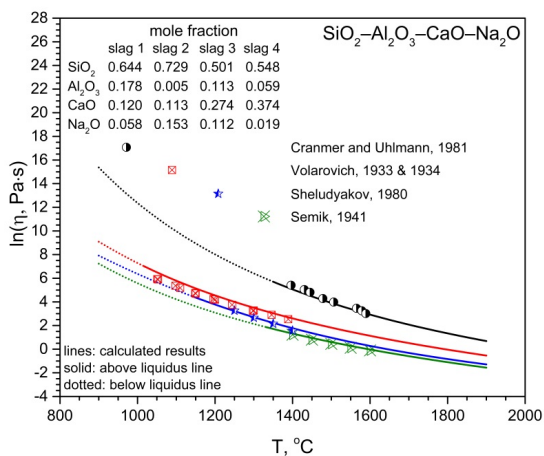


Fig. 5.36. Comparison between experimental data and calculated data in the system $\text{SiO}_2\text{--Al}_2\text{O}_3\text{--CaO--Na}_2\text{O}$ for the SiO_2 contents of 0.501, 0.548, 0.644, and 0.729 mole fraction

Fig. 5.37 shows the viscosity behavior when substituting SiO_2 for Al_2O_3 for the constant contents of CaO and Na_2O . The experimental data given by Pavlushkin et al. [204] are satisfactorily predicted. It is seen that the viscosity maximum occurs when Al_2O_3 is replaced with SiO_2 . The viscosity increases at the beginning by substituting SiO_2 for the excess Al_2O_3 that is not charge-compensated by CaO or Na_2O . Then further substitution of SiO_2 for Al_2O_3 leads to not only an increased concentration of SiO_2 itself but also an increased concentration of network modifiers that originally act as charge compensators for Al_2O_3 . As a result, the viscosity maximum occurs during the substitution of SiO_2 for Al_2O_3 . This kind of the viscosity maximum has been observed for other systems.

Riebling found that the substitution of Al_2O_3 for SiO_2 at a constant Na_2O content of 0.20 mole fraction leads to the presence of the viscosity maximum for the system $\text{Na}_2\text{O}-\text{Al}_2\text{O}_3-\text{SiO}_2$ [187], whereas the viscosity maximum occurs when replacing SiO_2 with Al_2O_3 at different CaO contents of 0.35, 0.40, and 0.45 mole fraction for the system $\text{CaO}-\text{Al}_2\text{O}_3-\text{SiO}_2$ [205].

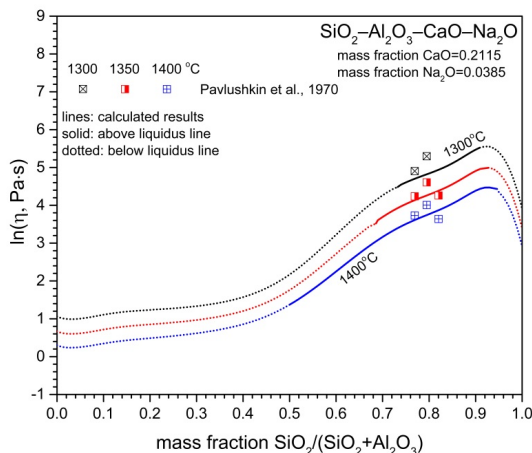


Fig. 5.37. Comparison between experimental data and calculated data in the system $\text{SiO}_2-\text{Al}_2\text{O}_3-\text{CaO}-\text{Na}_2\text{O}$ at 1300°C, 1350°C, and 1400°C as well as 0.2115 mass fraction CaO and 0.0385 mass fraction Na_2O

5.4.5 $\text{SiO}_2-\text{Al}_2\text{O}_3-\text{Na}_2\text{O}-\text{K}_2\text{O}$

Extending the viscosity calculations to the system $\text{SiO}_2-\text{Al}_2\text{O}_3-\text{Na}_2\text{O}-\text{K}_2\text{O}$ works well. As **Fig. 5.38** presents, the viscosity behavior at fully charge-compensated composition is well described. The viscosities of two slags [13, 206] are well predicted. It is noted that the viscosity of slag 6 is greater than that of slag 5 at the same temperature due to the fact that the slag 6 contains a higher content of SiO_2 and K_2O than slag 5, in which the Al^{3+} -induced quasi-tetrahedron is more stable when AlO_4^{5-} is charge-compensated by K^+ .

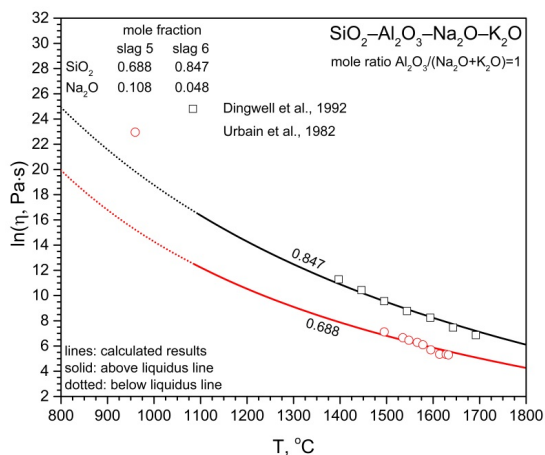


Fig. 5.38. Comparison between experimental data and calculated data in the system $\text{SiO}_2\text{--Al}_2\text{O}_3\text{--Na}_2\text{O--K}_2\text{O}$ at 1 mole ratio $\text{Al}_2\text{O}_3/(\text{Na}_2\text{O}+\text{K}_2\text{O})$ for the SiO_2 contents of 0.688 and 0.847 mole fraction

As shown in **Fig. 5.39**, when substituting SiO_2 for Al_2O_3 the viscosity maximum appears at different temperatures in the range from 1000 $^\circ\text{C}$ to 1400 $^\circ\text{C}$. The experimental data [154] are well reproduced. The position of the viscosity maximum occurs in the vicinity of the fully charge-compensated composition. This indicates that the substitution of SiO_2 for Al_2O_3 that behaves as a network former causes a decrease in viscosity. That is, the viscosity change resulting from an increased concentration of SiO_2 is smaller than that resulting from the corresponding decreased concentration of the Al^{3+} -based quasi-tetrahedra and increased concentration of network modifiers that originally act as charge compensators for Al_2O_3 . Comparing the positions of the viscosity maximum as shown in **Figs. 5.37** and **5.39** indicates that the viscosity contribution induced by the charge compensation effect differs depending on the charge compensators for Al_2O_3 .

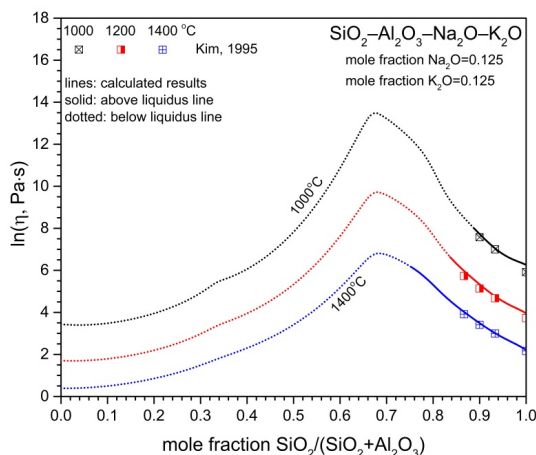


Fig. 5.39. Comparison between experimental data and calculated data in the system $\text{SiO}_2\text{--Al}_2\text{O}_3\text{--Na}_2\text{O--K}_2\text{O}$ at 1000°C, 1200°C, and 1400°C as well as 0.125 mole fraction Na_2O and 0.125 mole fraction K_2O

5.4.6 $\text{SiO}_2\text{--Al}_2\text{O}_3\text{--CaO--MgO--Na}_2\text{O--K}_2\text{O}$

When the model is extended to the system $\text{SiO}_2\text{--Al}_2\text{O}_3\text{--CaO--MgO--Na}_2\text{O--K}_2\text{O}$, the structural change induced by different oxides Al_2O_3 , CaO , MgO , Na_2O , and K_2O is described by the associate species employed for pure oxides, binary systems and ternary systems. By way of extrapolation from the corresponding subsystems, the viscosity of this senary system is well predicted by the current model. As **Fig. 5.40** shows, the current model allows a good performance in reproducing the experimental data [207–209].

It is seen that the viscosity of three slags follows the order: slag 9 > slag 7 > slag 8, which is reasonable when the charge compensation effect is taken into account. Although the sum of contents SiO_2 and Al_2O_3 differs little in slag 7 and in slag 8, the difference in viscosity is relatively large. It is noted that the excess network modifiers that are not required to compensate Al_2O_3 are alkaline earth oxides for the slag 7,

whereas the excess network modifiers for the slag 8 contain more than 50% of alkali oxides, due to the fact that the priority of the network modifiers to compensate Al_2O_3 follows the order: $\text{K}_2\text{O} > \text{Na}_2\text{O} > \text{CaO} > \text{MgO}$ [125, 210–212].

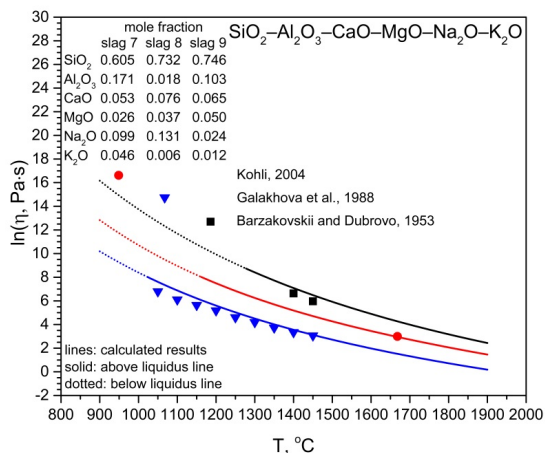


Fig. 5.40. Comparison between experimental data and calculated data in the system $\text{SiO}_2\text{--Al}_2\text{O}_3\text{--CaO--MgO--Na}_2\text{O--K}_2\text{O}$ for the SiO_2 contents of 0.605, 0.732, and 0.746 mole fraction

As **Fig. 5.41** shows, the substitution of SiO_2 for Al_2O_3 leads to varying viscosity maxima for different slags at 1300°C . The viscosities [208, 213] of the slag 10, slag 11, and slag 12 are satisfactorily reproduced. It is found that the substitution of CaO for Na_2O causes a right shift in position of the viscosity maximum at constant contents of MgO and K_2O . The same holds for the substitution of CaO for K_2O . Moreover, the substitution of CaO for Na_2O or K_2O results in a decrease in magnitude of the viscosity maximum. To present the viscosity behavior when substituting alkaline earth oxides for alkali oxides, the slag 13 and slag 14 are designed, which have the same mole ratio $\text{Na}_2\text{O}/\text{K}_2\text{O}$ and mole ratio CaO/MgO as the slag 10, respectively. It is noted that the order of the viscosities extrapolated to the system $\text{Al}_2\text{O}_3\text{--CaO--MgO--Na}_2\text{O--K}_2\text{O}$ or to the system $\text{SiO}_2\text{--CaO--MgO--Na}_2\text{O--K}_2\text{O}$ is reasonable, which indicates that the current model is self-consistent.

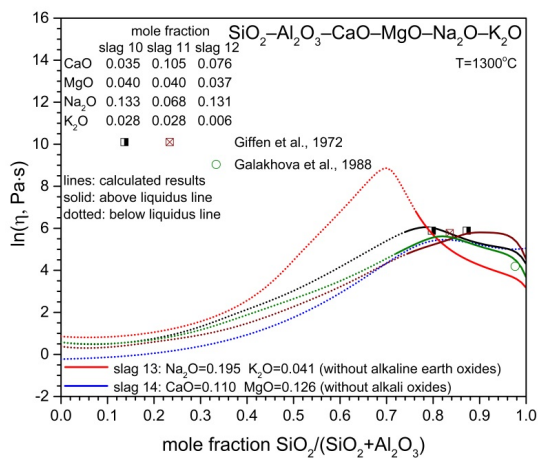


Fig. 5.41. Comparison between experimental data and calculated data in the system $\text{SiO}_2\text{--Al}_2\text{O}_3\text{--CaO--MgO--Na}_2\text{O--K}_2\text{O}$ at 1300°C

5.5 The FeO/Fe₂O₃-containing systems

The presence of FeO/Fe₂O₃ leads to a more complex viscosity behavior resulting from the redox reaction of Fe²⁺ and Fe³⁺ as well as the dual structural role. For description of the Fe²⁺/Fe³⁺-induced structural change in the system SiO₂–Al₂O₃–CaO–MgO–Na₂O–K₂O–FeO–Fe₂O₃, 14 Fe-containing associate species are employed, among which the associate species CaFe₂O₄, MgFe₂O₄, NaFeO₂, and KFeO₂ representing Fe³⁺-based quasi-tetrahedra behave as network formers. No ternary associate species are employed to describe the Fe³⁺-induced charge compensation effect. More than 1600 experimental data points are employed to assess the model parameters, and the viscosity in the investigated systems is properly described. The dependence of viscosity on partial pressure of oxygen makes it difficult to optimize all the model parameters. Not all the model parameters have been optimized so far. Nevertheless, the overall performance of the current model is good. The local viscosity maximum in the system SiO₂–FeO/Fe₂O₃ is discussed. The Fe³⁺-induced charge compensation effect is presented and is also compared to that induced by Al³⁺. Moreover, the viscosity behavior when replacing Fe₂O₃ with SiO₂ for constant contents of the other network modifiers is presented.

5.5.1 The overall performance of the FeO/Fe₂O₃-containing systems

The viscosity of the system SiO₂–Al₂O₃–CaO–FeO, which is of practical significance for the coal ashes, is used to demonstrate the performance of the current model in describing the viscosity of the FeO/Fe₂O₃-containing systems. Hurst et al. [61] modified the Urbain model to predict the viscosity of such system. It is found that different sets of model parameters are required for different contents of FeO, which results in many model parameters. **Figs. 5.42 and 5.43** show that a good agreement between the calculated viscosities and the experimental data [61, 62] is achieved with the current model using only one set of model parameters. Therefore, the current model gives a better performance than the Hurst model.

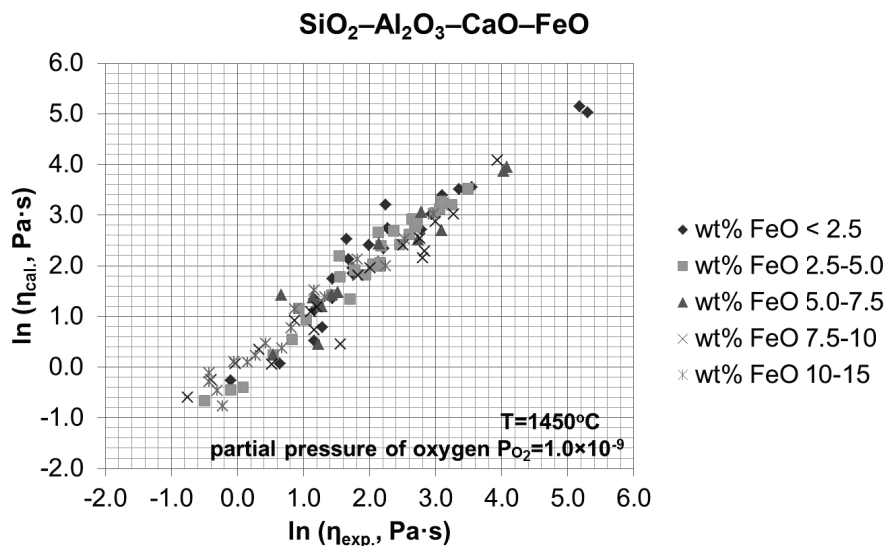


Fig. 5.42. Comparison between experimental data and calculated data in the system SiO₂–Al₂O₃–CaO–FeO at 1450°C

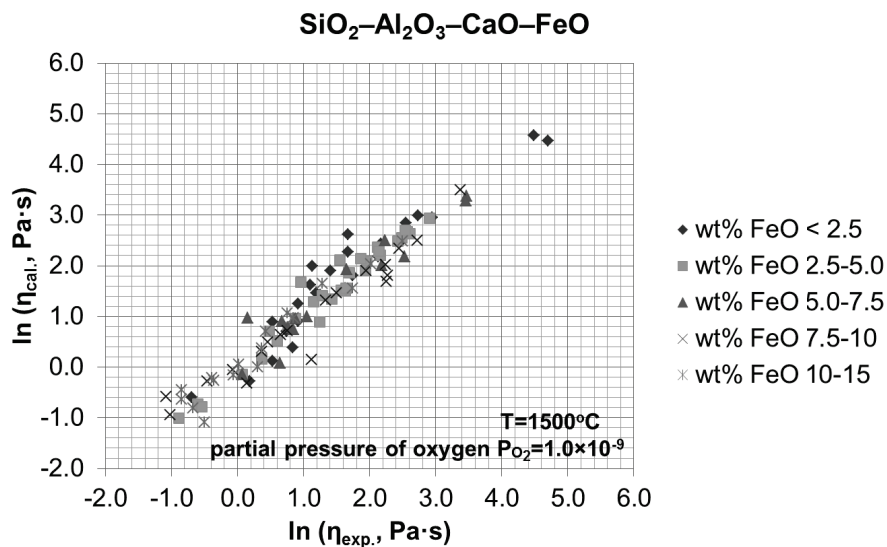


Fig. 5.43. Comparison between experimental data and calculated data in the system SiO₂–Al₂O₃–CaO–FeO at 1500°C

The viscosity of other multicomponent systems, such as the systems $\text{SiO}_2\text{--CaO--FeO}$, $\text{SiO}_2\text{--MgO--FeO}$, $\text{SiO}_2\text{--Al}_2\text{O}_3\text{--FeO}$, and $\text{SiO}_2\text{--CaO--MgO--FeO}$, are also described. It is seen from **Fig. 5.44** that the experimental data given by Chen et al. [214, 215], Ducret and Rankin [216], and Ji et al. [217] are satisfactorily reproduced with the current model.

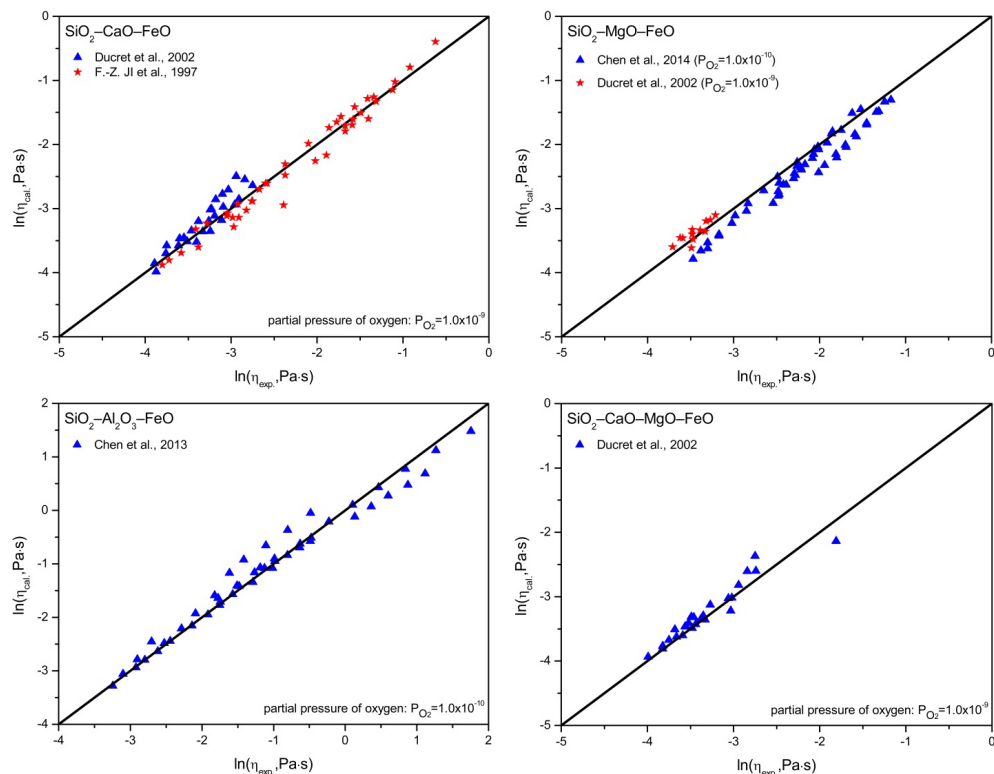


Fig. 5.44. Comparison between experimental data and calculated data in the systems $\text{SiO}_2\text{--CaO--FeO}$, $\text{SiO}_2\text{--MgO--FeO}$, $\text{SiO}_2\text{--Al}_2\text{O}_3\text{--FeO}$, and $\text{SiO}_2\text{--CaO--MgO--FeO}$

It is noted that calculating the viscosity with the current model requires the partial pressure of oxygen, besides the composition and temperature. In the case of no clear partial pressure of oxygen given, the modified optimization process (see **Fig. 4.17**) can be used to obtain the so called optimized partial pressure of oxygen, with which the viscosity can be calculated. As shown in **Fig. 5.45**, viscosities [218] of the system $\text{SiO}_2\text{--MgO--K}_2\text{O--FeO}$ is still properly reproduced even no partial pressure of oxygen is given.

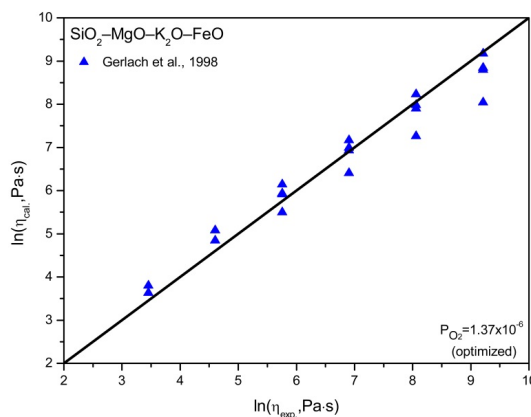


Fig. 5.45. Comparison between experimental data and calculated data in the system $\text{SiO}_2\text{-MgO-K}_2\text{O-FeO}$

5.5.2 Discussion of the local viscosity maximum in the system $\text{SiO}_2\text{-FeO/Fe}_2\text{O}_3$

Due to the fact that the structural role of Fe^{2+} and Fe^{3+} to viscosity differs, the viscosity behavior of $\text{FeO/Fe}_2\text{O}_3$ -containing systems is very complicated. The binary system $\text{SiO}_2\text{-FeO}$, for example, involves a controversial viscosity behavior. A local viscosity maximum occurs in the low range of SiO_2 content, around the fayalite composition (Fe_2SiO_4), which was confirmed by Urbain and Hebd [219], Rontgen et al. [220], Shiraishi et al. [221], and Sumita et al. [222]. However, Kucharski et al. [223] and Chen et al. [224] did not observe this phenomenon. Actually, the reasons for the local viscosity maximum around the fayalite composition are still unclear. Shiraishi et al. stated that the presence of the fayalite cluster in the melt results in the local viscosity maximum [221], whereas Waseda et al. explained this phenomenon with a combination of silicate anion polymerization effect and cation effect [225]. Unfortunately, the viscosity behavior of other binary systems such as $\text{SiO}_2\text{-CaO}$ and $\text{SiO}_2\text{-MgO}$ might not support such explanations, because there is no analogous viscosity maximum in these binary

systems. For example, in the binary system $\text{SiO}_2\text{--CaO}$ a calcium analogue of fayalite Ca_2SiO_4 does not lead to the local viscosity maximum.

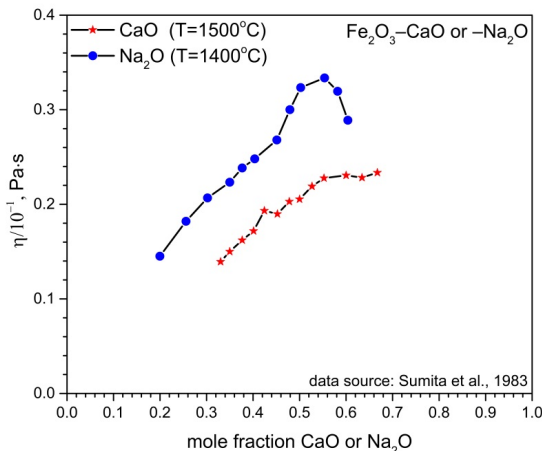


Fig. 5.46. Viscosity maximum in the systems $\text{Fe}_2\text{O}_3\text{--CaO}$ and $\text{Fe}_2\text{O}_3\text{--Na}_2\text{O}$

To explain the local viscosity maximum in the binary system $\text{SiO}_2\text{--FeO/Fe}_2\text{O}_3$, two points should be taken into account. In the silicate melts, the Fe^{2+} - and Fe^{3+} -based species generally coexist. Furthermore, their structural roles to viscosity are different. From **Fig. 4.13**, the Fe^{3+} -based species in the form of CaFe_2O_4 behaves as a network former, which is caused by the Fe^{3+} -induced charge compensation effect. Here, Ca^{2+} charge-compensate Fe^{3+} in tetrahedral coordination, in which the resulting viscosity maximum can be observed in the binary system $\text{CaO--Fe}_2\text{O}_3$ exposed to the air, as shown in **Fig. 5.46**. Compared to the binary system $\text{CaO--Fe}_2\text{O}_3$, the binary system $\text{Na}_2\text{O--Fe}_2\text{O}_3$ shows a much more pronounced viscosity maximum due to a lower ionization potential.

Besides the ions Ca^{2+} and Na^+ , the Fe^{2+} , in principle, can also charge-compensate Fe^{3+} in tetrahedral coordination, which possibly causes the above-mentioned local viscosity maximum in the binary system $\text{SiO}_2\text{--FeO/Fe}_2\text{O}_3$. The charge compensation of FeO_4^{5-} and Fe^{2+} depends on the $\text{Fe}^{2+}/\text{Fe}^{3+}$ ratio, which is in turn dependent on the pressure,

temperature, composition and partial pressure of oxygen. **Fig. 5.47** shows the influence of temperature, composition and partial pressure of oxygen on the ferrous-ferric ratio in the system $\text{SiO}_2\text{--Fe}_2\text{O}_3$. At a constant composition, for example, the $\text{Fe}^{2+}/\text{Fe}^{3+}$ ratio increases with increasing temperature or with decreasing partial pressure of oxygen.

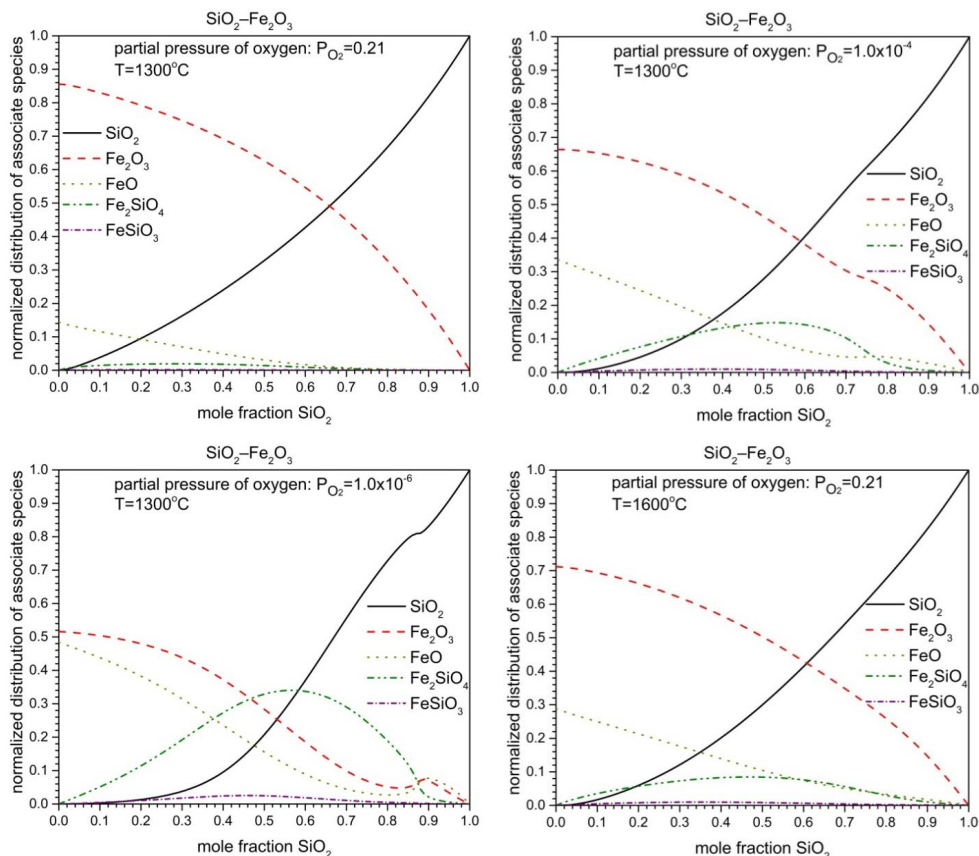


Fig. 5.47. The associate species distribution in the system $\text{SiO}_2\text{--Fe}_2\text{O}_3$

Therefore, the existence of the local viscosity maximum is dependent on the composition, temperature, and partial pressure of oxygen. That is why some researchers such as Rontgen et al. and Sumita et al. observed the local viscosity maximum, whereas some researchers such as Kucharski et al. and Chen et al. did not observe it. To describe this local viscosity maximum with current model, an additional term ($\text{FeO} \cdot \text{SiO}_2 \cdot \text{Fe}_2\text{O}_3$) might be needed, in which three associate species FeO, Fe₂O₃

and SiO_2 inter-polymerize. The corresponding structural change is that FeO_4^{5-} is charge-compensated by Fe^{2+} and forms a Fe^{3+} -based quasi-tetrahedron, which further link to the silica network structure and thereby causes a sharp increase in viscosity.

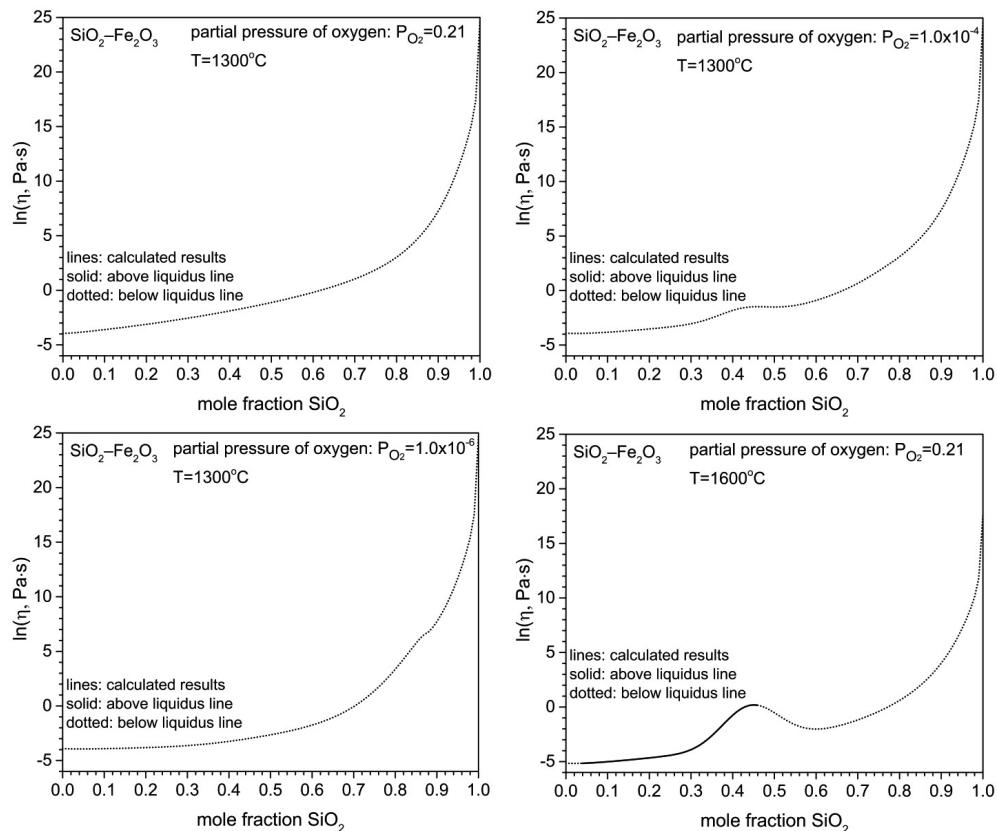


Fig. 5.48. The local viscosity maximum in the system $\text{SiO}_2\text{--Fe}_2\text{O}_3$

The presence of the predicted viscosity maximum, for example, depends on the temperature and partial pressure of oxygen, as shown in **Fig. 5.48**. It should be pointed out that the position of the local viscosity maximum is shifted towards the right of the fayalite composition, which may need further optimization of the corresponding model parameters. Another promising approach is to introduce new associate species such as Fe_3O_4 (i.e. $\text{FeO} \cdot \text{Fe}_2\text{O}_3$) and $\text{Fe}_3\text{Si}_2\text{O}_8$ (i.e. $\text{FeO} \cdot 2\text{SiO}_2 \cdot \text{Fe}_2\text{O}_3$) in the modified associate species model for the description of liquid solution.

5.5.3 Fe_2O_3 -induced charge compensation effect

With the current model, the charge compensation effect can be described by relying on the associate species CaFe_2O_4 , MgFe_2O_4 , NaFeO_2 , and KFeO_2 . **Fig. 5.49** presents the viscosity behavior induced by the charge compensation effect for the binary systems Fe_2O_3 – CaO and Fe_2O_3 – Na_2O . With the current model, the experimental data given by Sumita et al. [222] are properly reproduced. It is seen that a more pronounced viscosity maximum is displayed in the system Na_2O – Fe_2O_3 due to a stronger charge compensation effect.

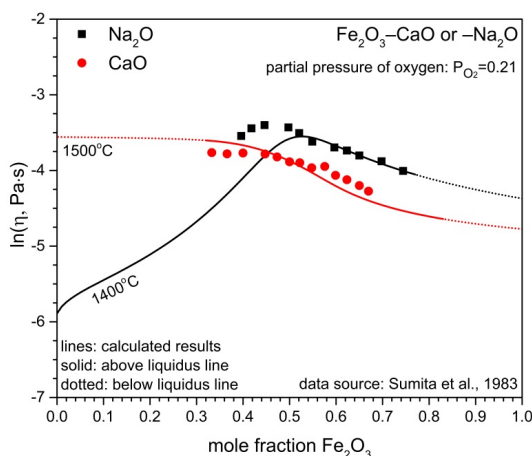


Fig. 5.49. The charge compensation effect in the systems Fe_2O_3 – CaO and Fe_2O_3 – Na_2O

In contrast to the binary systems Fe_2O_3 – Na_2O /CaO, the charge compensation effect of the ternary systems SiO_2 – Al_2O_3 – $\text{FeO}/\text{Fe}_2\text{O}_3$ is more complicated due to the competition of the charge compensators for Al_2O_3 and Fe_2O_3 . As shown in **Fig. 5.50**, the experimental data given by Chen et al. [214] are well reproduced with the current model. At a constant SiO_2 content of 0.40 mole fraction, the viscosity maximum occurs when replacing FeO with Al_2O_3 and the viscosity maximum is located in the peraluminous region. It is noted that the position of the viscosity maximum is shifted towards the

Al_2O_3 -rich side with increasing temperature. Moreover, the position and magnitude of the viscosity maximum are dependent on the partial pressure of oxygen. When the partial pressure of oxygen is increased from 1.0×10^{-10} to 0.21, the position of the viscosity maximum is shifted to the Al_2O_3 -rich side and the viscosity maximum is less pronounced.

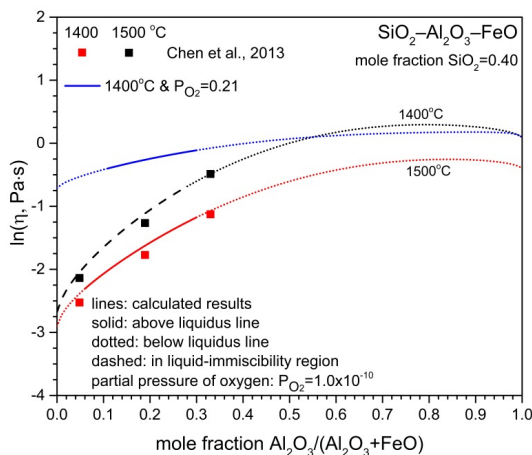


Fig. 5.50. The charge compensation effect in the system $\text{SiO}_2\text{--Al}_2\text{O}_3\text{--FeO}$

The charge compensation effect induced by Fe_2O_3 is weaker than that induced by Al_2O_3 . As seen from **Fig. 5.51**, the Fe^{3+} charge-compensated by K^+ can produce a pronounced viscosity maximum, whereas the viscosity maximum is less pronounced when Fe^{3+} is charge-compensated by Na^+ . The same holds for Ca^{2+} and Mg^{2+} . Another viscosity behavior induced by substituting SiO_2 for Al_2O_3 or Fe_2O_3 demonstrates that the Al_2O_3 has a stronger charge compensation effect than Fe_2O_3 for the same charge compensators.

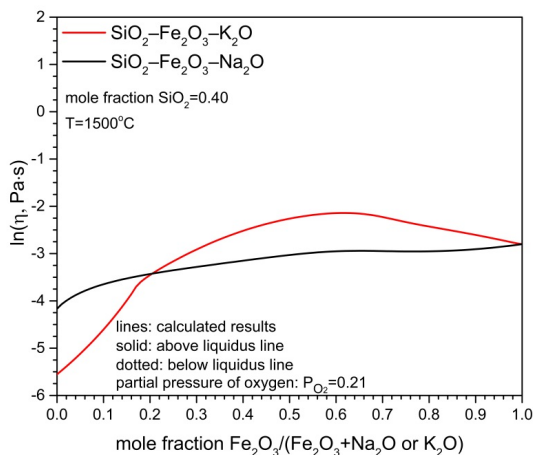


Fig. 5.51. The charge compensation effect in the systems $\text{SiO}_2\text{--Fe}_2\text{O}_3\text{--Na}_2\text{O/K}_2\text{O}$

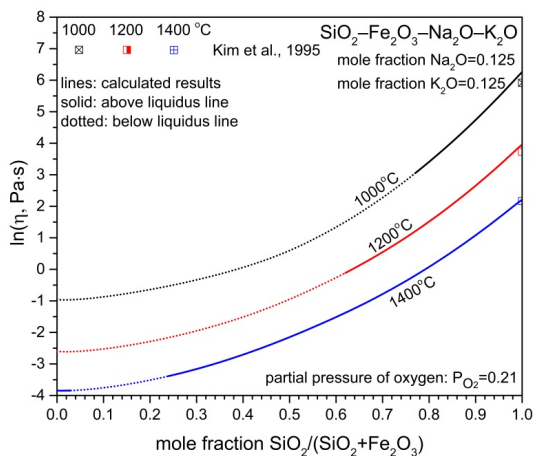


Fig. 5.52. The viscosity behavior with the substitution of SiO_2 for Fe_2O_3 in the system $\text{SiO}_2\text{--Fe}_2\text{O}_3\text{--Na}_2\text{O--K}_2\text{O}$

Compared to the viscosity maximum shown in **Fig. 5.39**, such kind of the viscosity maximum does not occur for the system $\text{SiO}_2\text{--Fe}_2\text{O}_3\text{--Na}_2\text{O--K}_2\text{O}$ when replacing Fe_2O_3 with SiO_2 (see **Fig. 5.52**), which is caused by the weak charge compensation effect between Fe^{3+} and K^+ or Na^+ . That is, the viscosity change resulting from an increased concentration of SiO_2 is always larger than that resulting from the corresponding decreased concentration of the Fe^{3+} -based quasi-tetrahedra and increased concentration of network modifiers that originally act as charge compensators for Fe_2O_3 .

Table 5.3. Composition of four synthetic slags (mole fraction)

Slags	SiO_2	Al_2O_3	Fe_2O_3	CaO
Slag 15	0.40	0.10	0.00	0.50
Slag 16	0.40	0.30	0.00	0.30
Slag 17	0.40	0.15	0.15	0.30
Slag 18	0.40	0.00	0.30	0.30

To further compare the charge compensation effects induced by Al_2O_3 and Fe_2O_3 , the viscosity of four $\text{Al}_2\text{O}_3/\text{Fe}_2\text{O}_3$ -containing slags, as listed in **Table 5.3**, is given by the current model. It is seen that at the same temperature the viscosity of these four slags follows the order: slag 16 > slag 15 > slag 17 > slag 18, as shown in **Fig. 5.53**.

It is easy to understand that the viscosity of slag 16 is greater than that of slag 15 because of more Al^{3+} in tetrahedral coordination for slag 16, whereas it is strange that the viscosity of slag 17 is smaller than that of slag 15, which might be caused by Fe_2O_3 . The redox reaction of Fe^{3+} of Fe^{2+} leads to an increased amount of network modifiers in the slag melts and thereby the effective concentrations of SiO_2 and Al_2O_3 are decreased. Moreover, the Fe_2O_3 -induced charge compensation effect is less pronounced than that induced by Al_2O_3 . As a result, the viscosity of slag 17 is smaller than that of slag 15. If the composition of slag 17 is changed by replacing all Fe_2O_3 with FeO , the viscosity of slag 17 will be larger than that of slag 15, which is denoted with slag 17', as shown in **Fig. 5.53**. Because of the weaker charge compensation effect of Fe_2O_3 as well as the redox reaction of Fe^{3+} and Fe^{2+} , the viscosity of slag 17 is greater than that of slag 18. It

is noted that the viscosity spacing between slag 15 and slag 17 is dependent on temperature, which might be due to the redox reaction of Fe^{3+} and Fe^{2+} depending on the temperature.

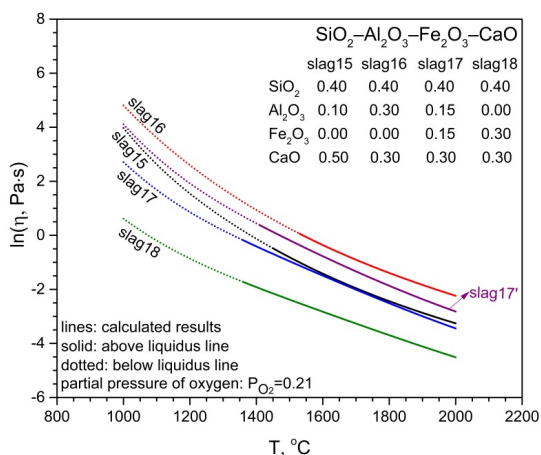


Fig. 5.53. The viscosity of the $\text{Al}_2\text{O}_3/\text{Fe}_2\text{O}_3$ -containing slags

Since the viscosity behavior of the $\text{FeO}/\text{Fe}_2\text{O}_3$ -containing systems is complicated depending on the composition, temperature and partial pressure of oxygen, more reliable experimental data are required to assess the current model parameters.

5.6 Viscosity of real coal ashes

Due to the low availability of experimental data for some systems, such as the system $\text{SiO}_2\text{--CaO--FeO--K}_2\text{O}$, the viscosity measurement is necessary for assessment of the model parameters. For a specific range where the viscosity behavior such as the local viscosity maximum in the system $\text{SiO}_2\text{--FeO}$ is controversial, the viscosity measurement is also needed. The motivation here is to produce experimental data which are further employed to assess the model parameters or to validate the model developed. Since the current model is developed for describing the viscosity of liquid phases in oxide

systems relevant to fuel slags, the viscosity of four coal ashes is measured by the rotating cylinder method in this study.

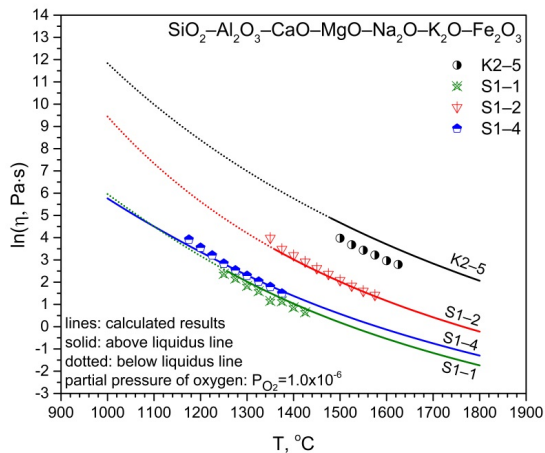


Fig. 5.54. Comparison between experimental data and calculated data for the coal ashes K2-5, S1-1, S1-2, and S1-4

As shown in **Fig. 5.54**, the calculated viscosities agree well with the experimental data points, except for the viscosity of the coal ash K2-5. The magnitude of the viscosities calculated is greater than that of the measured data for K2-5, which might be caused by the deviation of composition. The composition of four coal ashes is listed in **Table 5.4**. It is found that the charge compensation effect has a greater contribution to viscosity for K2-5 due to its high content of SiO_2 . Then the evaporation of charge compensators (for example K_2O) for Al_2O_3 might cause a big deviation of the viscosity measured.

Table 5.4. Main components of four coal ashes (mole fraction)

Coal ashes	SiO_2	Al_2O_3	CaO	MgO	Na_2O	K_2O	Fe_2O_3
K2-5	0.7180	0.1747	0.0206	0.0239	0.0028	0.0320	0.0280
S1-1	0.6292	0.0185	0.2165	0.0873	0.0153	0.0018	0.0314
S1-2	0.5738	0.1739	0.1612	0.0416	0.0206	0.0071	0.0218
S1-4	0.5777	0.0798	0.1785	0.0709	0.0510	0.0105	0.0316

When the composition remains constant during the viscosity measurement, it is reasonable that the viscosity follows the order: K2-5 > S1-2 > S1-4 > S1-1. The current model also gives the same viscosity order. It should be pointed out that the components BaO, Mn₂O₃, and TiO₂ are ignored here when the viscosity of the coal ashes is calculated with the current model. Moreover, the value of partial pressure of oxygen is assumed to be 1.0×10^{-6} .

5.7 Application of the current model in selection of coal ashes fluxing and blending

A reliable viscosity model has been developed, which can be used to generate the iso-viscosity lines and the 3-dimensional viscosity surface. As **Fig. 5.55** shows, the 3-dimensional viscosity surface is presented for the systems $\text{SiO}_2\text{--Al}_2\text{O}_3$, $\text{Al}_2\text{O}_3\text{--CaO}$, and $\text{SiO}_2\text{--Al}_2\text{O}_3\text{--CaO}$.

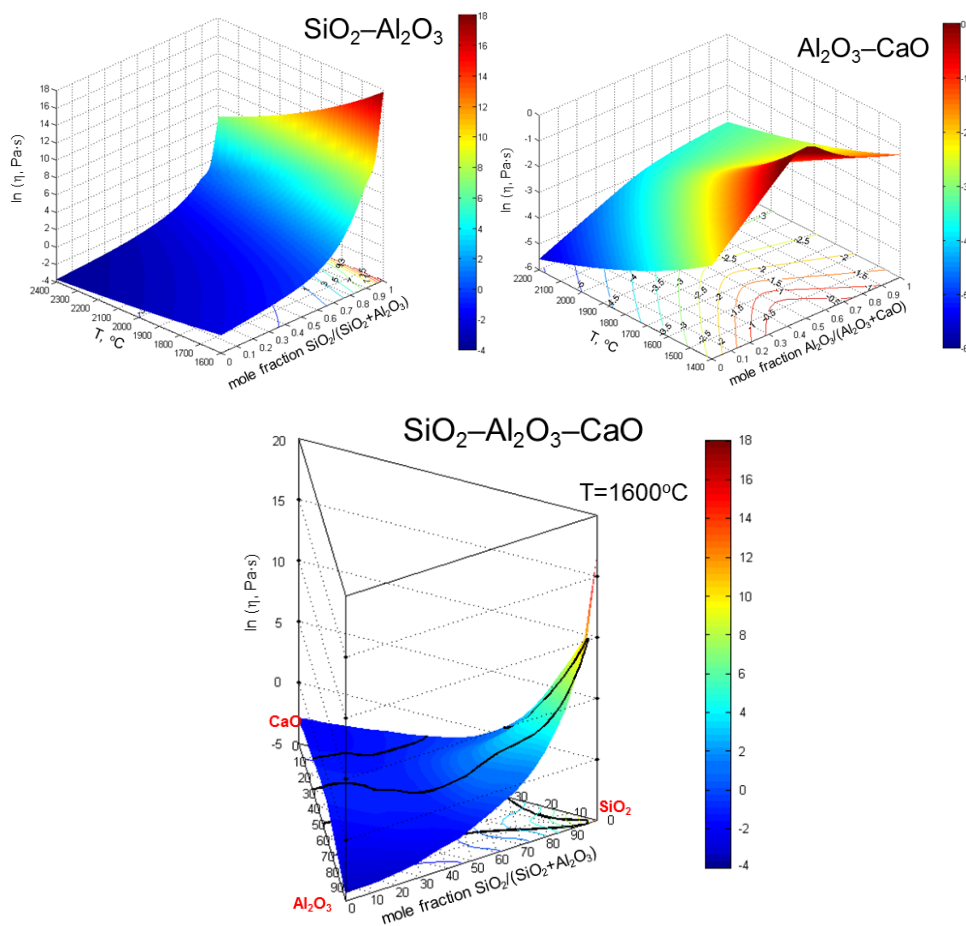


Fig. 5.55. Iso-viscosity lines and viscosity surface in the systems $\text{SiO}_2\text{--Al}_2\text{O}_3$, $\text{Al}_2\text{O}_3\text{--CaO}$, and $\text{SiO}_2\text{--Al}_2\text{O}_3\text{--CaO}$

For the binary systems $\text{SiO}_2\text{--Al}_2\text{O}_3$ and $\text{Al}_2\text{O}_3\text{--CaO}$, the iso-viscosity lines show the way that the temperature-induced viscosity change is compensated by the composition-induced viscosity change. When the temperature remains constant, the way of the change in viscosity is presented with respect to composition for the ternary system $\text{SiO}_2\text{--Al}_2\text{O}_3\text{--CaO}$. That means, the way of the change in viscosity with respect to composition, temperature as well as partial pressure of oxygen (for $\text{FeO}/\text{Fe}_2\text{O}_3$ -containing systems, for example) can be visualized. It is noted that a fully liquid region (within black curves) for the system $\text{SiO}_2\text{--Al}_2\text{O}_3\text{--CaO}$ at 1600°C is identified using the thermodynamic database [96–100]. Such visualization can give a quantitative guideline in selection of the coal ashes fluxing and blending at a given condition.

Visualization of the viscosity can be done not only for simple systems such as the binary system $\text{SiO}_2\text{--Al}_2\text{O}_3$, but also for higher order systems such as the quinary system $\text{SiO}_2\text{--Al}_2\text{O}_3\text{--CaO--MgO--Na}_2\text{O}$. As an example, viscosity of the system $\text{SiO}_2\text{--Al}_2\text{O}_3\text{--CaO--MgO--Na}_2\text{O--K}_2\text{O}$ is visualized at 1600°C and 0.1 mole fraction Na_2O , 0.1 mole fraction K_2O , and 0.2 mole fraction MgO , as shown in **Fig. 5.56**.

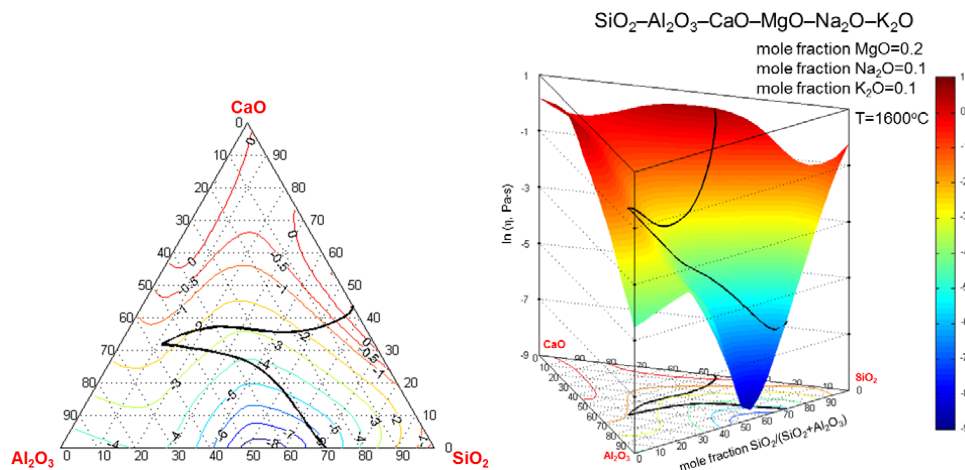


Fig. 5.56. Iso-viscosity lines and viscosity surface in the system $\text{SiO}_2\text{--Al}_2\text{O}_3\text{--CaO--MgO--Na}_2\text{O--K}_2\text{O}$ at 1600°C as well as 0.1 mole fraction Na_2O , 0.1 mole fraction K_2O , and 0.2 mole fraction MgO

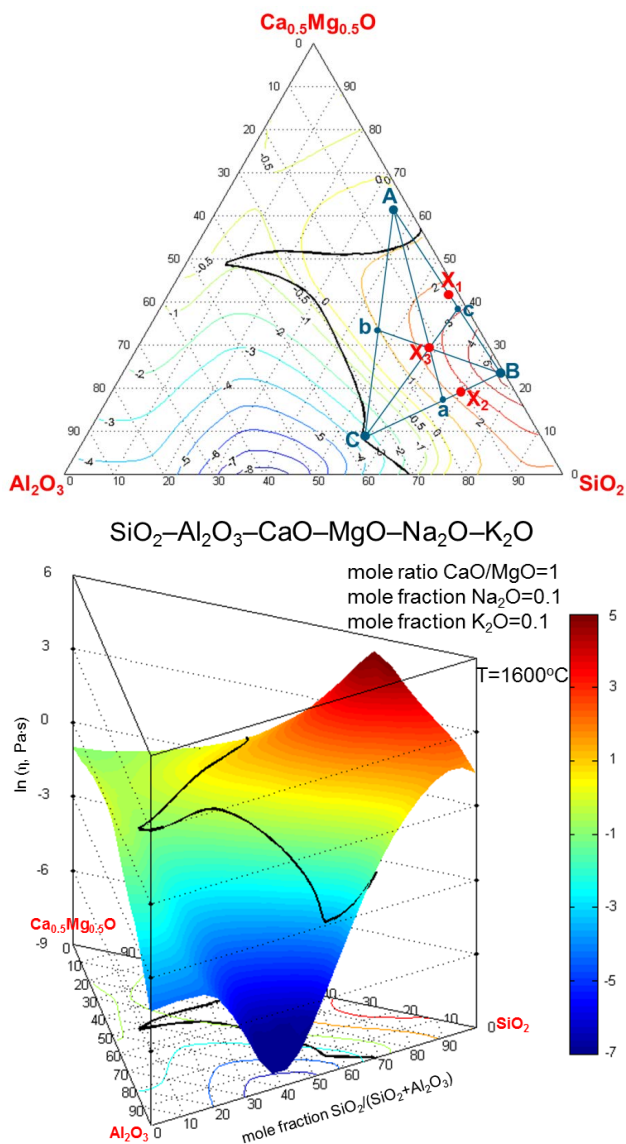


Fig. 5.57. Principle of coal ashes bending

Another example is given to show the principle to select the blending proportions for two or three coal ashes by using such visualization of viscosity, as shown in **Fig. 5.57**. There are three coal ashes which are marked as A, B, and C, whereas the target ash

blend composition is marked as X_1 , X_2 , or X_3 . Then the lever rule is employed to determine the ratio of the amount of two coal ashes, which is expressed as

$$\frac{\text{Amount of Coal ash A}}{\text{Amount of Coal ash B}} = \frac{BX_1}{AX_1} \quad (5.1)$$

$$\frac{\text{Amount of Coal ash B}}{\text{Amount of Coal ash C}} = \frac{CX_2}{BX_2} \quad (5.2)$$

With the same principle, the ratio of amount of three coal ashes can be obtained by

$$\begin{aligned} & \text{Amount of Coal ash A} / \text{Amount of Coal ash B} / \text{Amount of Coal ash C} \\ & = aX_3/bX_3/cX_3 \end{aligned} \quad (5.3)$$

It is noted that the target ash blend composition corresponds to the viscosity values in the range from 2 to 3 on the logarithmic scale (in Pa·s), which is an optimum viscosity range of coal ash slags in slagging gasifier. In contrast, the viscosity of only coal ash B is greater than 400 Pa·s at 1600°C and moreover the viscosity of coal ash A without blending with coal ash B or C should be very large due to the presence of solid phases. Besides the coal ashes blending, the use of fluxes such as CaO and FeO is an alternative approach to adjust the viscosity of coal ash slags. Using the visualization of the viscosity, the composition can be changed by more than one flux and the amount of fluxes is directly obtained to reach an optimum viscosity under certain conditions.

6 Conclusion and outlook

A new structure based model, which we call the modified Arrhenius model, has been developed to describe the viscosity behavior of molten fuel slags in the Newtonian range, based on the thermodynamic modified associate species model.

In the model, the structure of slag is effectively taken into account, in which the viscosity is linked to the type and distribution of species, as well as the connectivity of species. The type of species is determined from the Gibbs energy and thereby the distribution of species is calculated by using a completely self-consistent thermodynamic dataset, where the modified associate species model was applied for the slag. This dataset provides the phase diagram and other thermodynamic properties to be calculated in good agreement with the experimental data. In consequence, both the temperature- and composition-induced structural changes of molten fuel slags have been described with a set of monomeric associate species in combination with the critical clusters induced by the self- and inter-polymerizations. Therefore the dependences of the viscosity on temperature and composition are well described with the current viscosity model.

The calculated data for the pure oxides SiO_2 and Al_2O_3 and slag relevant binary systems $\text{SiO}_2\text{--Al}_2\text{O}_3$, $\text{SiO}_2\text{--CaO}$, $\text{SiO}_2\text{--MgO}$, $\text{SiO}_2\text{--Na}_2\text{O}$, $\text{SiO}_2\text{--K}_2\text{O}$, and $\text{Al}_2\text{O}_3\text{--CaO}$ are in good agreement with the available experimental data using only one set of model parameters, all having a clear physico-chemical meaning. The viscosities of the pure oxides CaO , MgO , Na_2O , and K_2O as well as the binary systems $\text{Al}_2\text{O}_3\text{--MgO}$, $\text{Al}_2\text{O}_3\text{--Na}_2\text{O}$, and $\text{Al}_2\text{O}_3\text{--K}_2\text{O}$ obtained by way of extrapolation of the corresponding higher order systems also show a very reasonable behavior. With the new model, one of the challenges of the viscosity behavior in SiO_2 -based binary systems, the so called lubricant effect, can be described very well by relying on the monomeric associate species as well as the two common critical silica clusters $(\text{SiO}_2)_6$ and $(\text{SiO}_2)_{109}$. Another challenge in Al_2O_3 -based binary systems, the amphoteric or charge compensation effect, can also be described very well by relying on the monomeric associate species CaAl_2O_4 , MgAl_2O_4 , NaAlO_2 , or KAlO_2 .

The new model has been extended to describe the viscosity of the system $\text{SiO}_2\text{--Al}_2\text{O}_3\text{--CaO--MgO--Na}_2\text{O--K}_2\text{O}$ and its ternary or higher order subsystems. In the multicomponent systems without Al_2O_3 , four ternary associate species $\text{Na}_2\text{Si}_6\text{Ca}_3\text{O}_{16}$, K_2SiCaO_4 , K_2SiMgO_4 , and $\text{K}_2\text{Si}_5\text{MgO}_{12}$, besides the monomeric associate species employed for the pure oxides and binary systems, are used to describe the viscosity. To describe the Al_2O_3 -induced viscosity maximum, the monomeric associate species CaAl_2O_4 , MgAl_2O_4 , $\text{CaSi}_2\text{Al}_2\text{O}_8$, and $\text{Mg}_2\text{Si}_5\text{Al}_4\text{O}_{18}$ in systems containing alkaline earth oxides or NaAlO_2 , KAlO_2 , NaSiAlO_4 , KSiAlO_4 , $\text{NaSi}_3\text{AlO}_8$, and KSi_2AlO_6 in systems containing alkali oxides are employed. The monomeric associate species CaAl_2O_4 , MgAl_2O_4 , NaAlO_2 , and KAlO_2 represent quasi-tetrahedra behaving like silica tetrahedra. Some of the Al^{3+} -based quasi-tetrahedra can interconnect with the silica network structure. These are described by way of the ternary associate species $\text{CaSi}_2\text{Al}_2\text{O}_8$, $\text{Mg}_2\text{Si}_5\text{Al}_4\text{O}_{18}$, NaSiAlO_4 , KSiAlO_4 , $\text{NaSi}_3\text{AlO}_8$, and KSi_2AlO_6 . The model parameters for the ternary associate species have been assessed using more than 4500 experimental data points. As a result, the viscosities for the systems $\text{SiO}_2\text{--CaO--MgO}$, $\text{SiO}_2\text{--CaO--Na}_2\text{O}$, $\text{SiO}_2\text{--Na}_2\text{O--K}_2\text{O}$, $\text{SiO}_2\text{--Al}_2\text{O}_3\text{--CaO}$, $\text{SiO}_2\text{--Al}_2\text{O}_3\text{--MgO}$, $\text{SiO}_2\text{--Al}_2\text{O}_3\text{--Na}_2\text{O}$, $\text{SiO}_2\text{--Al}_2\text{O}_3\text{--K}_2\text{O}$, $\text{SiO}_2\text{--Al}_2\text{O}_3\text{--CaO--MgO}$, $\text{SiO}_2\text{--Al}_2\text{O}_3\text{--CaO--Na}_2\text{O}$, $\text{SiO}_2\text{--Al}_2\text{O}_3\text{--Na}_2\text{O--K}_2\text{O}$, $\text{SiO}_2\text{--CaO--MgO--Na}_2\text{O--K}_2\text{O}$, and $\text{SiO}_2\text{--Al}_2\text{O}_3\text{--CaO--MgO--Na}_2\text{O--K}_2\text{O}$ are well described. The influence of different oxides CaO , MgO , Na_2O , and K_2O on the viscosity in systems with or without Al_2O_3 is well predicted. The viscosity behavior when substituting one network modifier for another at constant SiO_2 contents is well described. The Al_2O_3 -induced viscosity maximum is also well described, in which the position and magnitude of the maximum as a function of composition and temperature (charge compensation effect) are properly predicted. Another viscosity maximum when replacing Al_2O_3 with SiO_2 for constant contents of the network modifiers is well presented. Moreover, the viscosities extrapolated from lower order systems to corresponding higher order systems are in good agreement with the experimental data, which indicates that the current model is self-consistent.

The new model has also been extended to describe the viscosity of the $\text{FeO/Fe}_2\text{O}_3$ -containing systems. For description of the $\text{Fe}^{2+}/\text{Fe}^{3+}$ -induced structural change in the system $\text{SiO}_2\text{--Al}_2\text{O}_3\text{--CaO--MgO--Na}_2\text{O--K}_2\text{O--FeO--Fe}_2\text{O}_3$, 14 Fe-containing associate

species are employed, among which the associate species CaFe_2O_4 , MgFe_2O_4 , NaFeO_2 , and KFeO_2 representing Fe^{3+} -based quasi-tetrahedra behave as network formers. No ternary associate species are employed to describe the Fe^{3+} -induced charge compensation effect. The model parameters for the $\text{FeO}/\text{Fe}_2\text{O}_3$ -containing systems have been assessed using more than 1600 experimental data points with known partial pressure of oxygen. As a result, the viscosity in the investigated systems SiO_2 - FeO , SiO_2 - Fe_2O_3 , Fe_2O_3 - CaO , Fe_2O_3 - Na_2O , SiO_2 - CaO - FeO , SiO_2 - MgO - FeO , SiO_2 - Al_2O_3 - FeO , SiO_2 - Fe_2O_3 - Na_2O , SiO_2 - Fe_2O_3 - K_2O , SiO_2 - CaO - MgO - FeO , SiO_2 - MgO - K_2O - FeO , SiO_2 - Fe_2O_3 - Na_2O - K_2O , SiO_2 - Al_2O_3 - FeO - CaO , SiO_2 - Al_2O_3 - Fe_2O_3 - CaO , and SiO_2 - Al_2O_3 - CaO - MgO - Na_2O - K_2O - Fe_2O_3 is properly described. The local viscosity maximum in the system SiO_2 - $\text{FeO}/\text{Fe}_2\text{O}_3$ might be described by relying on an additional structural term ($\text{FeO} \cdot \text{SiO}_2 \cdot \text{Fe}_2\text{O}_3$). The Fe^{3+} -induced charge compensation effect is less pronounced than that induced by Al^{3+} . The Fe^{3+} -induced viscosity maximum does not always occur depending on the charge compensators for Fe^{3+} . The viscosity maximum when replacing Fe_2O_3 with SiO_2 for constant contents of the other network modifiers does not occur. Moreover, the partial pressure of oxygen plays an important role in modelling the viscosity of the $\text{FeO}/\text{Fe}_2\text{O}_3$ -containing systems.

With the new model, the iso-viscosity lines and 3-dimensional viscosity surfaces are generated for selecting the coal ash fluxing and blending. The next step is to further assess the model parameters for the $\text{FeO}/\text{Fe}_2\text{O}_3$ -containing systems. Then the model will be extended by further relevant oxides such as P_2O_5 , which is usually contained in fuel slags, and the model thereby is capable of describing the viscosity of P_2O_5 -containing systems for a better selection of the optimum operating condition in gasifiers. Further viscosity measurements are also necessary to validate the current model. In addition, partly-crystallized slags are common in slagging gasifiers. Therefore, the model needs to be extended from fully liquid phase to mixtures of liquid and solids, in which the crystallization kinetics should be taken into account.

References

- [1] Y. Huang, S. Rezvani, D. McIlveen-Wright, A. Minchener, N. Hewitt, Techno-economic study of CO₂ capture and storage in coal fired oxygen fed entrained flow IGCC power plants, *Fuel Process. Technol.*, 89 (2008) 916–925.
- [2] R.W. Breault, Gasification processes old and new: a basic review of the major technologies, *Energies*, 3 (2010) 216–240.
- [3] C. Higman, M.V.D. Burgt, *Gasification*, 2nd edition, Gulf Professional Publishing, Elsevier, USA, 2008.
- [4] P. Wang, M. Massoudi, Slag Behavior in Gasifiers. Part I: Influence of Coal Properties and Gasification Conditions, *Energies*, 6 (2013) 784–806.
- [5] M.J. Brannon, G.W. Ollis, G.L. Shoaf, Expanding the range of suitable gasification fuels, *Fuel Process. Technol.*, 99 (2012) 1–5.
- [6] A. Kondratiev, E. Jak, Predicting coal ash slag flow characteristics (viscosity model for the Al₂O₃–CaO–FeO–SiO₂ system), *Fuel*, 80 (2001) 1989–2000.
- [7] H.J. Hurst, F. Novak, J.H. Patterson, Viscosity measurements and empirical predictions for fluxed Australian bituminous coal ashes, *Fuel*, 78 (1999) 1831–1840.
- [8] S.K. Sundaram, K.I. Johnson, J. Matyas, R.E. Williford, S.P. Pilli, V.N. Korolev, An Integrated Approach to Coal Gasifier Testing, Modeling, and Process Optimization, *Energy Fuels*, 23 (2009) 4748–4754.
- [9] D.G. Roberts, D.J. Harris, A. Tremel, A.Y. Ilyushechkin, Linking laboratory data with pilot scale entrained flow coal gasification performance. Part 2: Pilot scale testing, *Fuel Process. Technol.*, 94 (2012) 26–33.
- [10] S. Arrhenius, Über die innere Reibung verdünnter wässriger Lösungen, *Z. Phys. Chem.*, S.1 (1887) 285–298.
- [11] H.D. Weymann, On the Hole Theory of Viscosity, Compressibility, and Expansivity of Liquids, *Kolloid-Z. Z. Polymere*, 181 (1962) 131–137.
- [12] T. Lakatos, L.G. Johansson, B. Simmingskold, Viscosity-temperature relations in the glass system SiO₂–Al₂O₃–Na₂O–K₂O–CaO–MgO in the composition range of technical glasses, *Glass Tech.*, 13 (1972) 88–95.
- [13] G. Urbain, Y. Bottinga, P. Richet, Viscosity of liquid silica, silicates and alumino-silicates, *Geochim. Cosmochim. Acta*, 46 (1982) 1061–1072.
- [14] P.V. Riboud, Y. Roux, D. Lucas, H. Gayes, Improvement of continuous casting powders, *Fachber. Huttenprax. Metallweiterverarb.*, 19 (1981) 859–869.
- [15] H. Hu, R.G. Reddy, Modeling of Viscosities of Binary Alkaline-Earth Metal oxide and Silica Melts, *High Temp. Sci.*, 28 (1990) 195–202.

References

- [16] S.Z. Yong, A. Ghoniem, Modeling the slag layer in solid fuel gasification and combustion—Two way coupling with CFD, *Fuel*, 97 (2012) 457–466.
- [17] L. Forsbacka, Experimental study and modelling of viscosity of chromium containing slags, Thesis, Helsinki University of Technology, 2007.
- [18] F.J. Keller, W.E. Gettys, M.J. Skove, *Physics Classical and Modern*, McGraw-Hill, United States, 1989.
- [19] H. Scholze, N.J. Kreidl, Technological aspects of viscosity: viscosity and relaxation, *Glass Sci. Tech.*, 3 (1986) 233–273.
- [20] S. Vargas, F.J. Frandsen, K. Dam-Johansen, Rheological properties of high-temperature melts of coal ashes and other silicates, *Prog. Energy Combust. Sci.*, 27 (2001) 237–426.
- [21] H.A. Barnes, J.F. Hutton, K. Walters, *An introduction to rheology*, Elsevier, Amsterdam, 1989.
- [22] R.P. Chhabra, Non-Newtonian Fluids: An Introduction, in: SERC School-cum-Symposium on Rheology of Complex Fluids, India, 2010.
- [23] R.B. Heimann, *Classic and Advanced Ceramics: From Fundamentals to Applications*, Wiley-VCH, 2010.
- [24] L. Wang, Experimental and modelling studies of the thermophysical and thermo-chemical properties of some slag systems, Thesis, KTH, 2009.
- [25] W.H. Zachariasen, Atomic Arrangement in Glass, *J. Amer. Chem. Soc.*, 54 (1932) 3841–3851.
- [26] B.E. Warren, J. Biscoe, Fourier analysis of X-Ray patterns of soda-silica glass, *J. Amer. Ceram. Soc.*, 21 (1938) 259–265.
- [27] G.N. Greaves, EXAFS and the structure of glass, *J. Non-Cryst. Solids*, 71 (1985) 203–217.
- [28] J.O.M. Bockris, J.D. Mackenzie, J.A. Kitchener, Viscous flow in silica and binary liquid silicates, *Trans. Faraday Soc.*, 51 (1955) 1734–1748.
- [29] B.W.M. Thomas, R.N. Mead, G. Mountjoy, A molecular dynamics study of the atomic structure of $(\text{CaO})_x(\text{Al}_2\text{O}_3)_{1-x}$ glass with $x = 0.625$ close to the eutectic, *J. Phys. Condens. Matter*, 18 (2006) 4697–4708.
- [30] J.H. Park, D.J. Min, H.S. Song, Amphoteric behavior of alumina in viscous flow and structure of $\text{CaO-SiO}_2\text{-(MgO)-Al}_2\text{O}_3$ slags, *Metall. Mater. Trans. B*, 35 (2004) 269–275.
- [31] H. Eyring, The theory of absolute reaction rates, *Trans. Faraday Soc.*, 34 (1938) 41–48.
- [32] Y. Bottinga, P. Richet, A. Sipp, Viscosity regimes of homogeneous silicate melts, *Amer. Mineral.*, 80 (1995) 305–318.

- [33] P. Richet, R.A. Robie, B.S. Hemingway, Low-temperature heat capacity of diopside glass ($\text{CaMgSi}_2\text{O}_6$): A calorimetric test of the configurational-entropy theory applied to the viscosity of liquid silicates, *Geochim. Cosmochim. Acta*, 50 (1986) 1521–1533.
- [34] J.-S. Wang, R.S. Porter, On the viscosity-temperature behavior of polymer melts, *Rheol. Acta*, 34 (1995) 496–503.
- [35] H. Vogel, Das Temperaturabhängigkeitsgesetz der Viskosität von Flüssigkeiten, *J. Physik Z.*, 22 (1921) 645–646.
- [36] G.S. Fulcher, Analysis of recent measurements of the viscosity of glasses, *J. Am. Ceram. Soc.*, 8 (1925) 339–355.
- [37] G. Tammann, W. Hesse, Die Abhängigkeit der Viskosität von der Temperatur bei unterkühlten Flüssigkeiten, *Z. Anorg. Allg. Chem.*, 156 (1926) 245–257.
- [38] G. Urbain, Viscosity of silicate melts: measure and estimation, *J. Mater. Educ.*, 7 (1985) 1007–1078.
- [39] L. Gan, C. Lai, A general viscosity model for molten blast furnace slag, *Metall. Mater. Trans. B*, 45 (2013) 875–888.
- [40] J.C. Mauro, Y. Yue, A.J. Ellison, P.K. Gupta, D.C. Allan, Viscosity of glass-forming liquids, in: *Proc. Natl. Acad. Sci. USA*, 2009, pp. 19780–19784.
- [41] H. Taniguchi, Entropy dependence of viscosity and the glass-transition temperature of melts in the system diopside-anorthite, *Contrib. Mineral. Petrol.*, 109 (1992) 295–303.
- [42] P. Richet, Viscosity and configurational entropy of silicate melts, *Geochim. Cosmochim. Acta*, 48 (1984) 471–483.
- [43] S. Glasstone, K.J. Laidler, H. Eyring, *The theory of rate processes: the kinetics of chemical reactions, viscosity, diffusion and electrochemical phenomena*, McGraw-Hill, New York, 1941.
- [44] R. Fürth, On the theory of the liquid state III. The hole theory of the viscous flow of liquids, *Math. Proc. Camb. Philo. Soc.*, 37 (1941) 281–290.
- [45] F.C. Auluck, S.C. De, D.S. Kothari, The hole theory of liquid state, *Proc. Nat. Inst. Sci.*, 10 (1944) 397–405.
- [46] K.C. Mills, M. Franken, N. Machingawuta, P. Green, C. Broadbent, G. Urbain, R. Scheel, J. Hocevoir, J.N. Pontoire, NPL Report No. DMM (A) 30, National Physical Laboratory, UK, 1991, pp. 1–67.
- [47] J.O.M. Bockris, A.K.N. Reddy, *Ionic Liquids*, Chapter 5, *Modern Electrochemistry 2nd Edition*, Plenum Press, New York, 1998.
- [48] A. Milchev, I. Avramov, On the Influence of Amorphization on Atomic Diffusion in Condensed Systems, *Phys. Stat. Sol. (b)*, 120 (1983) 123–130.
- [49] N. Hirai, H. Eyring, Bulk Viscosity of Liquids, *J. Appl. Phys.*, 29 (1958) 810–816.

- [50] I. Avramov, A. Milchev, Effect of disorder on diffusion and viscosity in condensed systems, *J. Non-Cryst. Solids*, 104 (1988) 253–260.
- [51] I. Avramov, Influence of disorder on viscosity of undercooled melts, *J. Chem. Phys.*, 95 (1991) 4439–4443.
- [52] H.R. Shaw, Viscosities of magmatic silicate liquids: An empirical method of prediction, *Am. J. Sci.*, 272 (1972) 870–893.
- [53] Y. Bottinga, D.F. Weill, The viscosity of magmatic silicate liquids: A model for calculation, *Am. J. Sci.*, 272 (1972) 438–475.
- [54] G. Urbain, F. Cambier, M. Deletter, M.R. Anseau, Viscosity of Silicate Melts, *Trans. J. Br. Ceram. Soc.*, 80 (1981) 139–141.
- [55] K.C. Mills, C.P. Broadbent, Evaluation of 'slags' program for the prediction of physical properties of coal gasification slags, in: *The impact of ash deposition on coal fired plants: Proceedings of the Engineering Foundation Conference*, UK, 1993, pp. 513–525.
- [56] A. Kondratiev, E. Jak, Review of Experimental Data and Modeling of the Viscosities of Fully Liquid Slags in the Al_2O_3 – CaO – FeO – SiO_2 System, *Metall. Mater. Trans. B*, 32 (2001) 1015–1025.
- [57] D.P. Kalmanovitch, M. Frank, An effective model of viscosity for ash deposition phenomena, in: *Proceedings of the engineering foundation conference on mineral matter and ash deposition from coal*, Santa Barbara, CA, 1988, pp. 89–101.
- [58] S. Srinivasachar, C.L. Senior, J.J. Helble, J.W. Moore, A fundamental approach to the prediction of coal ash deposit formation in combustion systems, in: *24th Symp. (Int.) Comb.*, 1992, pp. 1179–1187.
- [59] E. Jak, D. Saulov, A. Kondratiev, P.C. Hayes, Prediction of phase equilibria and viscosity in complex coal ash slag systems, *Prepr. Pap. Am. Chem. Soc., Div. Fuel Chem.*, 49 (2004) 159–162.
- [60] H.J. Hurst, F. Novak, J.H. Patterson, Viscosity models for fluxed Australian bituminous coal ashes, in: *Proc. V International Conference on Molten Slags, Fluxes and Salts*, Sydney, Australia, 1997, pp. 873–876.
- [61] H.J. Hurst, F. Novak, J.H. Patterson, Viscosity measurements and empirical predictions for some model gasifier slags, *Fuel*, 78 (1999) 439–444.
- [62] H.J. Hurst, J.H. Patterson, A. Quintanar, Viscosity measurements and empirical predictions for some model gasifier slags—II, *Fuel*, 79 (2000) 1797–1799.
- [63] A.Y. Ilyushechkin, S.S. Hla, Viscosity of High-Iron Slags from Australian Coals, *Energy Fuels*, 27 (2013) 3736–3742.
- [64] A. Kondratiev, E. Jak, Modeling of Viscosities of the Partly Crystallized Slags in the Al_2O_3 – CaO – FeO – SiO_2 System, *Metall. Mater. Trans. B*, 32 (2001) 1027–1032.

- [65] L. Zhang, S. Jahanshahi, Review and Modeling of Viscosity of Silicate Melts: Part I. Viscosity of Binary and Ternary Silicates Containing CaO, MgO, and MnO, *Metall. Mater. Trans. B*, 29 (1998) 177–186.
- [66] L. Zhang, S. Jahanshahi, Review and Modeling of Viscosity of Silicate Melts: Part II. Viscosity of Melts Containing Iron Oxide in the CaO–MgO–MnO–FeO–Fe₂O₃–SiO₂ System, *Metall. Mater. Trans. B*, 29 (1998) 187–195.
- [67] R.G. Reddy, J.Y. Yen, Z. Zhang, Viscosities of Na₂O–SiO₂–B₂O₃ melts, in: *Proc. V International Conference on Molten Slags, Fluxes and Salts*, Sydney, Australia, 1997, pp. 203–213.
- [68] Z.J. Zhang, R.G. Reddy, Experimental Determination and Modeling of Na₂O–SiO₂–B₂O₃ Melts Viscosities, *High Temp. Mater. Process.*, 23 (2004) 247–260.
- [69] T. Iida, H. Sakai, Y. Kita, K. Shigeno, An equation for accurate prediction of the viscosities of blast furnace type slags from chemical composition, *ISIJ Int.*, 40 (2000) S110–S114.
- [70] L. Forsbacka, L. Holappa, Viscosity of SiO₂–CaO–CrO_x slags in contact with metallic chromium and application of the Iida model, in: *Proc. VII International Conference on Molten Slags, Fluxes and Salts*, Capetown, SAIMM, Johannesburg, 2004, pp. 129–136.
- [71] D. Sichen, J. Bygdén, S. Seetharaman, A Model for Estimation of Viscosities of Complex Metallic and Ionic Melts, *Metall. Mater. Trans. B*, 25 (1994) 519–525.
- [72] S. Seetharaman, D. Sichen, Estimation of the Viscosities of Binary Metallic Melts Using Gibbs Energies of Mixing, *Metall. Mater. Trans. B*, 25 (1994) 589–595.
- [73] S. Seetharaman, K. Mukai, D. Sichen, Viscosities of slags—an overview, in: *Proc. VII International Conference on Molten Slags, Fluxes and Salts*, Capetown, SAIMM, Johannesburg, 2004, pp. 31–42.
- [74] I. Avramov, C. Rüssel, R. Keding, Effect of chemical composition on viscosity of oxide glasses, *J. Non-Cryst. Solids*, 324 (2003) 29–35.
- [75] T. Nentwig, Experimental determination and numerical simulation of viscosities in slag-systems under gasification conditions, Thesis, RWTH Aachen University, 2011.
- [76] A. Kondratiev, E. Jak, A Quasi-Chemical Viscosity Model for Fully Liquid Slags in the Al₂O₃–CaO–FeO–SiO₂ System, *Metall. Mater. Trans. B*, 36 (2005) 623–638.
- [77] A.N. Grundy, H. Liu, I.-H. Jung, S.A. Decterov, A.D. Pelton, A model to calculate the viscosity of silicate melts Part I: Viscosity of binary SiO₂–MeO_x systems (Me = Na, K, Ca, Mg, Al), *Int. J. Mater. Res.*, 99 (2008) 1185–1194.
- [78] A.N. Grundy, I.-H. Jung, A.D. Pelton, S.A. Decterov, A model to calculate the viscosity of silicate melts Part II: The NaO_{0.5}–MgO–CaO–AlO_{1.5}–SiO₂ system, *Int. J. Mater. Res.*, 99 (2008) 1195–1209.
- [79] W.-Y. Kim, A.D. Pelton, S.A. Decterov, A model to calculate the viscosity of silicate melts Part III: Modification for melts containing alkali oxides, *Int. J. Mater. Res.*, 103 (2012) 313–328.

- [80] A. Kondratiev, E. Jak, P.C. Hayes, Predicting Slag Viscosities in Metallurgical Systems, *JOM*, 54 (2002) 41–45.
- [81] A. Einstein, Eine neue Bestimmung der Moleküldimensionen, *Ann. Phys.*, 19 (1906) 289–306.
- [82] A. Einstein, Berichtigung zu meiner Arbeit: “Eine neue Bestimmung der Moleküldimensionen”, *Ann. Phys.*, 34 (1911) 591–592.
- [83] S.G. Ward, R.L. Whitmore, Studies of the viscosity and sedimentation of suspensions Part 1.–The viscosity of suspension of spherical particles, *Br. J. Appl. Phys.*, 1 (1950) 286–290.
- [84] R. Roscoe, The viscosity of suspensions of rigid spheres, *Br. J. Appl. Phys.*, 3 (1952) 267–269.
- [85] V. Vand, Viscosity of solutions and suspensions: I. Theory, *J. Phys. Coll. Chem.*, 52 (1948) 277–299.
- [86] L. Wu, M. Ek, M. Song, D. Sichen, The Effect of Solid Particles on Liquid Viscosity, *Steel research int.*, 82 (2011) 388–397.
- [87] C.K. Schoff, P. Kamarchik Jr., Rheological measurements, in: *Encyclopedia of chemical technology: recycling, oil to silicon*, Wiley, New York, 1997, pp. 347–404.
- [88] S. English, The effect of composition on the viscosity of glass, *J. Soc. Glass Technol.*, 8 (1924) 205–248.
- [89] G.J. Dienes, H.F. Klemm, Theory and application of the parallel plate plastometer, *J. Appl. Phys.*, 17 (1946) 458–471.
- [90] B.R. Stanmore, S. Budd, Measuring the viscous flow of molten coal ash, *Fuel*, 75 (1996) 1476–1479.
- [91] K.C. Mills, Viscosities of molten slags, Chapter 9, *Slag Atlas 2nd Edition*, VDEh, Düsseldorf, 1995.
- [92] D.R. Rohindra, R.A. Lata, R.K. Coll, A simple experiment to determine the activation energy of the viscous flow of polymer solutions using a glass capillary viscometer, *Eur. J. Phys.*, 33 (2012) 1457–1464.
- [93] R.E. Aune, S. Sridhar, M. Hayashi, Viscosities and Gibbs Energies—On a Common Structural Base, *High Temp. Mater. Processes (London)*, 22 (2003) 369–378.
- [94] N.L. Bowen, J.W. Greig, The System $\text{Al}_2\text{O}_3\text{--SiO}_2$, *J. Am. Ceram. Soc.*, 7 (1924) 238–254.
- [95] T.M. Besmann, K.E. Spear, Thermochemical Modeling of Oxide Glasses, *J. Am. Ceram. Soc.*, 85 (2002) 2887–2894.
- [96] E. Yazhenskikh, K. Hack, M. Müller, Critical thermodynamic evaluation of oxide systems relevant to fuel ashes and slags. Part 1: Alkali oxide–silica systems, *Calphad*, 30 (2006) 270–276.

- [97] E. Yazhenskikh, K. Hack, M. Müller, Critical thermodynamic evaluation of oxide systems relevant to fuel ashes and slags Part 2: Alkali oxide–alumina systems, *Calphad*, 30 (2006) 397–404.
- [98] E. Yazhenskikh, K. Hack, M. Müller, Critical thermodynamic evaluation of oxide systems relevant to fuel ashes and slags. Part 3: Silica–alumina system, *Calphad*, 32 (2008) 195–205.
- [99] E. Yazhenskikh, K. Hack, M. Müller, Critical thermodynamic evaluation of oxide systems relevant to fuel ashes and slags, Part 4: Sodium oxide–potassium oxide–silica, *Calphad*, 32 (2008) 506–513.
- [100] E. Yazhenskikh, K. Hack, M. Müller, Critical thermodynamic evaluation of oxide systems relevant to fuel ashes and slags, Part 5: Potassium oxide–alumina–silica, *Calphad*, 35 (2011) 6–19.
- [101] A.L. Gentile, W.R. Foster, Calcium Hexaluminate and Its Stability Relations in the System $\text{CaO-Al}_2\text{O}_3\text{-SiO}_2$, *J. Amer. Ceramic Soc.*, 46 (1963) 74–76.
- [102] K. Hack, T. Jantzen, Progress in data assessments for HotVegas project, in: GTT Annual Workshop 2010, Herzogenrath, Aachen, 2010.
- [103] L. Olivier, X. Yuan, A.N. Cormack, C. Jäger, Combined ^{29}Si double quantum NMR and MD simulation studies of network connectivities of binary $\text{Na}_2\text{O-SiO}_2$ glasses new prospects and problems, *J. Non-Cryst. Solids*, 293–295 (2001) 53–66.
- [104] W.E. Halter, B.O. Mysen, Melt speciation in the system $\text{Na}_2\text{O-SiO}_2$, *Chem. Geol.*, 213 (2004) 115–123.
- [105] H. Maekawa, T. Maekawa, K. Kawamura, T. Yokokawa, The structural groups of alkali silicate glasses determined from ^{29}Si MAS-NMR, *J. Non-Cryst. Solids*, 127 (1991) 53–64.
- [106] <http://www.3dchem.com/3dinorgmolecule.asp?ID=904>.
- [107] T. Uchino, Y. Tokuda, T. Yoko, Vibrational dynamics of defect modes in vitreous silica, *Phys. Rev. B*, 58 (1998) 5322–5328.
- [108] A.I. Zaitsev, B.M. Mogutnov, Thermodynamics of CaO-SiO_2 and MnO-SiO_2 melts: II. Thermodynamic Modeling and Phase-Equilibrium Calculations, *Inorg. Mater.*, 33 (1997) 823–831.
- [109] V.M. Breus, L.F. Kosoi, V.M. Ermolov, Viscosity of titanium containing calcium-alumina slags, *Izv. Vyssh. Uchebn. Zaved., Chern. Metall.*, 26 (1983) 41–44.
- [110] P. Kozakevitch, Viscosité et éléments structuraux des aluminosilicates fondus: laitiers $\text{CaO-Al}_2\text{O}_3\text{-SiO}_2$ entre 1600 et 2000 °C, *Rev. Metall. Paris*, 57 (1960) 149–160.
- [111] D.Y. Povolotskii, V.Y. Mishchenko, G.P. Vyatkin, A.V. Puzyrev, Physico-chemical properties of melts in the system $\text{CaO-Al}_2\text{O}_3\text{-CaF}_2$, *Izv. Vyssh. Uchebn. Zaved., Chern. Metall.*, 13 (1970) 8–12.
- [112] <http://www.sciglass.info/>.

References

- [113] T. Licko, V. Danek, Viscosity and structure of melts in the system CaO-MgO-SiO_2 , *Phys. Chem. Glasses*, 27 (1986) 22–29.
- [114] D.R. Neuville, P. Richet, Viscosity and mixing in molten (Ca, Mg) pyroxenes and garnets, *Geochim. Cosmochim. Acta*, 55 (1991) 1011–1019.
- [115] K. Mizoguchi, M. Yamane, Y. Sugihara, Viscosity measurements of the molten $\text{MeO}(\text{Me}=\text{Ca, Mg, Na})\text{-SiO}_2\text{-Ge}_2\text{O}_3$ silicate system, *J. Japan Inst. Metals*, 50 (1986) 76–82.
- [116] A.S. Panov, I.A. Danyushchenkov, I.S. Kulikov, L.M. Tsylev, Influence of magnesium and barium oxides on the viscosity of silicate melts, *Izv. Akad. Nauk SSSR, Otd. Tekh. Nauk, Metall. Topl.*, 5 (1962) 37–42.
- [117] M. Yamane, N. Takiuchi, Y. Tasaki, K. Mizoguchi, Viscosity of the molten $\text{MeO}(\text{Me}=\text{Li}_2\text{O, Na}_2\text{O, CaO, SrO})\text{-SiO}_2\text{-Y}_2\text{O}_3$ systems, *J. Japan Inst. Metals*, 53 (1989) 1047–1053.
- [118] R.S. McCaffery, C.H. Lorig, I.N. Goff, J.F. Oesterle, O.O. Fritzsche, *AIIME, Techn. Publ.*, 383 (1931).
- [119] Y. Shiraishi, T. Saito, The viscosities of CaO-SiO_2 -alkaline earth fluoride systems (On the viscosity of molten slags, I), *J. Japan Inst. Metals*, 29 (1965) 614–622.
- [120] D.R. Neuville, P. Richet, Viscosity and entropy of liquid mixtures in the $\text{SiO}_2\text{-Al}_2\text{O}_3\text{-CaO-MgO}$ system, *Riv. Staz. Sper. Vetro*, 20 (1990) 213–220.
- [121] I.I. Gulyai, The influence of silica on viscosity of slags of the system calcium oxide-magnesium oxide-silica, *Izv. Akad. Nauk SSSR, Otd. Tekh. Nauk, Metall. Topl.*, 5 (1962) 52–65.
- [122] J.S. Machin, T.B. Yee, D.L. Hanna, Viscosity studies of system $\text{CaO-MgO-Al}_2\text{O}_3\text{-SiO}_2$: III, 35, 45, and 50% SiO_2 , *J. Am. Ceram. Soc.*, 35 (1952) 322–325.
- [123] V.G. Voskoboinikov, N.E. Dunaev, A.G. Mikhalevich, T.I. Kukhtin, S.V. Shtengelmeier, *Svoistva Zhidkikh Domennykh Shlakov*, Moskva, 1975, pp. 159–176.
- [124] I.Y. Chernyavskii, Viscosity and structure of composite silicate melts under superheating and during solidification, in: *Proc. XVth Intern. Congr. on Glass*, Leningrad, 1989, pp. 358–361.
- [125] G.-H. Zhang, K.-C. Chou, K. Mills, Modelling Viscosities of $\text{CaO-MgO-Al}_2\text{O}_3\text{-SiO}_2$ Molten Slags, *ISIJ Int.*, 52 (2012) 355–362.
- [126] P.M. Bruisten, H.B.B. Dam, Viscosity measurement of quartz glass, in: *Proc. 1st Intern. Conf. Fundamentals of Glass Manufacturing Process*, Sheffield, 1991, pp. 18–21.
- [127] S.A. Dunn, Viscous behavior of silica with tungsten inclusions, *Am. Ceram. Soc. Bull.*, 47 (1968) 554–559.
- [128] U.C. Paek, C.M. Schroeder, C.R. Kurkjian, Determination of the viscosity of high silica glasses during fibre drawing, *Glass Technol.*, 29 (1988) 263–266.
- [129] K. Shiraki, M. Ohashi, K. Tajima, M. Tateda, K. Tsujikawa, Viscosity of F and GeO_2 codoped silica glass, *Electron. Lett.*, 29 (1993) 1263–1265.

- [130] R. Clasen, W. Hermann, Differences in properties of natural and synthetic silica glass on the basis of impurity levels, in: *Boll. Soc. Espan. Ceram. Vidrio-Proc. XVI Intern. Congr. on Glass*, Madrid, 1992, pp. 233–238.
- [131] M.R. Vukcevic, A new interpretation of the anomalous properties of vitreous silica, *J. Non-Cryst. Solids*, 11 (1972) 25–63.
- [132] B.O. Mysen, P. Richet, Silicate Glasses and Melts, Properties and Structure, in: *Developments in Geochemistry*, Elsevier, 2005, pp. 131–168.
- [133] I. Schweigert, K. Lehtinen, M. Carrier, M. Zachariah, Structure and properties of silica nanoclusters at high temperatures, *Phys. Rev. B*, 65 (2002) 1–9.
- [134] V.P. Elyutin, V.I. Kostikov, B.S. Mitin, Y.A. Nagibin, Measurements of viscosity of aluminium oxide, *Zh. Fiz. Khim.*, 43 (1969) 579–583.
- [135] G. Urbain, Viscosite de l'alumine liquide, *Rev. Int. Hautes Temp. Refract., Fr.*, 19 (1982) 55–57.
- [136] Y.V. Zubarev, V.I. Kostikov, B.S. Mitin, Y.A. Nagibin, V.V. Nishcheta, Some properties of the molten aluminium oxide, *Neorg. Mater.*, 5 (1969) 1563–1565.
- [137] R.B. Lobzhanidze, A.F. Filippov, P.P. Evseev, Physico-chemical properties of slags in the system $\text{CaF}_2\text{--Me}_x\text{O}_y\text{--Cr}_2\text{O}_3$, *Izv. Vyssh. Uchebn. Zaved., Chern. Metall.*, 13 (1970) 57–154.
- [138] A.G. Shalimov, V.G. Kuklev, Viscosity of lime alumina slags, *Izv. Akad. Nauk SSSR, Otd. Tekh. Nauk, Metall. Topl.*, 5 (1962) 43–51.
- [139] G.I. Zhmoidin, I.S. Kulikov, Viscosity of melts of the system calcium oxide-alumina and solubility of sulfur in them, *Izv. Akad. Nauk SSSR, Metall.*, (1965) 42–52.
- [140] J.O.M. Bockris, D.C. Lowe, Viscosity and the structure of molten silicates, *Proc. R. Soc. Lond. A*, 226 (1954) 423–435.
- [141] S.A. Kalyadina, *Issledovanie Vyazkosti i Udelnoi Elektroprovodnosti Fosfatno-Kremnistykh Rasplavov*, Thesis, Leningrad, 1977.
- [142] S.V. Mikhailikov, E.K. Borodulin, S.V. Shtengelmeier, V.V. Tantsyrev, E.A. Popova, Surface properties, adhesion to steel and viscosity of slags in the system CaO--MgO--SiO_2 , *Tr. Inst. Metall., Sverdlovsk*, (1970) 98–103.
- [143] V.V. Vetysheva, B.I. Leonovich, N.K. Nogteva, Viscosity of molybdenum-containing slags, *Zavodskaya Lab.*, 40 (1974) 1244–1245.
- [144] J.S. Machin, T.B. Yee, Viscosity studies of system $\text{CaO--MgO--Al}_2\text{O}_3\text{--SiO}_2$: IV, 60 and 65% SiO_2 , *J. Am. Ceram. Soc.*, 37 (1954) 177–186.
- [145] W. Weiss, A rapid torsion method for measuring the viscosity of silica glasses up to 2200°C, *J. Am. Ceram. Soc.*, 67 (1984) 213–222.
- [146] H.R. Lillie, High-temperature viscosities of soda-silica glasses, *J. Am. Ceram. Soc.*, 22 (1939) 367–374.

- [147] E. Preston, The Viscosity of the Soda-Silica Glasses at High Temperatures and its Bearing on their Constitution, *J. Soc. Glass Technol.*, 22 (1938) 45–81.
- [148] L. Shartsis, S. Spinner, W. Capps, Density, expansivity, and viscosity of molten alkali silicates, *J. Am. Ceram. Soc.*, 35 (1952) 155–160.
- [149] T.P. Shvaiko-Shvaikovskaya, O.V. Mazurin, Z.S. Bashun, The viscosity of glasses in the $\text{Na}_2\text{O}-\text{SiO}_2$ system in a molten state, *Neorg. Mater.*, 7 (1971) 143–147.
- [150] M.M. Skornyakov, A.Y. Kuznetsov, K.S. Evstropiev, Viscosity of the system $\text{Na}_2\text{SiO}_3-\text{SiO}_2$ in molten state, *Zh. Fiz. Khim.*, 15 (1941) 116–124.
- [151] R. Ota, T. Wakasugi, W. Kawamura, B. Tuchiya, J. Fukunaga, Glass formation and crystallization in $\text{Li}_2\text{O}-\text{Na}_2\text{O}-\text{K}_2\text{O}-\text{SiO}_2$, *J. Non-Cryst. Solids*, 188 (1995) 136–146.
- [152] J. Boow, W.E.S. Turner, The Viscosity and Working Characteristics of Glasses Part I: The Viscosity of Some Commercial Glasses at Temperatures Between Approximately 500° and 1400°, *J. Soc. Glass Technol.*, 26 (1942) 215–240.
- [153] J.-J. Cheng, M.-X. Fan, The effect of fluorine ions and hydroxyl groups on some properties of silicate glasses, in: *Collect. Pap. XIVth Intern. Congr. on Glass*, 1986, pp. 225–232.
- [154] K.D. Kim, Viscosity in mixed-alkali aluminosilicate glass melts, in: *Proc. XVIIth Intern. Congr. on Glass*, Beijing, 1995, pp. 747–752.
- [155] G. Urbain, Viscosité de Liquides Silice-Alumine-Oxydes Na et K. Mesures et Estimations, *Rev. Int. Hautes Temp. Refract., Fr.*, 22 (1985) 39–45.
- [156] A. Winter-Klein, Structure and physical properties of glass, in: *Stekloobraznoe Sostoyanie*, Moskva-Leningrad, 1965, pp. 45–54.
- [157] O. Asayama, H. Takebe, K. Morinaga, Critical cooling rates for the formation of glass for silicate melts, *ISIJ Int.*, 33 (1993) 233–238.
- [158] H.J. Pohlmann, Viskositätsuntersuchungen an Gläsern im kieselsäurereichen Teil des Systems $\text{K}_2\text{O}-\text{PbO}-\text{SiO}_2$, *Glastech. Ber.*, 49 (1976) 177–182.
- [159] R.S. Saringulyan, K.A. Kostanyan, On temperature dependence of electrical conductivity of glasses in a broad temperature range, *Armianskii Khim. Zh.*, 23 (1970) 928–936.
- [160] A.I. Vasiljev, A.A. Lisenenkov, G.A. Rashin, Investigation of the manifestation of mixed-alkali effect on electro-migrational and viscous properties of melts, *Tezisy IV Simp. po Elektricheskim Svoistvam i Stroeniyu Stekla*, Erevan, (1977) 32–34.
- [161] K. Mizoguchi, K. Okamoto, Y. Sugihara, Oxygen coordination of Al^{3+} ion in several silicate melts studied by viscosity measurements, *J. Japan Inst. Metals*, 46 (1982) 1055–1060.
- [162] C.M. Scarfe, D.J. Cronin, J.T. Wenzel, D.A. Kauffman, Viscosity-temperature relationships at 1 atm in the system diopside-anorthite, *Am. Mineral.*, 68 (1983) 1083–1088.
- [163] D. Sykes, J.E. Dickinson, R.W. Luth, C.M. Scarfe, Viscosity-temperature relationships at 1 atm in the system nepheline-diopside, *Geochim. Cosmochim. Acta*, 57 (1993) 1291–1295.

- [164] H. Taniguchi, Universal viscosity-equation for silicate melts over wide temperature and pressure ranges, *J. Volcan. Geotherm. Res.*, 66 (1995) 1–8.
- [165] T.P. Shvaiko-Shvaikovskaya, N.K. Gusakova, O.V. Mazurin, The viscosity of glasses in the Na_2O – CaO – SiO_2 system within a wide temperature range, *Neorg. Mater.*, 7 (1971) 713.
- [166] E.W. Washburn, G.R. Shelton, E.E. Libman, The viscosities and surface tensions of the soda-lime-silica glasses at high temperatures, *Univ. Ill. Bull.*, 21 (1924) 33–48.
- [167] L.N. Sheludyakov, *Sostav, Struktura i Vyazkost Gomogennykh Silikatnykh i Alyumosilikatnykh Rasplavov*, Alma-Ata, (1980) 97.
- [168] L. Sasek, Effect of SO_3 on viscosity, surface tension and adhesion angle of sodium-calcium glass melt, *Silikaty*, 7 (1963) 270–283.
- [169] R.S. Saringyulyan, K.A. Kostanyan, Viscosity and electrical conductivity of glasses in a broad temperature range, *Vyazkost i Elektroprovodnost Stekol v Shirokom Intervale Temperatur*. Deposited in VINITI, Moscow, 902–69 Dep. (1969).
- [170] M. Kawahara, K. Morinaga, T. Yanagase, Measurement of the viscosity and the infrared spectrum of the Na_2O – SiO_2 – MgO ternary system, *J. Japan Inst. Metals*, 41 (1977) 1047–1052.
- [171] J.D. Mackenzie, The discrete ion theory and viscous flow in liquid silicates, *Trans. Faraday Soc.*, 53 (1957) 1488–1493.
- [172] B.M. Fromberg, Z.N. Tsyplenkova, B.V. Rabinovich, Composition dependence of viscosity of electric-bulb glass, in: *Soveshchanie po Vyazkosti Zhidkosti i Kolloidnykh Rastvorov*, Moskva, 1941, pp. 341–351.
- [173] J.S. Machin, T.B. Yee, Viscosity studies of system CaO – MgO – Al_2O_3 – SiO_2 : II, CaO – Al_2O_3 – SiO_2 , *J. Am. Ceram. Soc.*, 31 (1948) 200–204.
- [174] J.R. Rait, R. Hay, Viscosity determinations of slag systems, *J. Royal Techn. Coll., Glasgow*, 4 (1938) 252–275.
- [175] M.J. Toplis, D.B. Dingwell, Shear viscosities of CaO – Al_2O_3 – SiO_2 and MgO – Al_2O_3 – SiO_2 liquids: Implications for the structural role of aluminium and the degree of polymerisation of synthetic and natural aluminosilicate melts, *Geochim. Cosmochim. Acta*, 68 (2004) 5169–5188.
- [176] T. Saito, Y. Kawai, On the viscosities of molten slags. I Viscosities of CaO – SiO_2 – Al_2O_3 slags, *Sci. Rep. Res. Inst. Tohoku Univ., Ser. A*, 3 (1951) 491–501.
- [177] N.L. Zhilo, O.B. Dosov, R.F. Pershina, *Rasplavy*, 1 (1987) 86–91.
- [178] R. Benesch, J. Janowski, J. Delekta, Ustalenie optymalnych warunkow pomiaru lepkości zuzli metalurgicznych, *Archiwum Hutnictwo*, 9 (1964) 103–121.
- [179] M. Ostroukhov, Viscosity of primary blast-furnace slags of the Magnitogorsk plant, *Stahl*, 10–11 (1939) 11–17.
- [180] D. Cranmer, D.R. Uhlmann, Viscosities in the system albite-anorthite, *J. Geophys. Res.*, 86 (1981) 7951–7956.

- [181] M. Cukierman, D.R. Uhlmann, Viscosity of liquid anorthite, *J. Geophys. Res.*, 78 (1973) 4920–4923.
- [182] R.A. Lyutikov, L.M. Tsylev, Viscosity and electrical conductivity of melts of the magnesio-alumino system, *Izv. Akad. Nauk SSSR, Otd. Tekh. Nauk, Metall. Gorn. Delo*, 1 (1963) 41–52.
- [183] N.L. Zhilo, Study of viscosity of synthetic and natural slags of silico-chromium manufacture, *Izv. Akad. Nauk SSSR, Otd. Tekh. Nauk, Metall. Topl.*, 3 (1961) 17–24.
- [184] O.S. Bobkova, Viscosity of slags in the system $\text{MgO-SiO}_2\text{-Al}_2\text{O}_3$, in: *Fiziko-Khimicheskie Osnovy Proizvodstva Stali*, Moskva, 1957, pp. 488–496.
- [185] E.F. Riebling, Structure of magnesium aluminosilicate liquids at 1700°C, *Canad. J. Chem.*, 42 (1964) 2811–2821.
- [186] G.I. Lyudogovskii, M.V. Ibragimova, Viscosity of electric-furnace slags of ferrochromium and silicochromium melts, *Vestn. Akad. Nauk Kaz. SSR*, 12 (1958) 43–54.
- [187] E.F. Riebling, Structure of sodium aluminosilicate melts containing at least 50 mole % SiO_2 at 1500°C, *J. Chem. Phys.*, 44 (1966) 2857–2865.
- [188] M.J. Toplis, D.B. Dingwell, K.-U. Hess, T. Lenci, Viscosity, fragility, and configurational entropy of melts along the join $\text{SiO}_2\text{-NaAlSiO}_4$, *Am. Mineral.*, 82 (1997) 979–990.
- [189] C.M. Scarfe, D.J. Cronin, Viscosity-temperature relationships of melts at 1 atm in the system diopside-albite, *Am. Mineral.*, 71 (1986) 767–771.
- [190] M.J. Toplis, D.B. Dingwell, The variable influence of P_2O_5 on the viscosity of melts of differing alkali/aluminium ratio: Implications for the structural role of phosphorus in silicate melts, *Geochim. Cosmochim. Acta*, 60 (1996) 4107–4121.
- [191] M.J. Toplis, D.B. Dingwell, The structural role of aluminum in highly polymerized silicate melts: new insights from shear viscosity measurements, in: *Proc. XVIIIth Intern. Congr. on Glass CD-ROM*, San Francisco, 1998, pp. D5.86–86.
- [192] M.J. Toplis, D.B. Dingwell, T. Lenci, Peraluminous viscosity maxima in $\text{Na}_2\text{O-Al}_2\text{O}_3\text{-SiO}_2$ liquids: The role of triclusters in tectosilicate melts, *Geochim. Cosmochim. Acta*, 61 (1997) 2605–2612.
- [193] D.J. Stein, F.J. Spera, Experimental rheometry of melts and supercooled liquids in the system $\text{NaAlSiO}_4\text{-SiO}_2$: implications for structure and dynamics, *Am. Mineral.*, 78 (1993) 710–723.
- [194] S. Sakka, K. Kamiya, N. Kato, Viscosities of mixed alkali aluminosilicate glasses of the system $\text{Li}_2\text{O-Na}_2\text{O-Al}_2\text{O}_3\text{-SiO}_2$, *Res. Rep. Fac. Eng., Mie Univ.*, 6 (1981) 81–92.
- [195] K. Kani, Viscosity phenomena of the system $\text{KAlSi}_3\text{O}_8\text{-NaAlSi}_3\text{O}_8$ and of perthite at high temperatures, *Proc. Imper. Acad. Tokyo*, 11 (1935) 334–336.
- [196] H. Taniguchi, T. Murase, Some physical properties and melt structures in the system diopside-anorthite, *J. Volcan. Geotherm. Res.*, 34 (1987) 51–64.

- [197] J.S. Machin, D.L. Hanna, Viscosity studies of system $\text{CaO-MgO-Al}_2\text{O}_3\text{-SiO}_2$: I, 40% SiO_2 , J. Am. Ceram. Soc., 28 (1945) 310–316.
- [198] I.I. Gulyai, Viscosity of slags in the system calcium oxide-magnesium oxide-silica with 5% of alumina, Izv. Akad. Nauk SSSR, Otd. Tekh. Nauk, Metall. Topl., 5 (1960) 219–220.
- [199] E.E. Hofmann, Viskositätsverhalten von synthetischen Schlacken in Abhängigkeit von der Zusammensetzung und der Temperatur, Stahl Eisen, 79 (1959) 846–854.
- [200] A.M. Muratov, I.S. Kulikov, Viscosity of melts of the system $\text{SiO}_2\text{-Al}_2\text{O}_3\text{-CaO-MgO-CaS}$, Izv. Akad. Nauk SSSR, Metall., 4 (1965) 57–62.
- [201] M.P. Volarovich, Investigation of viscosity and plasticity of molten slags and rocks, Zh. Fiz. Khim., 4 (1933) 807–814.
- [202] M.P. Volarovich, Investigation of viscosity of melted rocks, Dokl. Akad. Nauk SSSR, 1 (1934) 561–563.
- [203] I.P. Semik, On the viscosity of blast-furnace slags, in: Soveshchanie po Vyazkosti Zhidkosti i Kolloidnykh Rastvorov, Moskva, 1941, pp. 257–269.
- [204] N.M. Pavlushkin, P.D. Sarkisov, B.M. Gurevich, Viscosity and activation energy of viscous flow of glasses in the system $\text{CaO-Al}_2\text{O}_3\text{-SiO}_2\text{-Na}_2\text{O}$, Shlakositaly, Moskva, (1970) 84–92.
- [205] G.-H. Zhang, K.-C. Chou, Influence of $\text{Al}_2\text{O}_3/\text{SiO}_2$ Ratio on Viscosities of $\text{CaO-Al}_2\text{O}_3\text{-SiO}_2$ Melt, ISIJ Int., 53 (2013) 177–180.
- [206] D.B. Dingwell, R. Knoche, S.L. Webb, M. Pichavant, The effect of B_2O_3 on the viscosity of haplogranitic liquids, Am. Mineral., 77 (1992) 457–461.
- [207] J.T. Kohli, US Patent No. 6753279 Int.Cl C 03 C 3/085, <http://ep.espacenet.com/>, 2004.
- [208] G.S. Galakhova, A.S. Kutukov, T.I. Povolotskaya, Technological properties of glasses for medicine application, Steklo Keram., 1 (1988) 13–14.
- [209] V.P. Barzakovskii, S.K. Dubrovo, Fiziko-Khimicheskie Svoistva Glazurei Vysokovoltного Farfora, Moskva-Leningrad, (1953) 186.
- [210] B.O. Mysen, P. Richet, Silicate Glasses and Melts, Properties and Structure, in: Developments in Geochemistry, Elsevier, 2005, pp. 231–258.
- [211] S.L. Webb, M. Banaszak, U. Köhler, S. Rausch, G. Raschke, The viscosity of $\text{Na}_2\text{O-CaO-Al}_2\text{O}_3\text{-SiO}_2$ melts Eur. J. Mineral., 19 (2007) 681–692.
- [212] G.-H. Zhang, K.-C. Chou, Measuring and Modeling Viscosity of $\text{CaO-Al}_2\text{O}_3\text{-SiO}_2\text{-(K}_2\text{O)}$ Melt, Metall. Mater. Trans. B, 43 (2012) 841–848.
- [213] J.W. Giffen, D.A. Duke, W.H. Dumbaugh, J.E. Flannery, J.F. MacDowell, J.E. Megles, US Patent No.3673049 Int.Cl B 32 b 7/02, 17/06, <http://ep.espacenet.com/>, 1972.
- [214] M. Chen, S. Raghunath, B. Zhao, Viscosity of $\text{SiO}_2\text{-"FeO"-Al}_2\text{O}_3$ System in Equilibrium with Metallic Fe, Metall. Mater. Trans. B, 44 (2013) 820–827.

- [215] M. Chen, S. Raghunath, B. Zhao, Viscosity Measurements of SiO_2 –“FeO”–MgO System in Equilibrium with Metallic Fe, *Metall. Mater. Trans. B*, 45 (2014) 58–65.
- [216] A.C. Ducret, W.J. Rankin, Liquidus temperatures and viscosities of FeO – Fe_2O_3 – SiO_2 – CaO – MgO slags at compositions relevant to nickel matte smelting, *Scand. J. Metall.*, 31 (2002) 59–67.
- [217] F.-Z. Ji, D. Sichen, S. Seetharaman, Experimental Studies of the Viscosities in the CaO – FeO – SiO_2 Slags, *Metall. Mater. Trans. B*, 28 (1997) 827–834.
- [218] S. Gerlach, O. Claussen, C. Russel, Self-diffusion of iron in alkali–magnesia–silica glass melts, *J. Non-Cryst. Solids*, 226 (1998) 11–18.
- [219] G. Urbain, C.R. Hebd, *Seances Acad. Sci. II*, 232 (1951) 330.
- [220] P. Roentgen, H. Winterhager, L. Kammel, *Erzmetall*, 9 (1956) 207–214.
- [221] Y. Shiraishi, K. Ikeda, A. Tamura, T. Saito, On the Viscosity and Density of the Molten FeO – SiO_2 System, *Trans. JIM*, 19 (1978) 264–274.
- [222] S. Sumita, K. Morinaga, T. Yanagase, Physical Properties and Structure of Binary Ferrite Melts, *Trans. Japan Inst. Metals*, 24 (1983) 35–41.
- [223] M. Kucharski, N.M. Stubina, J.M. Toguri, Viscosity Measurements of Molten Fe – O – SiO_2 , Fe – O – CaO – SiO_2 , and Fe – O – MgO – SiO_2 Slags, *Can. Metall. Q.*, 28 (1989) 7–11.
- [224] M. Chen, S. Raghunath, B. Zhao, Viscosity Measurements of “FeO”– SiO_2 Slag in Equilibrium with Metallic Fe, *Metall. Mater. Trans. B*, 44 (2013) 506–515.
- [225] Y. Waseda, Y. Shiraishi, J.M. Toguri, The structure of the molten FeO – Fe_2O_3 – SiO_2 system by X-ray diffraction, *Trans. JIM*, 21 (1980) 51–62.

Appendix

Currently optimized model parameters as well as predicted theoretical viscosity and activation energy of viscous flow for the FeO/Fe₂O₃-containing systems

Structural unit i	Model parameters		Predicted theoretical viscosity and activation energy of viscous flow	
	A _i	B _i	$\eta_{T \rightarrow \infty}$, Pa·s	E _{η} , kJ/mol
FeO	-8.998	10.273	1.24×10^{-04}	85.42
Fe ₂ O ₃	-11.241	11.135	1.31×10^{-05}	92.58
FeNa ₂ O ₂	-8.313	20.869	2.45×10^{-04}	173.52
FeSiO ₃	-2.781	94.710	6.20×10^{-02}	787.46
Fe ₂ SiO ₄	-25.356	23.339	9.72×10^{-12}	194.05
FeSi ₂ CaO ₆	-17.375	18.347	2.85×10^{-08}	152.54
FeSi ₂ MgO ₆	-41.444	39.274	1.00×10^{-18}	326.54
FeSiNa ₂ O ₄	-2.971	10.773	5.13×10^{-02}	89.57
FeAl ₂ O ₄	-18.848	26.008	6.53×10^{-09}	216.24
Fe ₂ Si ₅ Al ₄ O ₁₈	-2.147	17.248	1.17×10^{-01}	143.41
CaFe ₂ O ₄	-11.017	12.594	1.64×10^{-05}	104.71
MgFe ₂ O ₄	-16.427	10.789	7.35×10^{-08}	89.70
NaFeO ₂	-16.206	21.870	9.15×10^{-08}	181.84
KFeO ₂	-10.310	23.560	3.33×10^{-05}	195.88

It is seen that the values of the model parameters B_i for CaFe₂O₄, MgFe₂O₄, NaFeO₂, and KFeO₂ follow the order: KFeO₂ > NaFeO₂ > CaFe₂O₄ > MgFe₂O₄, which is reasonable from the view of ionization potential. In contrast, the model parameter B_i for the species FeAl₂O₄ is equal to that of the other Al³⁺-induced quasi-tetrahedra, which might be caused by the stronger charge compensation effect induced by Al³⁺. The species Fe₂O₃ has the larger activation energy of viscous flow than the species FeO. According to the degree of polymerization, the activation energy of species FeSiO₃ is greater than that of the species Fe₂SiO₄. However, it is noted that the activation energy

of the species FeSiO_3 seems to be too large (greater than that of the species $(\text{SiO}_2)_6$), which needs to be further optimized. The same holds for the species $\text{FeSi}_2\text{MgO}_6$.

Acknowledgements

I would like to express my sincerest thanks to Prof. Lorenz Singheiser and Dr. Michael Müller for offering this opportunity to perform an interesting doctoral study in the institute of energy and climate research (IEK-2), Forschungszentrum Jülich.

I wish to present my deepest gratitude to my supervisor, Dr. Michael Müller, who has supported me throughout my thesis with his excellent guidance, encouragement, and patience whilst allowing me the room to work in my own way. My grateful thanks are extended to Prof. Erwin Wosch and Prof. Klaus Hack for their in-depth discussions and valuable suggestions.

I wish to record my grateful thanks to Dr. Elena Yazhenskikh for her valuable explanation about the thermodynamic modified associate species model and giving me lots of supports in the field of thermodynamic. My special thanks are given to Mr. Sören Seebold for his excellent experimental ideas and valuable discussions. I am also very appreciative of assistance from Dr. Marc Bläsing, Dr. Dietmar Kobertz, Dr. Tatjana Jantzen, Dr. Stephan Petersen, Mr. Heinrich Esser, Mr. Paul Joecken, Mr. Wolfgang Dank, Mrs. Marita Offermann, and Mrs. Inge Dreger.

I would like to take this opportunity of thanking Dr. Emanuel Forster, Dr. Sarah Schaafhausen, Dr. Maria Benito Abascal, Mr. Andre Horstenkamp, Dr. Mingshui Ma, Dr. Dmitry Sergeev, Dr. Kamila Armatys, and Miss. Kerstin Dönecke for the excellent and pleasant atmosphere they created. I would also like to thank all the scientific and nonscientific staff of IEK-2 for their help during my work period. I am very grateful to my parents and my wife for their unceasing encouragement, support, and attention.

The work has been performed in the framework of the HotVeGas Project supported by Bundesministerium für Wirtschaft und Technologie (FKZ 0327773) and the HViGasTech Project supported by the Helmholtz Association of German Research Centers (VH-VI-429).

Band / Volume 268

Chemische, verfahrenstechnische und ökonomische Bewertung von Kohlendioxid als Rohstoff in der chemischen Industrie

A. Otto (2015), viii, 272 pp

ISBN: 978-3-95806-064-7

Band / Volume 269

Energetische und wirtschaftliche Optimierung eines membranbasierten Oxyfuel-Dampfkraftwerkes

Y. Nazarko (2015), IV, 337 pp

ISBN: 978-3-95806-065-4

Band / Volume 270

Investigation of light propagation in thin-film silicon solar cells by dual-probe scanning near-field optical microscopy

S. Lehnen (2015), 120 pp

ISBN: 978-3-95806-066-1

Band / Volume 271

Characterization of soil water content variability at the catchment scale using sensor network and stochastic modelling

W. Qu (2015), XVI, 123 pp

ISBN: 978-3-95806-067-8

Band / Volume 272

Light Absorption and Radiative Recombination in Thin-Film Solar Cells

T. C. M. Müller (2015), ii, 146 pp

ISBN: 978-3-95806-068-5

Band / Volume 273

Innenbeschichtung poröser Körper mittels Atomlagenabscheidung zur Redoxstabilisierung anodengestützter Festoxidbrennstoffzellen

T. Keuter (2015), XII, 133 pp

ISBN: 978-3-95806-069-2

Band / Volume 274

Thermochemical Modeling of Laves Phase Containing Ferritic Steels

A. Jacob (2015), 200 pp

ISBN: 978-3-95806-070-8

Band / Volume 275

Lithiumbatterien für stationäre und mobile Anwendungen: Benchmarking und experimentelle Umsetzung

T. Bergholz (2015), vi, 387 pp

ISBN: 978-3-95806-071-5

Band / Volume 276

Pyrochlore as nuclear waste form: actinide uptake and chemical stability

S. C. Finkeldei (2015), IX, 155 pp

ISBN: 978-3-95806-072-2

Band / Volume 277

Herstellung von Elektrodenstrukturen für Lithium-Ionen-Dünnschichtbatterien

A. Bünting (2015), v, 151 pp

ISBN: 978-3-95806-073-9

Band / Volume 278

Keramiken des Monazit-Typs zur Immobilisierung von minoren Actinoiden und Plutonium

J. M. Heuser (2015), viii, 212 pp

ISBN: 978-3-95806-076-0

Band / Volume 279

IEK-3 Report 2015

Systems Research and Engineering for a Sustainable Energy Supply
(2015)

ISBN: 978-3-95806-077-7

Band / Volume 280

IEK-3 Report 2015

Systemforschung und –technik für eine nachhaltige Energieversorgung
(2015)

ISBN: 978-3-95806-078-4

Band / Volume 281

Integration of the German energy transition in the EU-context

A. Ernst (2015), 76 pp

ISBN: 978-3-95806-079-1

Band / Volume 282

Modelling and Experimental Validation of the Viscosity of Liquid Phases in Oxide Systems Relevant to Fuel Slags

G. Wu (2015), XVI, 170 pp

ISBN: 978-3-95806-081-4

Weitere *Schriften des Verlags im Forschungszentrum Jülich* unter
<http://www.zbw1.fz-juelich.de/verlagextern1/index.asp>

Energie & Umwelt /
Energy & Environment
Band / Volume 282
ISBN 978-3-95806-081-4

